THEORETICAL AND EXPERIMENTAL STUDIES OF MULTISTEP ELECTROCHEMICAL BIOSENSORS

By

Neda Rafat

A DISSERTATION

Submitted to
Michigan State University
in partial fulfillment of the requirements
for the degree of

Chemical Engineering—Doctor of Philosophy

2020

ABSTRACT

THEORETICAL AND EXPERIMENTAL STUDIES OF MULTISTEP ELECTROCHEMICAL BIOSENSORS

By

Neda Rafat

Electrochemical biosensors are analytical devices that detect analytes by transforming a biochemical reaction into a quantitative, electrical signal. This class of biosensors has proven valuable in research, quality control, food safety, medical diagnosis, and monitoring of therapeutic efficacy. Electrochemical biosensors integrate specificity of biological recognition molecules (e.g., antibodies) with the advantages of electrochemical detection techniques (reproducible, quantitative electrical output) to provide sensitive and specific analytical devices. Miniaturized amperometric biosensors that use redox enzymes to generate an electric current in response to the voltage applied at a working electrode have been successfully commercialized.

Mechanistic mathematical models that describe the multiple mass-transfer and chemical-reaction steps that give rise to the electrical output are needed to help design, optimize, and validate electrochemical biosensors for medical and environmental applications.

In this work, experimental and theoretical studies of two types of multistep electrochemical biosensors were performed. An electrochemical immunosensor (EI) was fabricated on screen-printed electrodes (SPEs) for detection of a model protein (mouse IgG) by integrating principles of an enzyme-labled immunosorbent assay (ELISA) using horseradish peroxidase (HRP) as the labeling enzyme and an electrochemical transducer. Experimental conditions such as substrates concentration, pH, and applied voltage were optimized using a fractional factorial design. A mathematical model was developed to simulate the EI's steady-state signal by solving the non-linear ordinary differential equations including enzyme kinetics and diffusion-based mass transfer

rates for all the reactants. A new concept, current-control coefficient, was introduced to measure the extend to each reaction step limited the current density. The model allows the rate limiting step to be indentified and experimental conditions that optimize detetction sensitivity to be determined.

In addition, experimental and theoretical studies of an inhibition-based bi-enzyme electrochemical biosensor (IBE) for a model inhibitor of acetylcholinesterase (AChE), phenylmethyl sulfonyl fluoride (PMSF), were conducted. The IBE was fabricated by co-immobilization of AChE and tyrosinase (Tyr) on the gold working electrode of a SPE. Inclusion of a hydrolase enzyme (AChE) and an oxidase enzyme (Tyr) provided an amplification system which improved the biosensor's sensitivity significantly. A comprehensive mathematical model was developed to simulate time-dependent electrochemical signal in the IBE. The unsteady-state model was developed by solving a system of non-linear partial differential equations including enzymatic reactions, inhibition kinetics of AChE by an inhibitor (PMSF), and diffusion-based mass transfer steps. The model successfully simulated the IBE's response to the substrate (phenyl acetate) and the inhibitor. Using the model along with the current-control coefficient and sensitivity parameters, effect of the governing factors on the IBE's performance were studied. The model allowed to optimize the governing factors to achieve optimum sensitivity for detection of the inhibitor and design the biosensor to achieve specific performance criteria.

Dedicated to my family

ACKNOWLEDGMENTS

I would like to express my sincere gratitude to my supervisor, Prof. Robert Mark Worden for his continuous support, encouragement, and guidance during my P.h.D research. Dr. Worden provided a positive and respectful work environment which helped me to grow my professional skills with his insight, patience, valuable knowledge, and positive attitude. Throughout my Ph.D. study, Dr. Worden always put his effort and time to teach me his great knowledge clearly and simply. I truly feel honored for having the opportunity to be in Dr. Worden's research group.

I would like to thank Dr. Paul Satoh for his support and valuable ideas during my Ph.D work. It was an honor to know him and learn a lot from his valuable experiences and knowledge in the field of biosensors and biochemistry.

I would like to thank my committee members, Dr. Scott Calabrese Barton, Dr. Dana Spence, and Dr. David Hickey for their helpful ideas, support, and contributions to this work.

I would like to thank our collaborators, Dr. Mohsen Zayernouri for his valuable insight and help on developing mathematical models of our biosensors, Dr. Jonathan Hardy for generously sharing his great knowledge and laboratory space with us to conduct research on *Listeria monocytogenes*, and Dr. Masamitsu Kanada for kindly tutoring me on extraction of extracellular vesicles from breast cancer-cells.

Finally, I would like to thank my husband, Iman, for all his dedication and support, and my wonderful parents for being my inspiration and motivation to always seek higher goals.

TABLE OF CONTENTS

LIST OF TABLES

LIST OF FIGURES

KEY TO SYMBOLS AND ABBREVIATIONS

ELISA	Enzyme linked immunosorbent assay
PMSF	Phenylmethylsulfonylfluoride
NTE	Neuropathy target esterase
OP	Organophosphorus compound
EI	Electrochemical immunosensor
IBE	Inhibition-based bi-enzyme electrochemical biosensor
LM	*Listeria monocytogenes*
EV	Extracellular vesicle
POC	Point-of-care
HRP	Horseradish peroxidase
AChE	Acetylcholinesterase
Tyr	Tyrosinase
EDC	1-Ethyl-3-(3-dimethylaminopropyl) carbodiimide
NHS	N-Hydroxy succinimide
BSA	Bovine serum albumin
SPE	Screen-printed electrode
RSM	Response surface methodology
PCR	Polymerase chain reaction
EET	External electron transfer
CAGR	Compound annual growth rate
TMB	3,3',5,5'-Tetramethylbenzidine
H_2O_2	Hydrogen peroxide
MBTH	3-Methyl-2-benzothiazolinone hydrazone hydrochloride hydrate
PBS	Phosphate buffered saline
NTA	Nanoparticle tracking analysis

WT	Wild type
BHI	Brain heart infusion
E	Applied electrochemical potential on the working electrode
C	Catechol
Q	O-quinone
E_h	Standard electrochemical potential
D	Diffusion coefficient
D_δ	Diffusion coefficient in the diffusion layer
D_L	Diffusion coefficient in the immunosensing/enzyme-containing layer
V_{max}	Maximum enzymatic reaction rate
k^{cat}	Catalytic rate constant in Michaelis-Menten kinetics
K_m^C	Michaelis-Menten constant of HRP for catechol
$K_m^{H_2O_2}$	Michaelis-Menten constant of HRP for hydrogen-peroxide
J	Current density
n	Number of transferred electrons in a redox reaction
m	Number of transferred protons in a redox reaction
F	Faraday constant
R	Universal gas constant
T	Temperature
E_{mid}	Midpoint potential of a voltammogram
L	Thickness of immunosensing/enzyme-containing layer
δ	Thickness of diffusion layer
k_p	Partition coefficient
C_{Vi}^J	Current-control coefficient
S	Sensitivity
S_1	Phenyl acetate
S_2	Phenol

S_3	Catechol
S_4	O-quinone
E_1	Acetylcholinesterase activity
E_2	Phenolase activity of tyrosinase
E_3	Catecholase activity of tyrosinase
I	Inhibitor of acetylcholinesterase
k'	pseudo-first-order rate constant for the inactivation of AChE with PMSF
k_2	Reaction constant of deactivation of acetylcholinesterase with PMSF
k_I	Dissociation constant of PMSF
k_{+1}	Forward rate constant for binding of the inhibitor to AChE
k_{-1}	Backward rate constant for binding of the inhibitor to AChE
K_0	Heterogeneous electron transfer rate
AF	Amplification factor
σ	Damkohler number

1 Introduction

1.1 Overview

A biosensor is defined as a device that utilizes a biochemical mechanism to transfer concentration or presence of a specific sample component (analyte) to a detectable signal [1-3]. Biosensors have a wide range of applications including environmental monitoring, disease detection, food safety, drug discovery, etc [4]. A biosensor includes two major components: a biological recognition element or a bioreceptor and a transducer [3, 5, 6]. Biological recognition element or bioreceptor specifically targets the analyte by using a biochemical mechanism for recognition. Bioreceptors can be generally divided into five categories: enzyme, antibody/antigen, nucleic acid/DNA, cellular structure/cell, and biomimetics. The enzymes and antibodies are the most commonly used type of bioreceptors in biosensor applications [3, 7, 8]. The main categories of transduces in biosensor applications are electrochemical transducer, optical transducer, piezoelectric transducer, and gravimetric transducer [7, 9]. Electrochemical transducers report the presence or concentration of analyte in the form of an electrical signal. Electrochemical biosensors integrate the sensitivity of electrochemical transducers and their low limit of detection with the high specificity of the bioreceptors. Electrochemical biosensors benefit from several advantages such as low cost, ease of use, portability, and simplicity of construction. These advantages make electrochemical biosensors great options for development of analytical devices in different fields [10, 11]. The electrochemical biosensors can be divided in four major categories based on the electrochemical technique which is used to measure the electrical signal produced by the biochemical mechanism: amperometric biosensors, potentiometric biosensors, conductometric biosensors, and impedimetric biosensors [12]. In amperometric biosensors, electric current flow between two electrodes is measured (usually at a fixed applied electrochemical potential on a working electrode)

when a redox reaction takes place on the working electrode [13]. In potentiometric biosensors, the electrochemical potential difference between a working electrode and a reference electrode is measured. This potential difference is related to the analyte concentration [14]. Conductometric biosensors measure the electrical conductivity in the sample solution, which can be changed by changing the analyte concentration[15]. In impedimetric biosensors, an analyte is detected by measuring the change in the impedance of the system, which is caused by the biochemical reaction between the bioreceptor and the analyte [16]. While each electrochemical transducer has its unique advantages, in this work, we have been focused in amperometric transducers due to their high sensitivity, simplicity of their construction, relative low background signal and wide linear range [17].

This dissertation describes theoretical and experimental studies of two electrochemical biosensors: an electrochemical immunosensor (EI) for a model antigen and an inhibition-based bi-enzyme electrochemical biosensor (IBE) for the detection of a model inhibitor of acetylcholinesterase. The EI was developed by the integration of an amperometric transducer with the principal of the enzyme-labeled immunosorbent assay (ELISA). The IBE was developed by including a hydrolase enzyme (acetylcholinesterase) and an oxidase enzyme (tyrosinase). The inclusion of the two enzymes provides an amplification system that improves the biosensor's sensitivity significantly. While the underlying theme of this study is the development of electrochemical biosensors, each chapter in this thesis addresses a unique architecture or issue.

Chapter 2 of this dissertation discusses the principles of an optical ELISA, and this high throughput assay was used to find and optimize the type of bioreceptors before developing an EI.

In Chapter 3, the theoretical and experimental studies of an EI for a model antigen, mouse IgG, is discussed. This chapter reports a unique and novel mathematical model for the simulation and

optimization of the steady-state EI's signal. A new concept, the current-control coefficient, is introduced to measure the extent that each reaction step is limiting the current density. The model allows to predict the rate limiting step and optimize experimental conditions for improving the sensitivity of detection for the mouse IgG.

Chapter 4 of this dissertation is devoted to the theoretical and experimental studies of an IBE for the detection of organophosphorus compounds. IBE is fabricated by co-immobilization of acetylcholinesterase (AChE) and tyrosinase (Tyr) on the gold working electrode of an SPE. The inclusion of a hydrolase enzyme (AChE) and an oxidase enzyme (tyrosinase) provides an amplification system that significantly improved the biosensor's sensitivity. A comprehensive mathematical model is presented to simulate the time-dependent electrochemical signal in the IBE. The unsteady-state model is developed by solving a system of non-linear partial differential equations, including enzymatic reactions, inhibition kinetics of AChE by an inhibitor (PMSF), and diffusion-based mass transfer steps. The model successfully simulates the IBE's response to the substrate (phenyl acetate) and the inhibitor. Using the model and the current-control coefficient and sensitivity parameters, the effect of the governing factors on the sensitivity are examined. The model provides a platform to optimize the governing factors to achieve optimum sensitivity for detecting the inhibitor.

Finally, in Chapter 5, it will be discussed how the developed EI and previous research in Dr. Worden's research group in the field of chromatids, can be applied for the ongoing research of *Listeria monocytogenes*.

1.2 Enzyme Linked Immunosorbent Assay (ELISA)

The enzyme-linked immunosorbent assay (ELISA) is a commonly used analytical biochemistry assay that is developed based on the strong and specific antibody-antigen interactions [18]. This is a plate-based assay technique which is frequently used for detecting and quantifying peptides, proteins, antibodies, toxins, pathogens, and hormones [18, 19]. ELISAs are typically performed in 96-well polystyrene plates where the analyte is immobilized on the bottom of wells directly or with the aid of an antibody. Then, an enzyme conjugated antibody is used to detect the immobilized analyte. The enzyme reacts with a substrate to produce a measurable optical signal which its intensity is related to the analyte concentration. ELISAs can be divided into three categories based on their binding structure of antibody and antigen: indirect ELISA, competitive ELISA and Sandwich ELISA [20]. In this work, the focus was on integration of electrochemical transducers with sandwich ELISAs. In a sandwich ELISA, a capture antibody against the analyte is coated on the plate to detect the analyte from the sample solution. Then a secondary antibody conjugated to an enzyme is added to detect the antibody-analyte complex. Finally, a substrate is added that can react with the immobilized enzyme to produce an optical signal which its intensity is related to the analyte concentration. This technique benefits from a high specificity as two antibodies are used to specifically detect and bind the analyte [21, 22]. Because conventional ELISAs in a 96-well plate provide a high throughput standard platform to develop an immunoassay against a specific analyte, they were performed in this work prior to the development of the EI for a specific analyte. Developed optical ELISAs are discussed in Chapter 2. An ELISA was performed against a model antigen, mouse IgG, to validate functionality of antibodies and optimizes the governing factors. Once a successful optical ELISA was developed with the proper antibodies, the principal of ELISA was integrated with an amperometric transducer to develop an EI. An optical ELISA was also developed for the detection of extracellular vesicles (EVs) from breast cancer cells. EVs are

membrane-bound vesicles that can be produced by any type of live cells, including breast cancer cells [23]. In this work, we were interested to develop an electrochemical biosensor for the detection of EVs from breast cancer cells as an approach for detection of breast cancer cells, but before that, it was important to find a proper surface biomarker on the EVs to target them. Recent studies have shown that EVs carry surface biomarkers which can be specific to their cell of origin. Some works have shown elevated concentrations of some of the tetraspanin proteins, including CD63 and CD81 on EVs from breast cancer cells [23, 24]. Before developing an EI for EVs from breast cancer cells, it was crucial to find out which surface biomarker is efficient for the detection of the EVs. Chapter 2 discusses the development of the optical ELISAs and how their results guided us for fabrication of EIs.

1.3 Integrated Experimental and Theoretical Studies on an Electrochemical Immunosensor

Continuous monitoring and screening of biological and chemical pathogens, contaminants, and biomarkers play an important role in prevention of disease spread and pathologies, early diagnosis of cancers, and the study of the efficacy of treatments [25]. Electrochemical immunosensors benefits from several advantages, which make them a great option in point of care (POC) and on-site diagnostics. They are developed by integrating immune principles and electrochemical transducers. High sensitivity, ease of use, low cost, portability, and having potential for automation and miniaturization are some of the advantages of electrochemical biosensors [26, 27]. Antibodies are universal biorecognition molecules that recognize their corresponding antigen to form highly specific antigen-antibody complexes. Extreme affinity and selectivity of antigen-antibody interactions provide great sensitivity for electrochemical immunosensors [28, 29]. Sandwich immunoassay has been widely used in electrochemical immunosensors. In this assay, a capture

antibody immobilized on the electrode captures the antigen and form an antibody-antigen complex. Then, a labeled detection antibody is used to detect and quantify antibody-antigen complexes [30]. Horseradish peroxidase (HRP) is the most commonly used enzyme label in sandwich immunoassay. This is mainly because of the high catalytic activity of HRP, its commercial availability, and its capacity for oxidation of a wide range of substrates [31]. Besides, due to its relatively small molecular size and stability to chemical modification, HRP is very suitable for the labeling of immunological reagents [32]. HRP has been used as the labeling enzyme in a wide range of disposable electrochemical immunosensors. While some mathematical models have been developed to study the kinetics of HRP [33-37], there is a lack of a comprehensive mathematical model that can be used to study, optimize, and simulate the HRP induced electrochemical signal under different experimental conditions and predict the rate limiting step. Chapter 3 presents a mechanistic model to simulate the steady-state signal in an electrochemical immunosensor (EI) having HRP as the labeling enzyme. An electrochemical immunosensor was developed for mouse immunoglobulin G (IgG), as a model antigen, using HRP as the labeling enzyme. Immunosensing layer was prepared by using EDC-NHS chemistry since this chemistry is widely used for the preparation of the immunosensing layer in electrochemical immunosensors. [38-40]. EDC (1-Ethyl-3-(3-dimethylaminopropyl)carbodiimide) is a zero-length cross-linker, which causes the coupling of primary amines to carboxylate groups. The addition of NHS (N-Hydroxysuccinimide) to EDC reactions increases the efficiency of the coupling reaction [41]. Experimental variables such as substrates concentration, electrochemical potential, and pH affect a biosensor sensitivity [42]. Therefore, a statistical model was developed using response surface methodology (RSM) to optimize multiple experimental variables influencing our biosensor signal. RSM is an efficient statistical method for screening and optimizing multiple variables influencing a response [43]. The

mechanistic model was developed by solving a set of non-linear differential equations, including diffusion equations coupled with non-linear enzymatic reactions. A bi-substrate ping-pong mechanism was assumed for the enzymatic reaction catalyzed by HRP [44-46]. Our mechanistic model provided a platform to study the effect of applied electrochemical potential, hydrogen peroxide concentration, catechol concentration, and pH on steady-state signal and it allowed simulating the signal under different experimental conditions. Besides, it helped to understand and study the mass transfer steps and reactions happening on the biosensor interface. Concepts such as current-control coefficient, sensitivity, and Damkohler number were introduced in this chapter using the mechanistic model to predict the rate limiting step and study the effect of the governing factors on sensitivity. Knowing such information would help to optimize governing factors for improving the EI's performance.

1.4 Theoretical and Experimental Studies of an Inhibition-based Bi-enzyme Electrochemical Biosensor (IBE) for Detection of Organophosphorus Compounds

Organophosphorus compounds (OPs) are the main group of insecticides (malathion, parathion, diazinon, fenthion, dichlorvos, chlorpyrifos, and others) and nerve gases (soman, sarin, tabun, and VX)[47]. OPs are synthetic chemicals first synthesized in early 1800 [48]. OPs have been commercially developed as pesticides for over five decades, and they still are used as pesticides and insecticides [49]. OPs eradicate pests by deactivating an important enzyme in the body called acetylcholinesterase (AChE). AChE is a vital enzyme responsible for controlling nerve signals in the body[50, 51]. The widespread use of OPs cause their accumulation in soil and aquatic organisms and poses a serious risk to non-target species, including humans and animals [26]. Extensive use of OPs in modern agriculture pesticides and their high toxicity requires development of analytical devices that can effectively monitor environmental samples and food samples [52].

The current gold standard technique for the detection of OPs is based on the principles of chromatography[53, 54]. Although these techniques provide accurate results for detection of OPs, they are expensive, time-consuming, require special trained technicians, and cannot be used for on-site applications [55].

In contrast, electrochemical biosensors offer several advantages such as high sensitivity, fast response, the potential for being miniaturized and portable, and being cost effective. These advantages make electrochemical biosensors great options for the development of portable analytical devices for OPs detections [56]. In general, electrochemical biosensors for detection of OPs are developed based on three main principles: inhibition of acetylcholinesterase (AChE) or butyrylcholinesterase with OPs, inhibition of enzymes phosphatase with OPs, and direct electrochemical detection of OPs [56]. In this work, we have been interested in the development of an inhibition-based bi-enzyme electrochemical biosensor (IBE) for the detection of OPs using AChE. OPs can covalently bind to the active site of AChE to inhibit it. The amount of inhibition in AChE activity is related to the OPs concentration. The inhibition of AChE with OPs is the principle of the detection method in inhibition-base electrochemical biosensors [57-60]. Acetylcholine and acetylthiocholine are two commonly used substrates in AChE electrochemical biosensors. AChE hydrolyses acetylcholine to produce choline which can be detected by use a second enzyme, choline oxidase [59]. In the case of acetylthiocholine, product of the hydrolase reaction catalyzed by AChE is thiocholine which can be oxidized to produce an electric signal which is related to AChE activity. In this work, we were interested in combining AChE with an oxidase enzyme, tyrosinase (Tyr), to develop an IBE with an amplification system for the detection of OPs. This biosensor is a modified version of a novel electrochemical biosensor that was previously developed in Dr. Worden's group to measure the activity of a hydrolase enzyme,

neuropathy target esterase [61]. Chapter 4 discusses theoretical and experimental studies of the developed IBE for the detection of a model inhibitor. It would be discussed how the inclusion of AChE and Tyr created an amplification system which improve the sensitivity of detection for a model inhibitor, phenyl methyl sulfonyl fluoride (PMSF). Besides, a comprehensive mathematical model is presented for simulation of the unsteady-state electric signal in the presented biosensor. The mathematical model provides a platform to estimate the rate limiting step in the biosensor and optimize the experimental condition in a way that maximum sensitivity is obtained.

1.5 Use of Electrochemical Detection Techniques for *Listeria Monocytogenes* Ongoing Research

Chapter 5 of this dissertation discusses briefly how the previously developed techniques in Dr. Worden's group in the field of chemotaxis and electrochemical biosensors can be applied to the *Listeria monocytogens* (*LM*) ongoing research. This work was performed with close collaboration with Dr. Jonathan Hardy (MSU Microbiology and Molecular Genetics Dept). *LM* is a gram-positive facultative intracellular pathogen, which can invade and multiply within mammalian cells [62]. Listeriosis, a serious infection caused by *LM* with a global mortality rate of 24 %, is most likely to infect high-risk population groups, including pregnant women, their fetuses, adults over 65 years old, and immunocompromised people [63]. According to the Centers for Disease Control and Prevention (CDC), 1600 people are diagnosed with listeriosis within the United States annually, 260 of which lead to death. *LM* can grow and survive under a wide range of environmental conditions, including high salt concentrations, anaerobic environments, refrigeration temperatures, and acidic conditions. Besides, *LM* can produce biofilms on food production equipment plants that allow their organism to survive for more than ten years. All these features favor *LM* as a foodborne pathogen and make it ubiquitous in the environment [63, 64]. To

avoid health risks associated with *LM*, it is important to be able to detect this pathogen in different environments and food samples and as well as to learn more about its survival mechanism in adverse growth conditions such as anaerobic conditions [65]. Some of the common detection methods of *LM* are culturing, biosensors, enzyme linked immunosorbent assay (ELISA), and polymerase chain reaction-based method (PCR). Among these methods, biosensors are the latest techniques which provide a low detection limit [65]. Recently, it was discovered that *LM* can secrete biologically active extracellular vesicles (EVs) despite having a thick cell wall and lack of outer membrane [66-68]. These EVs, with a diameter ranging from 20 to 200 nm, can be used as toxin cargo to transport concentrated virulence factors to host cells [66]. Another recent study showed for the first time that under anaerobic conditions, *LM* uses a mechanism called extracellular electron transfer (EET) to transfer electrons produced in respiration to extracellular soluble and insoluble electron acceptors [69]. The same study investigated the effect of the EET mechanism for colonization of the gut. Because oxygen levels are low in the intestinal lumen, anaerobic growth capabilities strongly enhance microbial proliferation there. The growth of a mutant deficient in EET in a gut model was six-fold lower than that of the wild-type Listeria with full EET capability [69]. This finding suggests that the EET mechanism helps *LM* to respire under anaerobic and facilitate the development of Listeriosis following *LM* ingestion. However, it is currently unknown whether the newly discovered EVs also participate in EET. If so, strategies to inhibit EV-mediated EET might be effective in preventing or mitigating the severe health problems associated with Listeriosis. Previously, Dr. Worden's research group showed for the first time that using the EET mechanism, Shewanella oneidensis cells can locate insoluble electron acceptors in an anaerobic environment [70]. Using a set of motility assays, it was shown that the cells use reduced riboflavin as both an electron shuttle and an attractant to tactically move toward local

insoluble electron acceptors to respire under anaerobic conditions. In this work, we were interested in test if *LM* tactically moves toward external electron acceptors (similar to Shewanella oneidensis), to develop electrochemical immunosensors for detection EVs from *LM*, and to test the hypothesis if these EVs participate in anaerobic respiration of *LM* via EET. To perform the needed experiments to test the mentioned hypothesis, we needed to isolate EVs from LM, confirm motility of the used strains of *LM*, and develop a chemically defined media which allows studying tactic movement (chemotaxis) of LM under a controlled growth condition. Chapter 5 discusses how these steps were performed.

2 Enzyme Linked Immunosorbent Assay (ELISA)

2.1 Introduction

Immunoassays are a class of analytical techniques that are perhaps the most commonly used method for measuring biological compounds in translational and clinical research [71]. Immunoassays are developed based on the principle of the immune system wherein a specific antigen (analyte) reacts with specific antibodies [72]. Epitopes on the antigen and the binding site of the antibody have specific chemical structure and spatial configuration. Therefore, an antibody can only bind to an antigen, which has the complementary epitope for the antibody's binding site. This selective, specific, and stable formation of the antibody-antigen complex makes immunoassays highly specific [73]. Immunoassays are widely applied for clinical, pharmaceutical, and environmental applications due to their intrinsic advantages such as being high throughput, very specific and sensitive (due to the highly selective and stable antibody-antigen binding), adaptable to a wide range of analytes, and relatively cost effective [74].

Enzyme-linked immunosorbent assay (ELISA) is a type of immunoassay that uses an enzyme-linked antibody to measure and detect an analyte. In a conventional ELISA, the target analyte is immobilized on the surface of a microplate (directly or via a capture antibody) and then complexed with an enzyme-linked antibody [18]. The amount of bound enzyme is directly related to the analyte concentration. The bound enzyme catalyzes a reaction in which its products produce a measurable signal which is related to the bound enzyme concentration. Therefore, by measuring the enzyme-induced signal, the analyte concentration can be measured.

The global market for ELISA was valued at USD 1,583.4 million in 2016 and is estimated to reach USD 2.5 billion by 2025 with a compound annual growth rate (CAGR) of 5.1 %. ELISA market is predicted to increase significantly in the next five years due to the high demand for cost-effective

diagnostic tools and the increasing incidence of infectious diseases and cancer [75]. For example, the massively increasing rate of COVID-19 cases has produced a high demand for antibody detection kits globally. The global market for COVID-19 antibody detection kits has a value of USD 5,406 million in 2020, with a CAGR of 10.16 % [76].

In this work, we have been interested in integrating the advantages of an optical ELISA and an amperometric transducer to develop a sensitive and specific EI. Because a conventional optical ELISA in a 96- microplate provides a high throughput platform to evaluate the efficiency of reagents and antibodies for detection of a specific antigen, we performed optical ELISAs to validate the functionality of antibodies and reagents which were going to be used in our EI. In this chapter, developed optical sandwich ELISAs for two different analytes will be discussed. Horseradish peroxidase (HRP) was used as the reporter enzyme for the following reasons: HRP is the most commonly used enzyme in ELISAs due to a relatively high turnover number, smaller molecular size, and stability, which makes the antibody-conjugation process more effective; it is relatively cost-effective [77]; there is a versatile range of colorimetric and redox active substrates available for HRP which makes it suitable for being used in both optical ELISAs and electrochemical immunosensors[78].

An optical sandwich ELISA was developed using 3,3', 5,5”-tetramethylbenzidine (TMB)- H_2O_2 and catechol-H_2O_2 system for detection of a model antigen (mouse IgG). This chapter will discuss how the optical ELISA helped to evaluate the functionality of antibodies and study the source of background signal, which was observed in the EI.

Another optical ELISA was developed to detect extracellular vesicles (EVs) produced by breast cancer cells. EVs are lipid bilayer-delimited particles that are released by cells to the extracellular environment [79]. Several studies have shown that cancer cells release more EVs than normal cells

and cancer EVs contain surface biomarkers and cargo specific to their cell of origin [80-82]. Biological fluids contain a large amount of EVs, which have stable sources of biomarkers that are unique to their cell of origin. EVs derived from cancer cells can be used as a biomarker in liquid biopsy to provide a minimally invasive approach for cancer diagnosis [83]. In this project, we were interested to develop an optical ELISA for the detection of EVs from breast cancer cells. Studies have shown that the concentration of some tetraspanin proteins such as CD63 and CD81 are elevated in EVs produced by breast cancer cells, and they are used as classical biomarkers for cancer detection [84]. CD63 and CD81 are glycoproteins that are present on the membrane of EVs [85]. We have used the optical ELISA to evaluate which surface biomarker (CD63 or CD81) would be more efficient for detecting breast cancer cells. Once the proper surface biomarker is known, an electrochemical immunosensor would be developed to detect EVs from breast cancer cells.

2.2 Experimental Methods

2.2.1 Materials and Instrumentation

Maxisorp Immuno Clear Standard Modules 96 microplates (Nunc, 469914) and 1-Step™ Ultra TMB-Blotting solution (37574) were purchased from Thermofisher Scientific. Mouse IgG, anti-mouse IgG antibody (ap124), HRP-conjugated-goat anti-mouse IgG (a5278), 3-methyl-2-benzothiazolinone hydrazone (MBTH), catechol, Bovine serum albumin (BSA, a3059), and TWEEN 20 were obtained from Sigma Aldrich. CD63 Antibody-HRP conjugated (NBP2-42225H) was obtained from Novus Biologicals. Anti-CD63 (215-820) was obtained from Ancell corporation. CD81 antibodies were obtained from Cosmo Bio US. MF-Millipore™ Membrane Filter, 0.05 μm pore size (VMWP02500) and Millex-GP Syringe Filter Unit, 0.22 μm, polyethersulfone, 33 mm, gamma sterilized (SLGP033RB) were purchased from Millipore Sigma. Ultrapure water (18.2 MΩ) was produced by a Nanopure-UV four-stage purifier (Barnstead International, Dubuque, IA); the purifier was equipped with a U.V. source and a final 0.2 μm filter.

Ultrapure water was used in all aqueous solutions. A Synergy H1 hybrid multi-mode plate reader was used to measure the absorbance in the plates.

2.2.2 ELISA Development

2.2.2.1 ELISA for Mouse IgG

In this section, we discuss the optical ELISA for a model antigen, mouse IgG. The optical ELISA was conducted to choose the best antibodies for the assay and optimize some of the experimental conditions such as antibody dilution. Once the optical ELISA was optimized, it was integrated with an electrochemical transducer to develop an electrochemical immunosensor.

First, 200 µl of [1:333] dilution of the primary antibody (ap124) in 50 mM phosphate buffer at pH 7.4 was added to the wells of a 96-well plate, and the microplate was incubated at 4°C overnight. Next day, after being washed with PBS, wells were filled thoroughly with 1% BSA in phosphate buffer to block the sites, which have the potential for causing non-specific binding, and the plate was incubated at room temperature for one hour. After being washed with PBS, 200 ul of the samples containing different concentrations of mouse IgG prepared in 1% BSA were added to each well. The plate was incubated at room temperature for two hours. Then, wells were washed five times with a washing buffer containing 0.5% TWEEN 20 in PBS. Next, 200 µl of [1:333] dilution of the detection antibody (a5278) in 1% BSA in 50 mM phosphate buffer at pH 7.4 was added to the wells. The plate was incubated at room temperature for an hour (Note: because HRP is light sensitive, this step and the consequent steps were performed in a dark space to avoid deactivation of the HRP). Next, wells were washed thoroughly for 5 times with the same washing buffer with

washing buffer (Figure 2.1). The optical signal was measured using TMB-H_2O_2 system or catechol-H_2O_2 system which have been discussed in the next section.

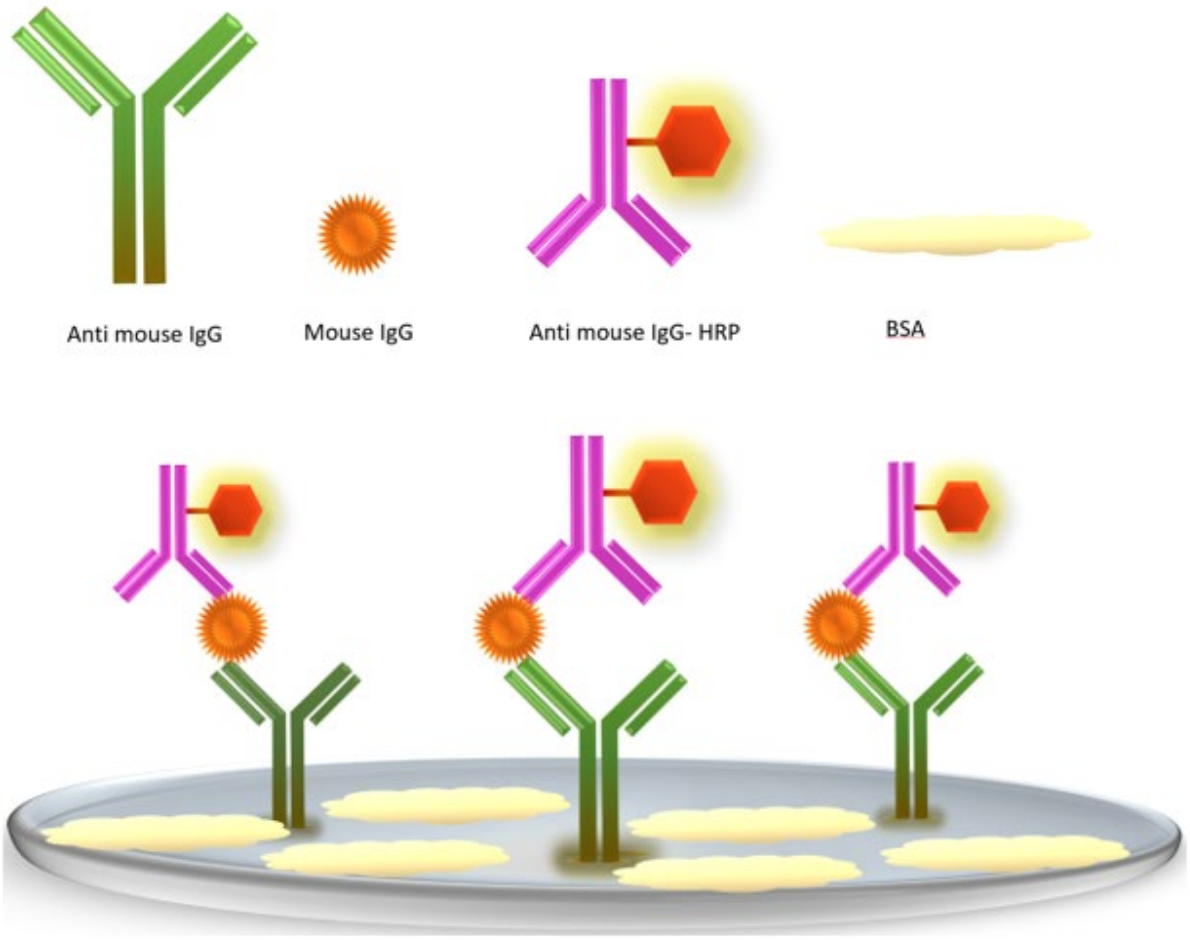

Figure 2.1. Molecular structure of the ELISA for mouse IgG on the bottom of a well in a microplate.

2.2.2.2 ELISA for EVs from Breast Cancer Cells

All eukaryotes and prokaryotic cells release extracellular vesicles (EVs) into the extracellular environment. EVs are lipid bilayer-enclosed, cytosol-containing spheres that play an important role in intracellular transfer of signaling molecules, functional proteins, nucleic acids, lipids, and virulence factors [86]. Biological fluids contain a large amount of EVs which have stable sources

of biomarkers that are unique to their cell of origin. EVs derived from cancer cells can be used as biomarker in liquid biopsy to provide a minimally invasive approach for cancer diagnosis [83]. Studies have shown that the concentration of some tetraspanin proteins such as CD63 and CD81 are elevated in EVs produced by breast cancer cells and they are used as classical biomarkers for cancer detection [84]. CD63 and CD81 are glycoproteins which are present on the membrane of EVs [85]. Herein, we present an optical ELISA to detect EVs from breast cancer cells using CD81 and CD81 as the surface biomarkers. To develop the ELISA, we needed to culture breast cancer cells to collect EVs. The procedure for the collecting EVs from breast cancer cells is discussed in the next section.

2.2.2.2.1 Culturing Breast Cancer Cells

MDA-MB-231 cells were seeded at a density of 1-3 million cells /75 cm^2 flask in 10 mL of growth medium and then incubated for 48 h in medium containing 10% Exo-depleted FBS at 37˚C. At least 5 flasks were used. The media was transferred from each plate to a separate 15 mL tube. The tubes were Centrifuged at 600 x g for 10 minutes. The supernatant from each tube was transferred to a new 15 mL tube and the pellet (included dead cells and cell debris) was discarded. Tubes were centrifuged at 2,000 x g for 30 minutes. The supernatant was combined into a 50 mL tube or stored at -20 C until ready to use.

2.2.2.2.2 Purification of EVs

The supernatant was filtered through a 0.22 µm filter and the filtrate was collected in a 50 mL tube (Figure 2.2). The collected solution was passed through a vacuum filtration (QIAvac 24 Plus) using the 50 nm filter (Figure 2.3, the filter was changed for every 20 mL of solution). The vacuum filtration was continued until the solution was just above the filter. Then, 5 mL of the PBS was

added, and the filtration continued until three-quarters of the filter space contained PBS. The solution above the filter contained the concentrated EVs. The EVs were stored at -80 C.

Figure 2.2. Filtering media solution through a 0.22 µm filter

Figure 2.3. Filtering media solution through a filter with a 50 nm pore size filter using vacuum

2.2.2.2.3 Quantification of EVs by NTA Analysis

Nanoparticle tracking analysis (NTA) was used to quantitate extracellular vesicles (EVs) in the collected sample solution from the previous step. NTA is a commonly used technique to determine the particle size distribution and concentration of a sample containing nanoparticles [87]. Figure 2.4 shows the size distribution of the EVs. The average size of the EVs was found to be 100 nm.

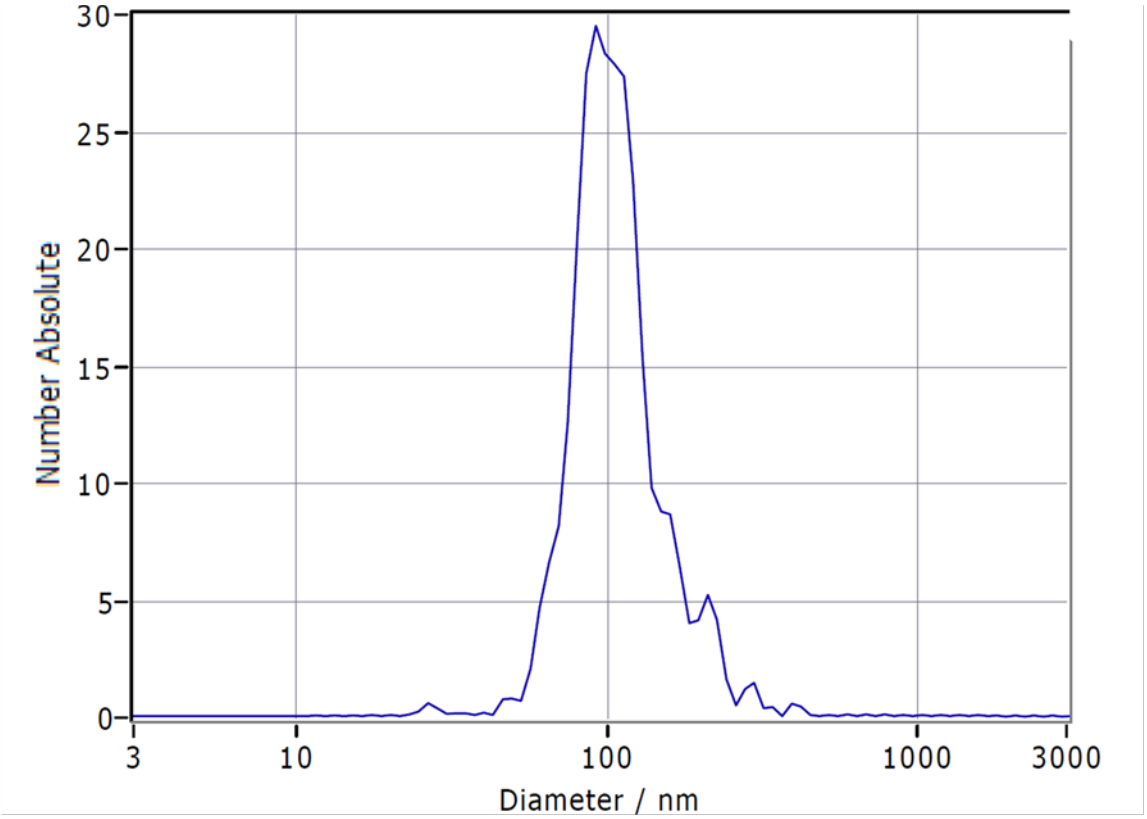

Figure 2.4. Size distribution of the EVs. NTA analysis showed an average diameter of 100 nm for the collected EVs from breast cancer cells

2.2.2.2.4 ELISA Development for EVs from Breast Cancer Cells

To begin, 100 ul of 20 ug/ml anti-CD63 or anti-CD81 in 50 mM Phosphate buffer pH 7.4 was added to each well in MAXisorp 96-well plate (Nunc) and the microplate was incubated at 4°C overnight. After being washed with PBS, 250 ul of 1% BSA was added to each well to block the sites, which have the potential for causing non-specific binding. Plate was incubated at room temperature for one hour. Wells were washed with PBS, 100 ul of the samples containing different concentration of EVs was added to each well. Samples were prepared in 100 mM PBS pH 7.4. The plate was incubated at room temperature for eight hours on a microplate shaker for gentle mixing (Note: Because EVs are relatively larger and heavier particles, they can precipitate when the sample is left stagnant). After being washed with PBS thoroughly (5 times), 100 ul of 20 ug/ml

detection antibody-HRP in 2% BSA in 50 mM PBS buffer pH 7.4 was added to each well. The plate was incubated at room temperature for one hour. Then, wells were washed with PBS 5 times (Figure 2.5, Note: because EVs can be lysed by TWEEN 20, washing buffer was prepared without the detergent).

Then, 100 ul of TMB-H2O2 was added to each well and enzymatic reaction between TMB-H2O2 and HRP happened for 10 minutes until a bright blue color was formed (Note: both TMB and the

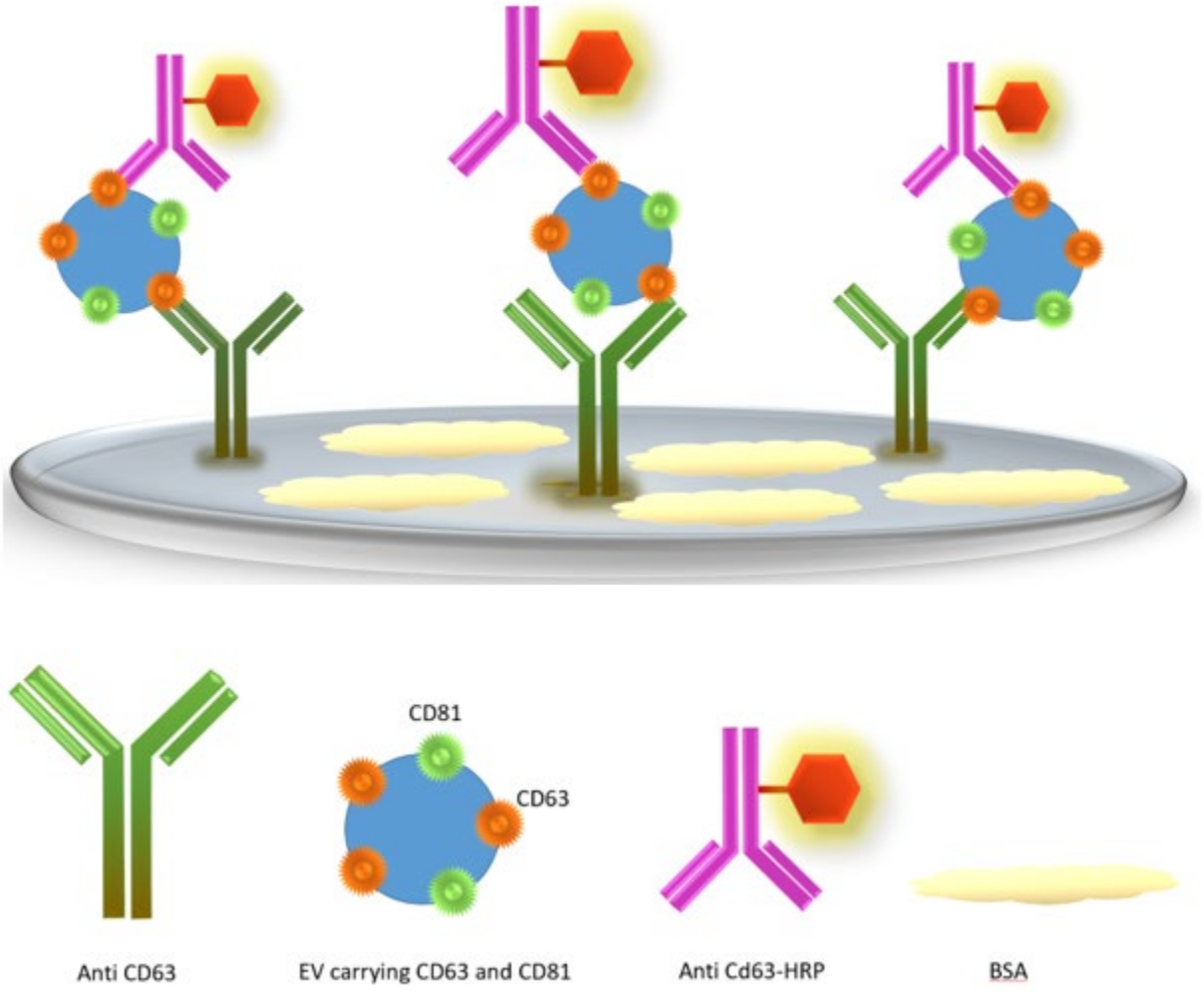

Figure 2.5. Molecular structure of the ELISA for EVs from breast cancer cells on the bottom of a well in a microplate.

products of the reaction catalyzed by HRP are light sensitive and this step must be done in a dark space). Then, 100 ul of 1 M sulfuric acid was added to each well to stop the reaction (yellow color formed). Finally, absorbance was read at 450 nM.

2.2.3 Color Formation Reaction

Two different cosubstrates, TMB and catechol, were used for HRP. TMB is a commonly used substrate for HRP in optical ELISAs. Initially the optical ELISA was performed with TMB to optimize the experimental conditions. Then, an optical ELISA was performed with catechol as this substrate was going to be used in the EI. Oxidation of catechol with HRP in the presence of H_2O_2 produces O-quinone which is an electroactive chemical.

2.2.3.1 TMB-H_2O_2 System

In this case, 200 ul of TMB-H2O2 was added to each well and enzymatic reaction between TMB-H2O2 and HRP happened for 10 minutes until a bright blue color was formed (Note: both TMB and the products of the reaction catalyzed by HRP are light sensitive and this step must be done in a dark space). Then, 100 ul of 1 M sulfuric acid was added to each well to lower pH and stop the reaction. Lowering pH induce formation of a relatively stable yellow colored product which can be measured at 450 nm [88]. Figure 2.6 shows the reaction the steps leading to formation of the colored products.

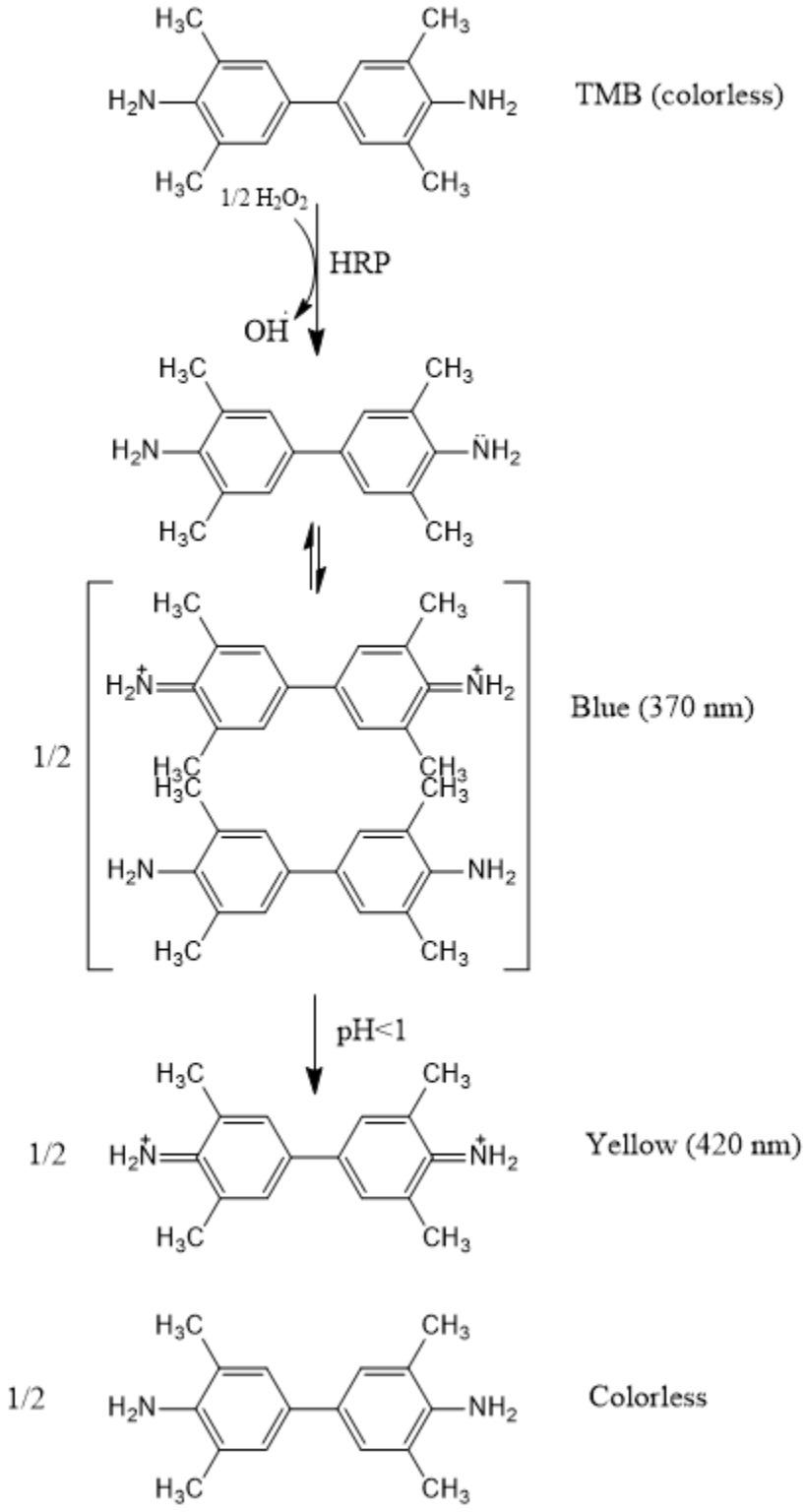

Figure 2.6. Reaction steps between TMB-H2O2 and HRP to form colored products.

2.2.3.2 Catechol-H2O2

In the case of catechol-H_2O_2, 200 µL of a solution containing 5 mM catechol and 1.5 mM H2O2 was added to the wells and the plate was incubated in a dark space for 20 minutes. Then, 100 µM of 10 mM MBTH (prepared in deionized water) was added to the wells and absorbance was read at 505 nm. Catechol reacts with HRP in the presence of H_2O_2 to produce *o*-quinones which reacts with 3-methyl-2 benzothiazolinone hydrazine (MBTH) to produce pink colored products (Figure 2.7) [89].

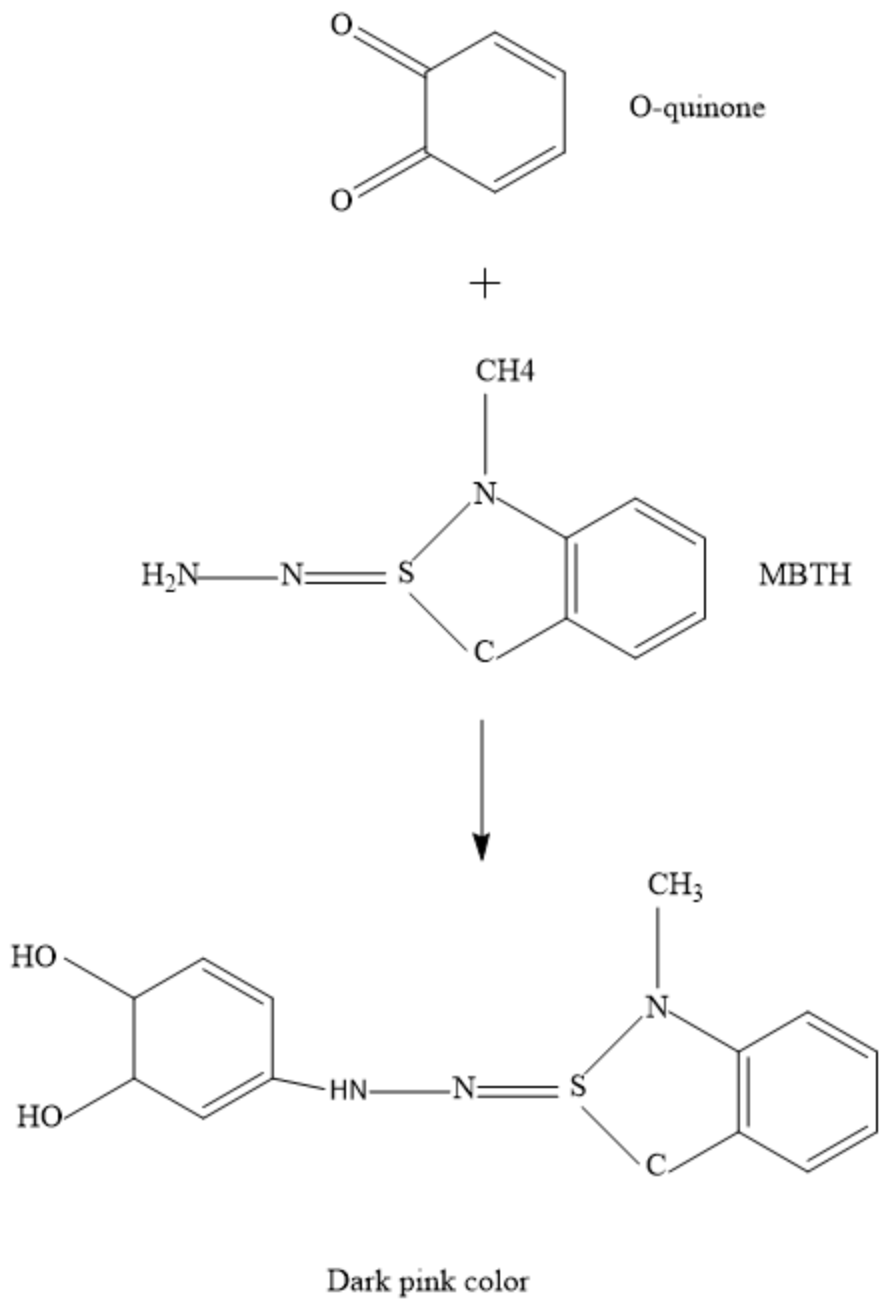

Figure 2.7. Reaction steps between o-quinone and MBTH for form pink colored products.

2.3 Results and Discussion

2.3.1 ELISA for Mouse IgG

One of the key parameters that had a significant effect on the performance of the ELISAs was dilution factor of the capture antibody and the detection antibody. Different dilutions of antibodies were used to design ELISAs (Figure 2.8). According to the results shown in Figure 2.8, a dilution of [1:333] gave the best sensitivity and this dilution was used in the design of EI.

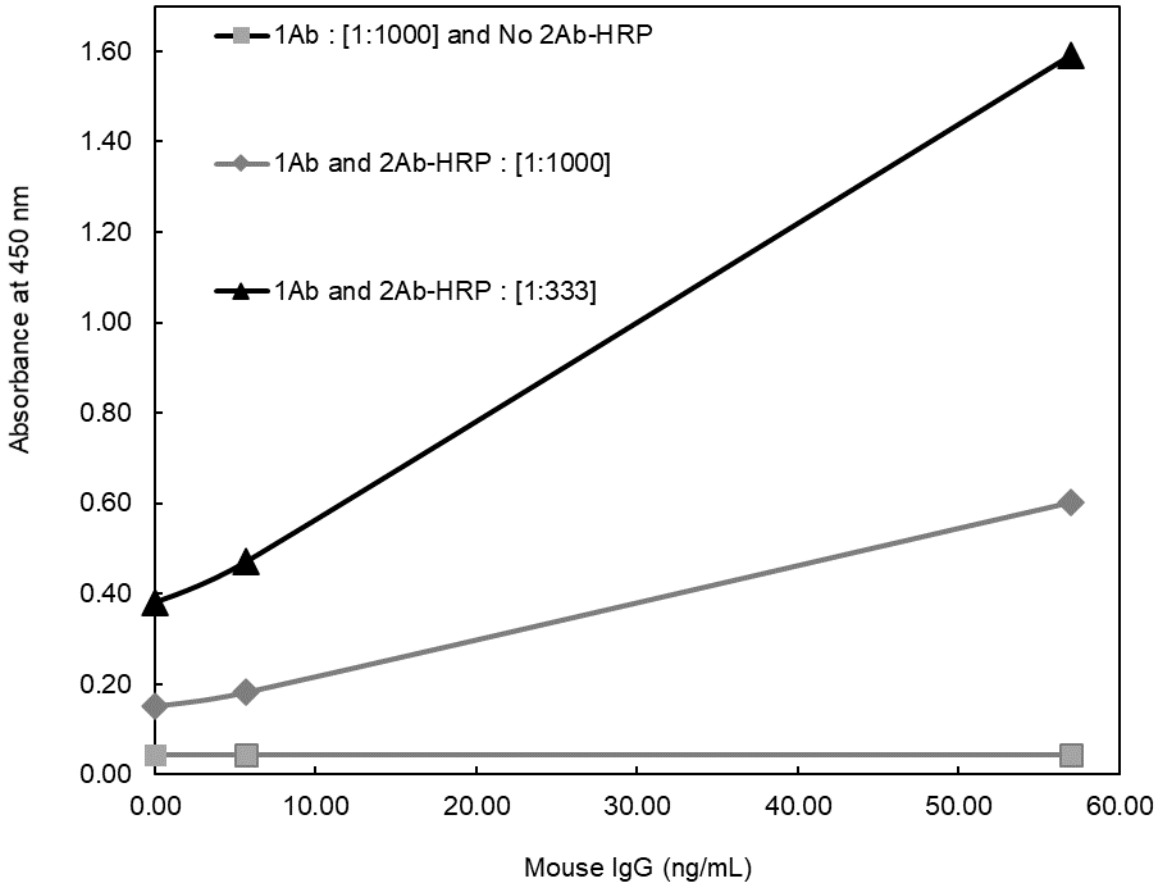

Figure 2.8. Optical ELISA for the mouse IgG. Mouse IgG was detected in a sandwich ELISA with a detection antibody labeled with HRP using TMB-H2O2 substrates.

An optical ELISA was also developed using catechol as the cosubstrate for the HRP as catechol was going to be used in the electrochemical immunosensor (Figure 2.9). According to this result, using catechol caused a relatively higher background signal compared to TMB-H_2O_2 system. A significant background signal was also observed in the EI using catechol-H_2O_2. Therefore, a set of control experiments were performed to investigate the source of the high background current when using catechol as the cosubstrate (Figure 2.10). According to Figure 2.10, a significant background signal was observed for the case of catechol alone and the case of the catechol with H_2O_2. These results can be attributed to the autoxidation of the catechol and the fact that a small amount of catechol might be oxidized in the presence of H_2O_2. Because this background current was also observed in the case of the EI using catechol-H_2O_2 as the substrates, a design of experiment was performed in MINITAB (discussed in the next chapter) to optimize catechol and H_2O_2 concentrations and thereby maximizing the signal to background ratio.

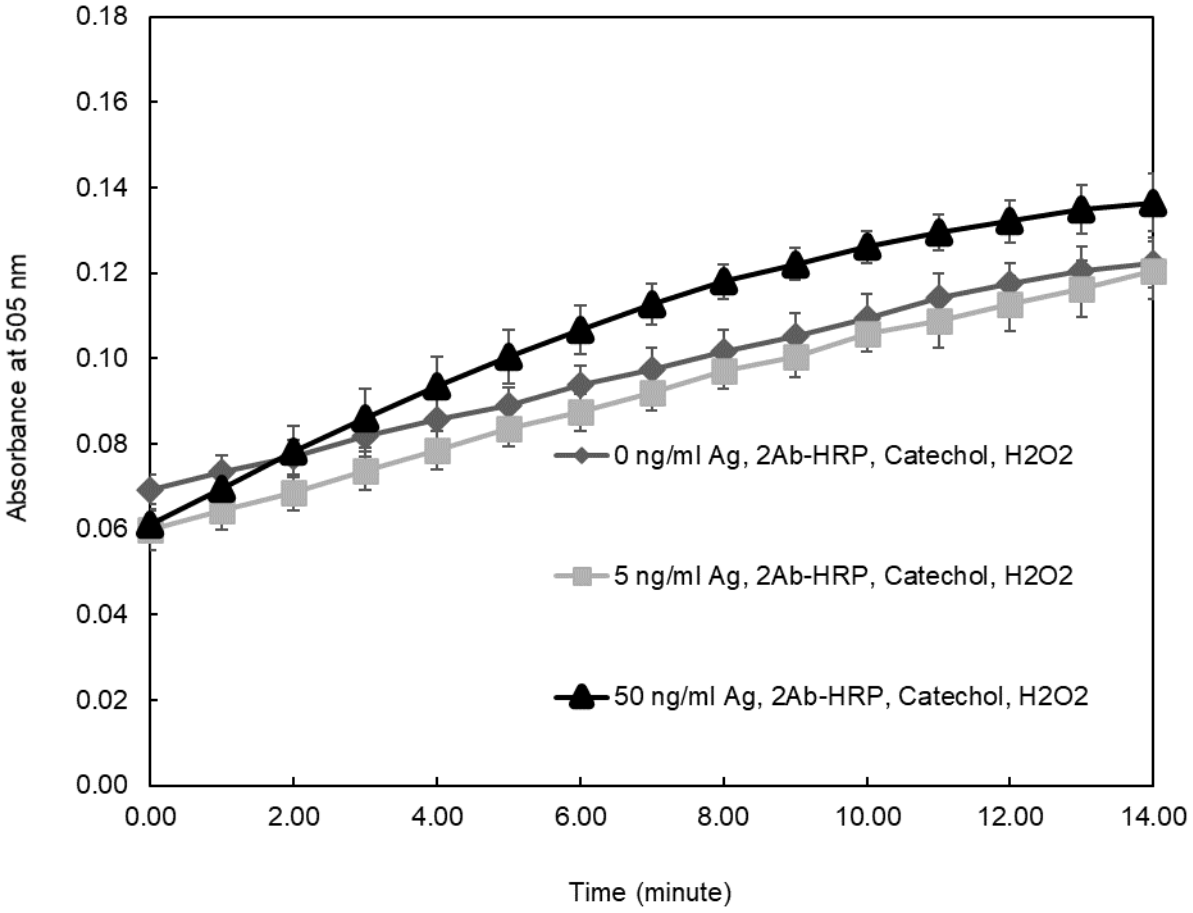

Figure 2.9. Optical ELISA for the mouse IgG. Mouse IgG was detected in a sandwich ELISA with a detection antibody labeled with HRP using catechol-H2O2 substrates.

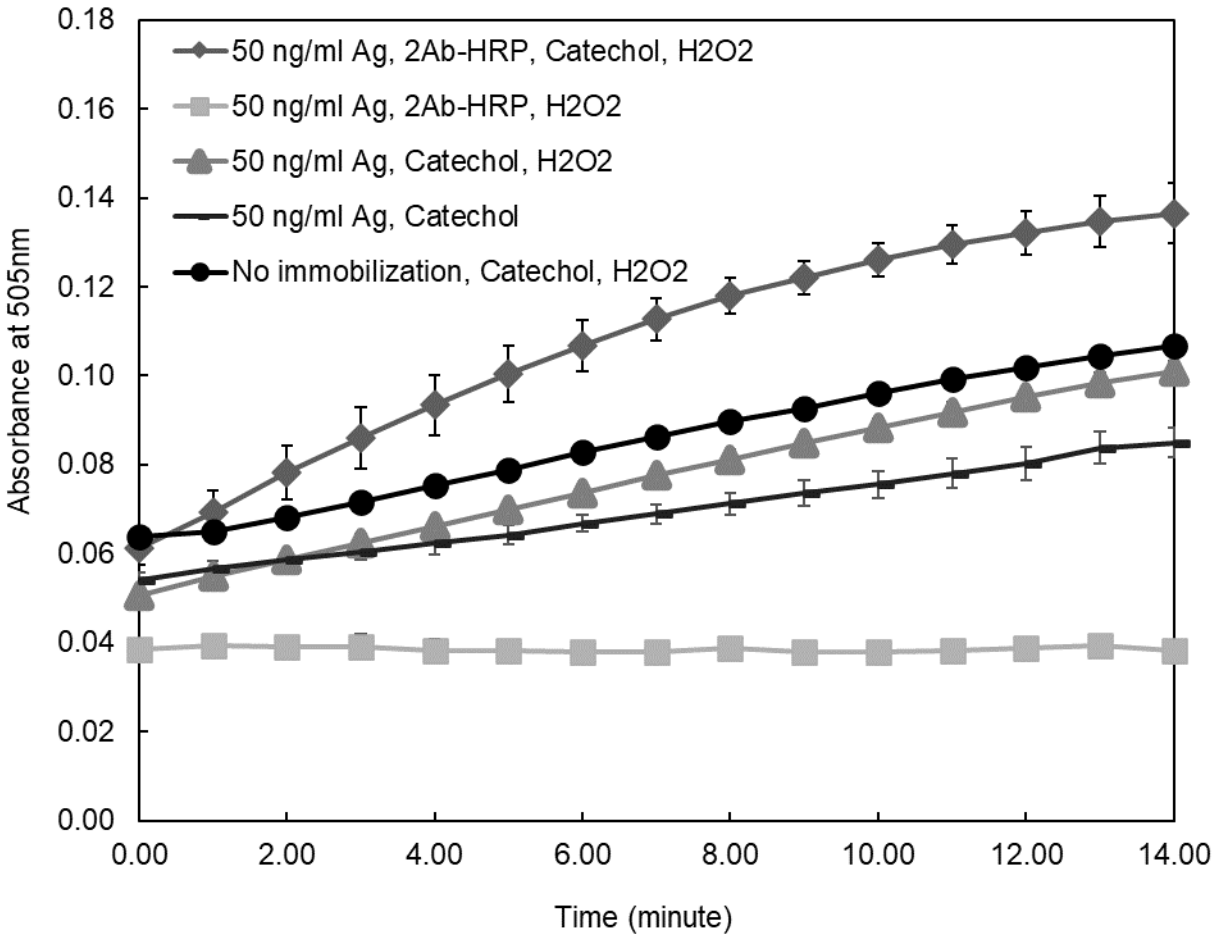

Figure 2.10. Control experiments for measuring the background signal cause by non-specific binding, H2O2 and catechol.

2.3.2 ELISA for EVs from Breast Cancer Cells

In this work, we were interested to develop an EI for detection of EVs from breast cancer cells. Before developing the biosensor, it was important to find a surface biomarker on the EVs that its concentration is high enough to detect EVs. In several studies, CD81 and CD63 were reported as two surface biomarkers on EVs from breast cancer cells that commercial antibodies were available for them. Optical ELISAs were developed to select the biomarker that gives a better sensitivity for detection EVs. In the first attempt, an ELISA was developed using antibodies against CD81 (Figure 2.11). Despite trying two sources of CD81 antibody and changing their concentrations

used in ELISA, the sensitivity did not improve. Therefore, antibodies against CD63 were used to develop the ELISA (Figure 2.12). Figure 2.12 shows that antibodies against CD63 significantly enhanced the dose response for detection of the EVs. These results suggest that antibodies against CD63 should be used in development of an EI.

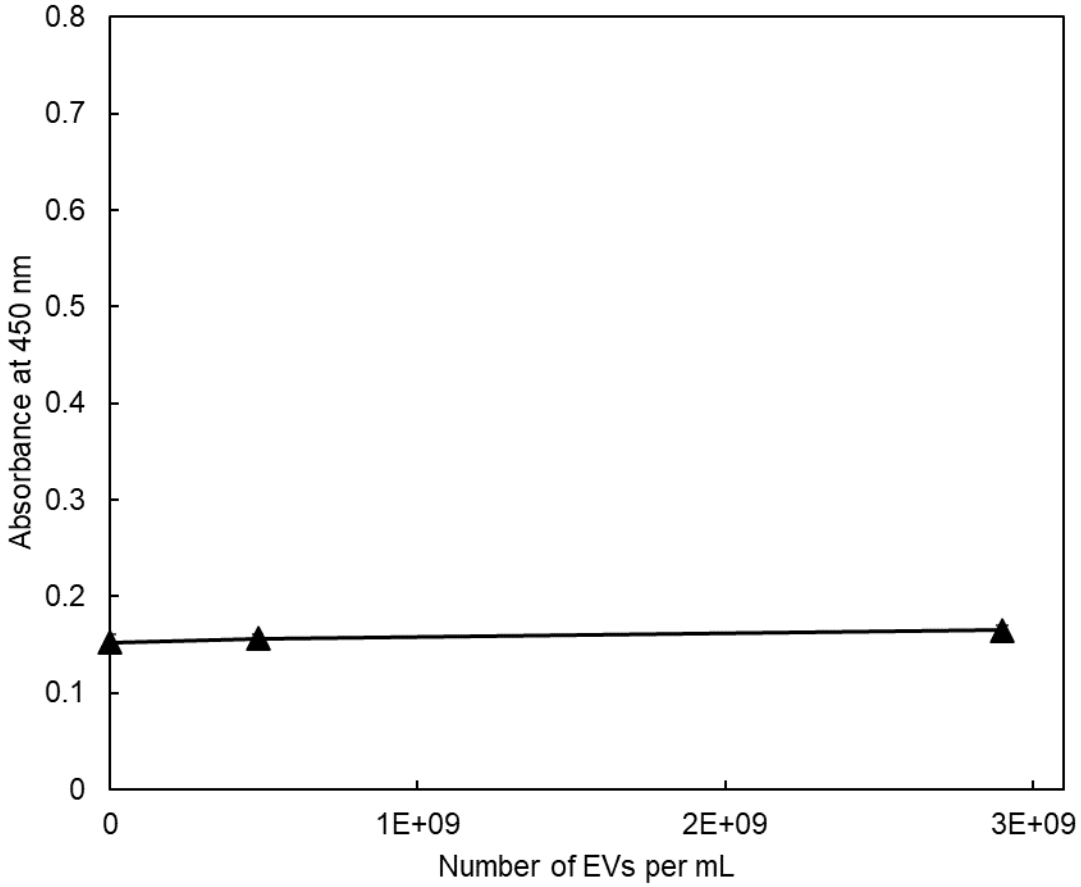

Figure 2.11. ELISA for EVs from breast cancer cells using CD81 as the surface biomarker.

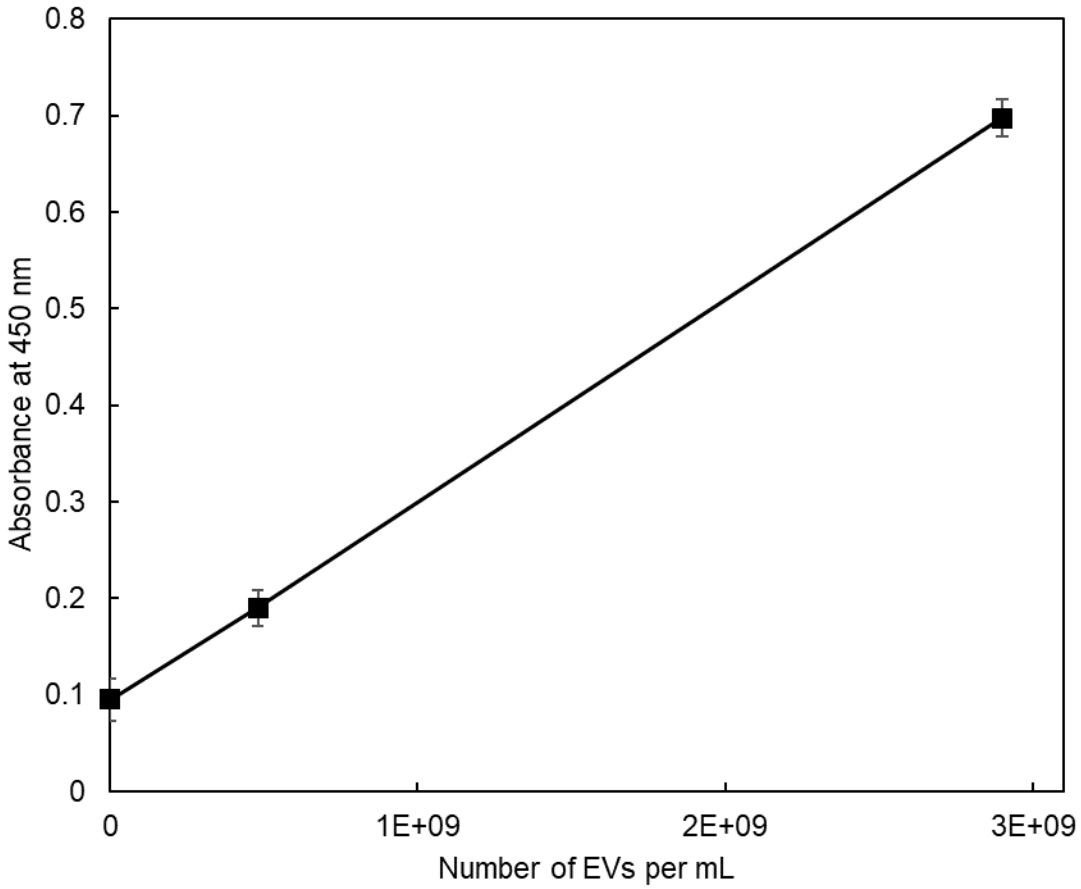

Figure 2.12. ELISA for EVs from breast cancer cells using CD63 as the surface biomarker.

2.4 Conclusions

In this chapter, it was discussed how the conventional optical ELISA was used as a high throughput assay to optimize experimental conditions before developing EIs for an analyte of interest. Optical ELISAs was developed for mouse IgG to optimize antibody concentrations and to study the background signal observed in the EI. Optical ELISAs were also developed for detection of EVs from breast cancer cells. With the aid of optical ELISAs, a surface biomarker on EVs from breast cancer cells (CD63), was found. This surface biomarker provided a good sensitivity of detection for EVs from breast cancer cells. The results and finding from the optical ELISAs were crucial for development of the EI which is discussed in the next chapter.

3 Integrated Experimental and Theoretical Studies on an Electrochemical Immunosensor (EI)

3.1 Introduction

Electrochemical biosensors are analytical devices that detect analytes by transforming a biochemical reaction into a quantitative, electrical signal. This class of biosensors has proven valuable in research, quality control, food safety, medical diagnosis, and monitoring of therapeutic efficacy [25]. Miniaturized amperometric biosensors that use redox enzymes to generate an electric current in response to voltage applied at a working electrode have been successfully commercialized; personalized blood glucose meters used by diabetics represented 85% the total biosensor market in 2008 [90]. By 2013, the worldwide market for glucose-monitoring biosensor systems was estimated to be billions of dollars per year, with screen-printed-electrode (SPE) arrays that served as single-use biosensor "strips" representing two-thirds of that market [91]. The disposable, redox-enzyme-based biosensor market is being further expanded by commercializing glucose-monitoring systems for animals [92].

Optical immunoassays based on the exceptionally high binding selectivity and affinity of biological recognition molecules (predominantly antibodies, but also aptamers[93]) have been commercialized for applications in many fields, including environmental protection, food safety, and healthcare. The projected global market for lateral-flow immunoassays has risen at a compound annual growth rate of 8.1% since 2017 and is expected to reach $8 billion in 2022 [94]. Immunoassays typically involve a "sandwich" molecular architecture, in which immobilized capture antibodies first bind target-analyte molecules present in the liquid sample. Then secondary antibodies labeled with reporter molecules that generate an optical signal also bind the analyte molecules. The resulting molecular "sandwiches" consist of an analyte molecule held between

primary- and secondary-antibody molecules. To estimate the analyte concentration, the surface concentration of bound reporter molecules is measured by the intensity of the optical signal they generate. A calibration curve is used to convert the reporter molecule's concentration into the analyte concentration [30]. Commonly used reporter molecules for immunoassays include redox enzymes whose products can be measured optically, such as horseradish peroxidase (HRP). HRP offers multiple advantages as a reporter. It is robust, has a relatively small molecular size, is inexpensive, is readily bound to antibodies in an active form, has a high turnover rate, and can oxidize a wide range of substrates to yield optically active products [31, 32].

Whereas virtually all commercial immunoassay systems involve optical detection, the benefits of integrating electrochemical biosensors and immunoassays have been recognized [10]. Such hybrid electrochemical immunosensors (EI) have the potential to combine the advantages of immunoassays (extremely high sensitivity and selectivity) with those of electrochemical biosensors (reproducible, quantitative, continuous electrical output). The electrical output is achieved by forming a sandwich molecular architecture on the working electrode, and the reporter molecule triggers an electrical signal. Redox enzymes are commonly used as EI reporters because some of their reaction products can be either oxidized or reduced at the working electrode, resulting in an electric current that serves as the EI's output. This approach offers exceptional versatility because an EI biosensor could be developed for virtually any analyte for which antibodies can be developed. Also, inexpensive, disposable, SPE arrays designed to be read by portable meters similar to glucose meters EI could be mass-produced. The resulting EI platform would enable an extremely wide range of molecular and cellular analytes to be accurately measured with high sensitivity and selectivity, ease of use, low cost, and portability [26-29, 95].

Prototype EI systems have been developed for healthcare applications. Sanchez-Tirado et al. fabricated an EI to measure cytokines used as markers of inflammation [96]. Tallapragada et al. developed an EI for human epidermal growth factor receptor 2 (HER2) that had a detection limit of 4 ng/mL [97]. Dempsey et al. described a disposable, printed lateral flow EI for human cardiac troponin T (cTnT) [98]. The reporter used in all of these studies, HRP, generated an oxidized product that was electrochemically reduced at the working electrode, resulting in a continuous amperometric output.

However, commercial implementation of EI systems has been hampered by the complexity of the multiple molecular mass-transfer, binding, and reaction steps that give rise to the electrical signal. This complexity complicates efforts to design new EIs that achieve specified performance metrics, including the lower detection limit and sensitivity (defined as the change in output per unit change in analyte concentration). Fabrication methods and operating conditions needed to achieve these metrics are expected to vary between EI systems due to factors including analyte-antibody binding affinities, the concentrations of primary antibodies bound to the electrode, and the kinetics of both the reporter enzyme's reaction and the electrochemical reaction. These kinetics will, in turn, be influenced by the liquid sample's properties, including its pH and its concentrations of the analyte, and substrates for the enzymatic reaction. Moreover, the concentrations of redox-active interferents in the sample may limit the working electrode's voltage.

The development of robust product-design algorithms for new EI systems that meet specified performance metrics would be aided by mechanistic mathematical models that quantitatively describe the rates of the key molecular mass-transfer, binding, and reaction steps. Such models would enable the step(s) that limits performance to be identified and guide strategies to overcome such limitation(s). To date, few mechanistic models of HRP-based EIs have been reported [33-

37], and these models have not been sufficiently comprehensive to predict how the output would vary with key independent variables, including the working electrode's applied voltage (*E*), the pH, and the concentrations of HRP's substrates. Such models are needed to help design EIs, identify factors that limit their performance properties, and guide research strategies to optimize EI systems.

Mechanistic models would also help support petitions for U.S. Food and Drug Administration (FDA) approval of EI systems for healthcare applications. The FDA requires that stringent accuracy and consistency standards be met by portable glucose monitoring systems while in the hands of lay users [99], and similar requirements would be expected for EIs. Mechanistic models would enable rapid, *in-silic*o hypothesis testing, including "what-if" studies to assess whether non-standard use by lay users could result in dangerously incorrect readings.

This chapter addresses the need for such mechanistic models by presenting a novel, integrated experimental and mathematical framework to characterize EI performance and then using the framework to optimize performance of a novel EI that can detect a target protein (mouse IgG) at the ng/ml level. The framework includes three components. The first is a detailed mechanistic model that can predict the rates of the individual mass-transfer and reaction steps that give rise to the EI's amperometric output. The second is a statistical-design-of-experiments approach that generates an empirical, statistical model describing the effects of key independent variables on the EI's output. This statistical model is used both to optimize the EI system and to help validate the mechanistic model. The third is an integration of dimensional analysis with principles of flux-control theory to quantify the extent to which individual mass-transfer and reaction steps limit the EI's sensitivity and output current (*J*). The chapter concludes by discussing the utility of the

integrated experimental and mathematical framework for future design, optimization, and validation of EI systems.

3.2 Experimental Methods

3.2.1 Materials and Instrumentation

Thioctic acid, sodium phosphate (monobasic and dibasic), mouse IgG, anti-mouse IgG antibody (ap124), HRP-conjugated-goat anti-mouse IgG (a5278), TWEEN 20, H_2O_2), *C*, and N-hydroxysulfosuccinimide sodium salt (NHS) were obtained from Sigma Aldrich. MES buffered saline packs, and 1-ethyl-3-(3-dimethylaminopropyl carbodiimide hydrochloride) (EDC) were purchased from ThermoFisher Scientific. Ultrapure water (18.2 MΩ) was produced by a Nanopure-UV four-stage purifier (Barnstead International, Dubuque, IA); the purifier was equipped with a U.V. source and a final 0.2 μm filter. Ultrapure water was used in all aqueous solutions. Screen-printed electrodes were obtained from Conductive Technologies Inc. and Metrohm DropSens (models DRP-250BT and DRP-110SWCNT).

3.2.2 Preparation of Immunosensing Layer

The immunosensing layer was prepared by using 1-ethyl-3-(3-dimethylaminopropyl (EDC) and N-hydroxysulfosuccinimide sodium salt (NHS) chemistry to attach the primary (capture) antibodies covalently to carboxylate groups present on the DropSens array's working electrodes. EDC-NHS chemistry has been widely used to fabricate the immunosensing layers of EIs [38-40]. EDC is a zero-length cross-linker that activates carboxylate groups for covalent coupling to primary amines. The addition of NHS with EDC results in an NHS ester intermediate that reacts rapidly with primary amines, thereby increasing the efficiency of the coupling reaction [41]. Cleaned gold SPEs were dipped in 15 mM thioctic acid in ethanol for 1 h. The resulting carboxylated SPEs were washed with ethanol and dried under nitrogen. The carboxyl groups were

activated by incubating the SPEs in 100 mM MES buffer containing 5.0 mM EDC and 9.0 mM NHS at pH 4.6 for 1 h at room temperature. Electrodes were then rinsed with MES buffer and dipped in 6 μg/mL goat anti-mouse IgG antibody in 50 mM phosphate buffer at pH 7 for 2 h. The primary-antibody-functionalized SPEs were then washed with phosphate buffer. To block nonspecific binding of the target analyte (mouse IgG), the SPEs were incubated in 2 % BSA in phosphate buffer for 1 h at room temperature. The resulting functional SPEs were washed with phosphate buffer at pH 7 and stored in phosphate buffer at 4°C.

SPEs were each dipped in a standard solution having a known concentration of the target analyte (mouse IgG) in a 2% aqueous bovine serum albumin (BSA) solution in 50 mM phosphate buffer at pH 7 for 1 h at room temperature. The SPEs were then washed four times with washing buffer (0.05% TWEEN20 in 50 mM phosphate buffer at pH 7) and incubated in a [1:333] dilution of HRP-conjugated-goat anti-mouse IgG in pH 7, 50 mM phosphate buffer in 2% BSA (Figure 3.1). After 1 h, the electrodes were rinsed four times with washing buffer and stored in phosphate buffer at 4°C until the electrochemical measurements were conducted.

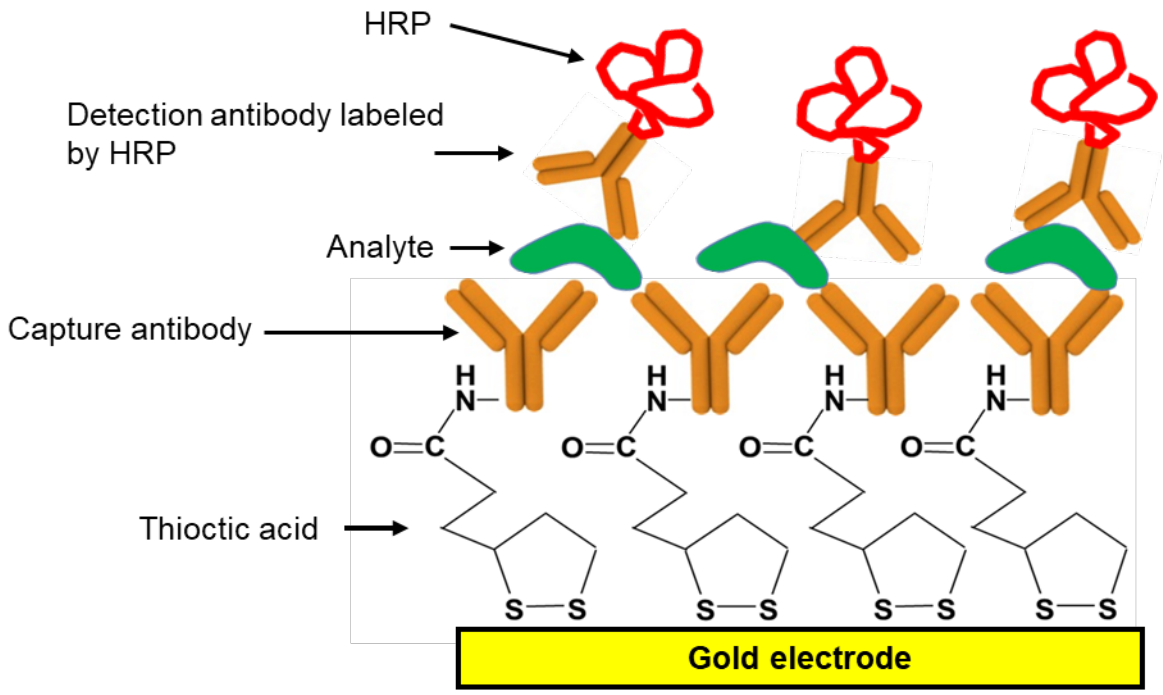

Figure 3.1. Schematic diagram of immunosensing layer showing molecular sandwiches containing the capture antibody, the target analyte, and the *HRP*-tagged secondary antibody bound to the EI's gold working electrode.

3.2.3 Electrochemical Measurement of EI Signal

The EIs were removed from the refrigerator and allowed to equilibrate at room temperature. Forty µL of a solution (subsequently referred to as the "bulk solution") containing 50 mM phosphate buffer, 1 mM H_2O_2, and 8 mM *C* were added to the SPE. Wire leads from a potentiometer (CHI 660, C.H. Instruments, USA) were connected to the EI's working, reference, and auxiliary electrodes, and reduction potential of -0.2 V relative to an Ag/AgCl reference electrode were applied to the working electrode. After about 1 min, the reduction current (i.e. the EI's signal (*J*)) reached a steady-state value, and the current level was recorded as the EI's output for that set of experimental conditions. Each EI was used once. All electrochemical potentials given in this work are relative to an Ag/AgCl reference electrode.

3.3 Optimization of EI Operating Conditions and Characterization of EI Performance Properties

A statistical design of experiment (DOE) approach was used for two purposes: (1) to determine the values of key independent variables that optimized the EI's signal and (2) to obtain an empirical equation that described the effects of the key independent variables on the EI's signal to help validate the mechanistic model. The independent variables expected to most strongly affect the performance of the EI described above included (1) the working electrode's E, (2) the bulk solution's [C], (3) the bulk solution's [H_2O_2], and (4) the bulk solution's pH [42].

A two-level half factorial design with center points and three replicates for each experiment was set up using Minitab® software (Table 3.1). For each factor, the following three levels, denoted low (-1), center point (0), and high (+1), were chosen: -0.05 V, -0.125 V, and -0.2 V for E; 1.0 mM, 4.5 mM, and 9.0 mM for [C]; 0.5 mM, 1mM, and 1.5 mM for [H_2O_2]; and 6.2, 6.6, and 7.0 for pH, respectively. To avoid electrical noise arising from the reduction of redox-active interferents in the bulk solution [100], the lowest E value was set to -0.2 V. To control the rate of C autoxidation [101], 8 mM was selected as the highest [C] value. Experiments were conducted in triplicate for each combination of factors specified by Minitab® using a constant analyte concentration of 40 ng/mL mouse IgG. Each EI's signal was calculated as the difference between the J measured first in the absence of analyte and then in the presence of the analyte. All signal data were input to Minitab®, which provided a statistical analysis of the results. The experimental conditions that Minitab® indicated were optimal for the EI were used in subsequent experiments to characterize the EI's performance properties. In these experiments, the EI signal was measured in triplicate for six concentrations of the analyte.

Table 3.1. Design of Experiments in coded units suggested by MINITAB using half factorial design. For each factor, three levels, denoted low (-1), center point (0), and high (+1), were selected: -0.05 V, -0.125 V, and -0.2 V for E; 1.0 mM, 4.5 mM, and 9.0 mM for [C]; 0.5 mM, 1mM, and 1.5 mM for [H_2O_2]; and 6.2, 6.6, and 7.0 for pH, respectively.

Run Order	E	pH	C	H_2O_2	Run Order	E	pH	C	H_2O_2
1	+1	-1	-1	+1	19	0	0	0	0
2	-1	+1	+1	-1	20	-1	-1	-1	-1
3	0	0	0	0	21	+1	+1	+1	+1
4	0	0	0	0	22	0	0	0	0
5	+1	-1	+1	-1	23	-1	+1	-1	+1
6	-1	+1	-1	+1	24	+1	-1	+1	-1
7	-1	-1	+1	+1	25	-1	+1	+1	-1
8	+1	+1	-1	-1	26	+1	-1	-1	+1
9	0	0	0	0	27	0	0	0	0
10	-1	-1	+1	+1	28	0	0	0	0
11	0	0	0	0	29	-1	+1	+1	-1
12	+1	+1	-1	-1	30	+1	-1	-1	+1
13	0	0	0	0	31	-1	+1	-1	+1
14	+1	+1	+1	+1	32	0	0	0	0
15	-1	-1	-1	-1	33	+1	-1	+1	-1
16	+1	+1	+1	+1	34	+1	+1	-1	-1
17	0	0	0	0	35	0	0	0	0
18	-1	-1	-1	-1	36	-1	-1	+1	+1

3.4 Mechanistic Mathematical Model

The mechanistic mathematical model of the EI describes the transport and reaction processes involving catechol (C), O-quinone (Q), and hydrogen peroxide (H_2O_2) that generate a current (J) at the EI's working electrode. Differential mass-balance equations describe the diffusion of these species in the x-direction (perpendicular to the electrode) through two layers (Figure 3.2) that lie between the electrode's surface at x=0 and the bulk solution: (1) the immunosensing layer between x=0 and x=L containing the antibodies and HRP, and (2) a stagnant, aqueous, diffusion layer between x=L and x=L+δ. The HRP-catalyzed conversion of C and H_2O_2 to Q is assumed to occur uniformly throughout the immunosensing layer, and the electrochemical reduction of Q to C is assumed to occur on the electrode's surface. The bulk solution is assumed to be well-mixed, with the concentrations of all chemical species remaining constant at their initial values [102]. Mass

transfer is assumed to follow Fick's law, with a diffusion coefficient (D) that is assumed to be the same for Q, C, and H_2O_2 but to vary between the diffusion layer (D_δ) and the immunosensing layer (D_L).

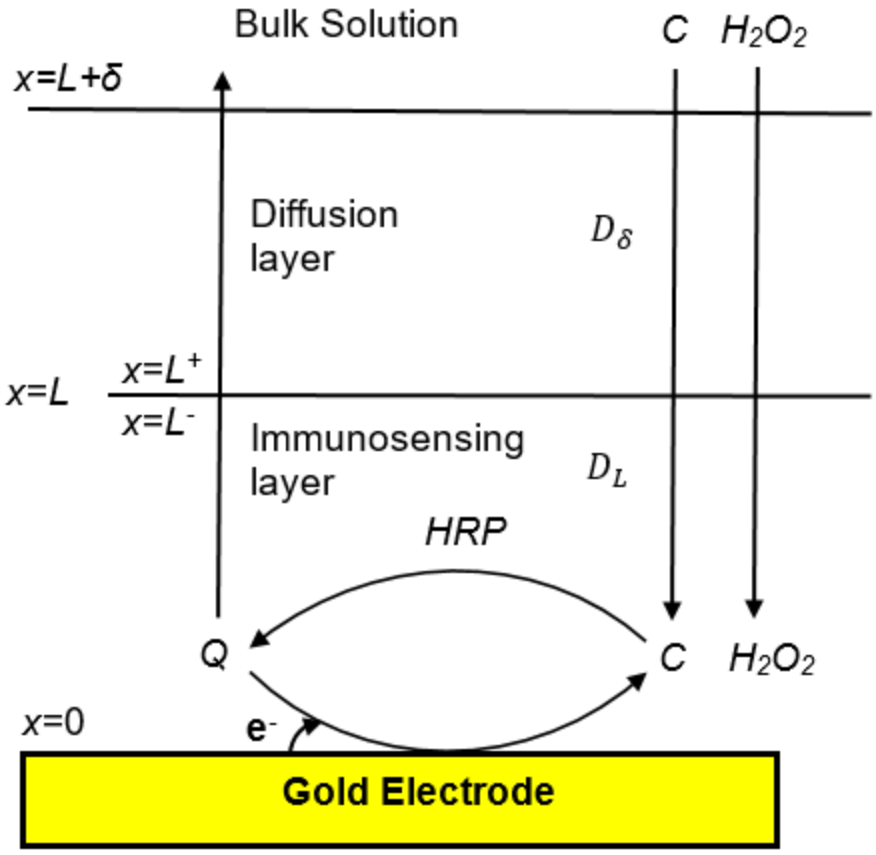

Figure 3.2. Schematic representation of diffusional mass-transfer, enzyme catalysis and electrochemical reaction steps happening on the biosensor interface.

The HRP concentration and maximum reaction rate constant (V_{max}) are assumed to be uniform throughout the immunosensing layer [103].

3.4.1 Kinetics of Enzymatic and Electrochemical Reactions

The non-linear, ping-pong kinetic mechanism describing HRP oxidation of C in the presence of H_2O_2 is shown in reactions A – C [44-46, 103]:

$$HRP(Fe^{3+}) + H_2O_2 \longrightarrow Compound(I) + H_2O \quad (A)$$

$$Compound\ (I) + C \longrightarrow Compound\ (II) + Q \quad (B)$$

$$Compound\ (II) + C \longrightarrow HRP\ (Fe^{3+}) + Q \quad (C)$$

where compounds (I) and (II) are oxidized intermediates of HRP. The kinetic formula resulting from this mechanism [35, 104-107] is:

$$v = \frac{V_{max}[H_2O_2][C]}{K_m^C[H_2O_2] + K_m^{H_2O_2}[C] + [H_2O_2][C]} \quad (1)$$

where v is the reaction rate, V_{max} is the maximum reaction rate constant ($V_{max} = k^{cat}\,[HRP]$), k^{cat} and [HRP] are turnover number and *HRP* concentration within the immunosensing layer, respectively; K_m^C and $K_m^{H_2O_2}$ are the corresponding Michaelis-Menten constants, and $[H_2O_2]$ and $[C]$ are H_2O_2 and *C* concentrations, respectively.

Molecules of *Q* produced by *HRP* can be reduced back to *C* at the surface of the working electrode in a two-electron, two proton reaction shown in reaction (D) at a rate described by the Butler-Volmer equation (Eq 2) [108]:

$$Q + 2e^- + 2H^+ \longrightarrow C \quad (D)$$

$$J = nFD_L\left[\frac{\partial Q}{\partial x}\right]_{x=0} = nFK_0[Q]_{x=0}\,e^{\left(-\frac{\alpha nF(E-E_h)}{RT}\right)} - nFK_0[C]_{x=0}\,e^{\left(\frac{(1-\alpha)nF(E-E_h)}{RT}\right)} \quad (2)$$

where J is the electric current density, n is the number of transferred electrons (n=2 for this reaction), α is the charge transfer coefficient (assumed 0.4), F is the Faraday constant (96,485 C mol^{-1}), K_0 is the apparent electron transfer rate constant for *Q*, *R* is the universal gas constant (8.314 J K^{-1} mol^{-1}), T is the absolute temperature (298 K), and E_h is the redox potential for

electrochemical reduction of Q to C under the experimental conditions used (0.15 V at pH 6.2). Values of E_h for a given set of experimental conditions were determined as the midpoint potential (E_{mid}) between the cathodic peak (for Q reduction) and anodic peak (for C oxidation) of cyclic voltammograms obtained under the same conditions [109]. The calculated value of J was taken to be the current generated by the EI.

The effect pH on E_{mid} is shown in Eq 3 [110, 111], in which m (=2) and n (=2) is the number of protons and electrons involved in the reduction of Q, respectively. This equation indicates that increasing the pH would make E_{mid} more negative and thereby reduce the working electrode's overpotential, reaction rate, and EI's signal, according to the Butler-Volmer equation. To simulate the effect of pH on E_hEq 3 was incorporated into the mechanistic model.

$$E_{mid} \sim const - 2.303\frac{mRT}{nF}\text{pH} \tag{3}$$

3.4.2 Mass Balance Equations

Assuming one-dimensional diffusion in the x-direction, the steady-state, differential, mass balance equations including diffusion and enzymatic reaction for H_2O_2, C, and Q across the immunosensing layer (0<x<L) are shown in Eqs 4-6 [103] [112-115]:

$$0 = D_L\frac{\partial^2 H_2O_2}{\partial x^2} - \frac{V_{max}[H_2O_2][C]}{K_m^C[H_2O_2] + K_m^{H_2O_2}[C] + [H_2O_2][C]} \tag{4}$$

$$0 = D_L\frac{\partial^2 C}{\partial x^2} - \frac{V_{max}[H_2O_2][C]}{K_m^C[H_2O_2] + K_m^{H_2O_2}[C] + [H_2O_2][C]} \tag{5}$$

$$0 = D_L\frac{\partial^2 Q}{\partial x^2} + \frac{V_{max}[H_2O_2][C]}{K_m^C[H_2O_2] + K_m^{H_2O_2}[C] + [H_2O_2][C]} \tag{6}$$

3.4.3 Boundary Conditions

Previous mathematical models [115-118] describing the electrochemical reduction of Q have assumed the electrochemical driving force (E-E_h) was sufficiently large that [Q] at the electrode's surface (where x=0) could be assumed to be approximately zero (Eq 7).

$$[Q]_{x=0} = 0 \tag{7}$$

However, this assumption is likely to be invalid for an EI under some realistic operating conditions. For example, to avoid electrical noise and/or interference by electroactive species in the solution, it may be desirable to use a moderate (E-E_h) value, for which $[Q]_{x=0}$ would not be vanishingly small, and the use of Eq 7 would cause significant error in the model's predictions. For that reason, we used the Butler-Volmer equation (Eq 2) as a boundary condition at the working electrode surface. This equation is valid over the entire spectrum of positive and negative (E-E_h) values.

Because Q reduction at the electrode generates C in equimolar amounts, the fluxes of Q and C at x=0 were assumed to be equal in magnitude but opposite in sign (Eq 8). Control experiments showed that J caused by the reduction of H_2O_2 was close to zero under the experimental conditions. Therefore, the flux of H_2O_2 at x=0 was assumed to be zero (Eq 9).

$$J = nFD_L[\frac{\partial Q}{\partial x}]_{x=0} = -nFD_L[\frac{\partial C}{\partial x}]_{x=0} \tag{8}$$

$$[\frac{\partial H_2O_2}{\partial x}]_{x=0} = 0 \tag{9}$$

Partitioning kinetics of all reactants between the diffusion layer and the immunosensing layer was assumed to be rapid enough that the interfacial concentrations were assumed to remain at

equilibrium. Identical partition coefficients (k_p) were assumed for all reacting species (Eqs 10-12).

$$[Q]_{x=L-} = k_p[Q]_{x=L+} \tag{10}$$

$$[H_2O_2]_{x=L-} = k_p[H_2O_2]_{x=L+} \tag{11}$$

$$[C]_{x=L-} = k_p[C]_{x=L+} \tag{12}$$

The bulk solution (at x=∞) was assumed to be well mixed and have the concentrations indicated in Eqs 13 A, B, and C.

$$[C]_{x=\infty} = C(\infty) \tag{13A}$$

$$[H_2O_2]_{x=\infty} = H_2O_2(\infty) \tag{13B}$$

$$[Q]_{x=\infty} = 0 \tag{13C}$$

No reaction is assumed to occur in the diffusion layer, so the mass transfer rate of C, H_2O_2 and Q across this layer is modeled as the product of a mass transfer coefficient (D/δ) and the concentration driving force across the layer. Also, at the interface between the diffusion layer and the immunosensing layer, the diffusive fluxes of C, H_2O_2 and Q exiting one layer is assumed to be equal to those entering the other layer (Eqs 14-16).

$$D_L[\frac{\partial Q}{\partial x}]_{x=L-} = -\frac{D_\delta}{\delta}\{[Q]_{x=L+} - 0\} \tag{14}$$

$$D_L[\frac{\partial H_2O_2}{\partial x}]_{x=L-} = \frac{D_\delta}{\delta\delta k_p}\{k_p\, H_2O_2(\infty) - [H_2O_2]_{x=L-}\} \tag{15}$$

$$D_L[\frac{\partial C}{\partial x}]_{x=L-} = \frac{D_\delta}{\delta k_p}\{k_p\, C(\infty) - [C]_{x=L-}\} \tag{16}$$

The coupled, second-order differential equations (Eqs 4-6) that described nonlinear kinetics of *HRP*-catalyzed oxidation of *C* to *Q* (Eq 1) and electrochemical reduction of *C* back to *Q* (Eq 2), along with the boundary conditions (Eqs 8-16), were solved numerically using function BVP4C in MATLAB.

3.5 Results and Discussion

3.5.1 EI system's Properties under Optimal Operating Conditions

Based on the half-factorial experiments with a centerpoint, the experimental conditions that optimized the EI signal were E = -0.2 V, $[C]$ = 8 mM, pH = 6.2, and $[H_2O_2]$ = 1 mM. The subsequent EI characterization experiments, which were conducted under these optimal experimental conditions (Figure 3.3), indicated that the EI's limit of detection was 1 ng/mL, its sensitivity was 0.63 nA mL/(ng mm^2), and its inter-assay/intra-assay variation was less than 5%.

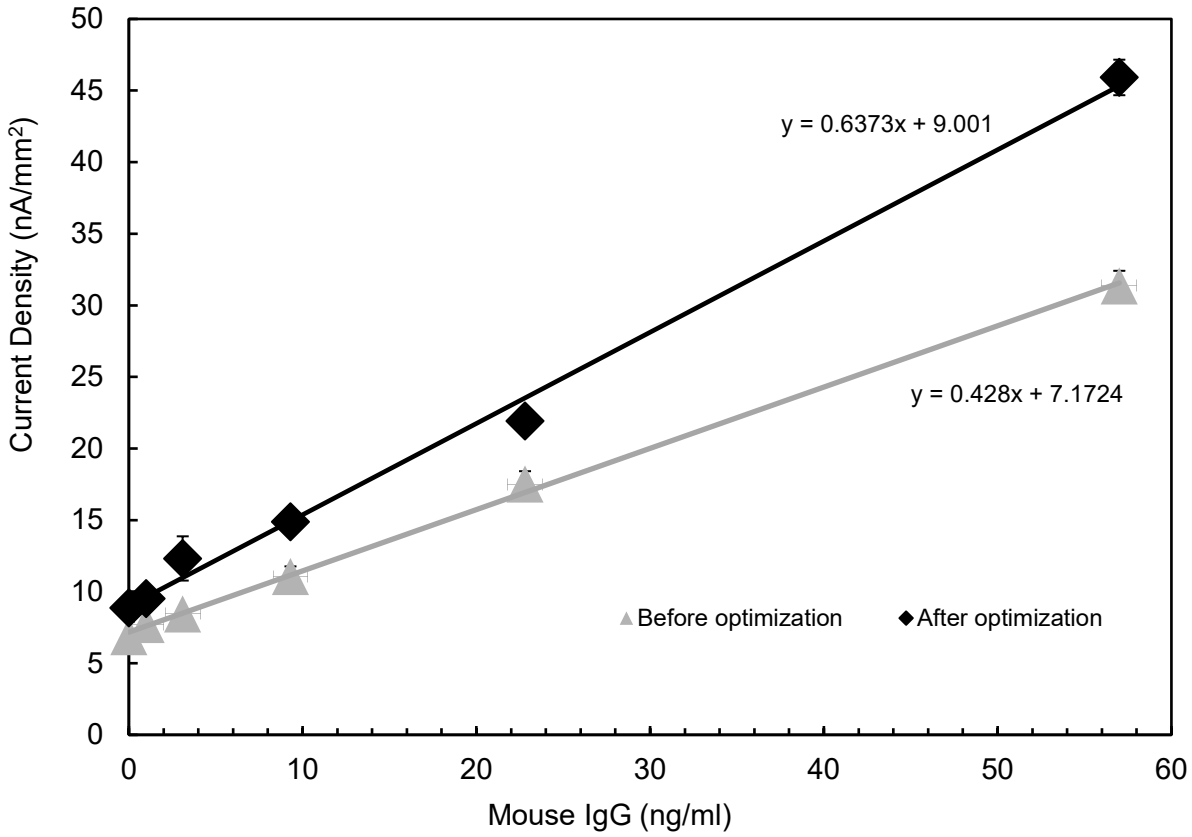

Figure 3.3. The dose response for mouse IgG on gold Dropsens SPEs. The dose response for mouse IgG on gold Dropsens SPEs before ($[H_2O_2]$=1.5 mM, pH=7 , [C] = 7 mM, E-E_h = -0.3 V) and after optimization ($[H_2O_2]$=1 mM, pH=6.2, [C] = 8 mM, E-E_h = -0.35 V). Error bars show ± standard deviation from the mean of 3 replicates.

3.5.2 Validation of Mechanistic Model

Minitab's® statistical analysis of the experimental optimization studies was integrated with the mechanistic mathematical model of EI operation for three purposes: (1) to help validate the mechanistic model, (2) to explain trends seen in the experimental data, and (3) to develop new methods to identify factors that limit an EI system's signal strength and sensitivity to the target analyte.

Some of the constants used in the mechanistic model (Table 3.2) were obtained from literature data. Others were estimated by fitting the model to the empirical, statistical model that Minitab®

generated from the experimental optimization studies. The statistical model was a best-fit polynomial that expressed the EI's signal as a function of the four factors. The polynomial had a linear term for each factor and binary, ternary, and quaternary product terms for each combination of factors to simulate interactions between factors.

Table 3.2. Values of constants used in the mechanistic model. The K_0 and [HRP] values were fit to the experimental data obtained using a constant analyte concentration of 40 ng/ml.

Parameter	Value	Units	Source
k^{cat}	2.2×10^{4}	s^{-1}	[114]
[HRP]	0.5	μM	-
K_m^C	3.0	mM	[114]
$K_m^{H_2O_2}$	0.2	mM	[114]
K_0	8.0×10^{-7}	cm s^{-1}	-
E_h	0.15	V	-
δ	3.0×10^{-3}	cm	[119]
L	25	nm	-
D_δ	2.2×10^{-5}	cm^2s^{-1}	-
D_L	2.3×10^{-6}	cm^2s^{-1}	-
k_p	1.0	-	-

Values for the kinetic constants of HRP's kinetic model were obtained from the BRENDA database [120]. The diffusion layer (δ) was for the unstirred bulk solution was assumed to remain constant [121] at a value of 200 μm [113, 122]. The thickness of the immunosensing layer was assumed to be 25 nm [119]. The values of diffusion coefficients in the immunosensing layer and diffusion layer were assumed to be 2.5×10^{-6} cm^2s^{-1} and 2.2×10^{-5} cm^2s^{-1}, respectively [123]. Values of K_0 and [HRP] (5.0×10^{-7} cm s^{-1} and 0.5 μM, respectively) were fit to the experimental data obtained using a constant analyte concentration of 40 ng/ml. Because deposition of HRP molecules in the immunosensing layer results from formation of sandwich molecular architectures, the [HRP] value is expected to vary with the analyte concentration in the bulk liquid.

To help validate the mechanistic model, trends in the model's prediction of how each of the four independent variables influenced the EI's signal were compared to the corresponding experimental data (Figures 3.5-3.8). The strength of each independent variable's effect was quantified as the Standardized Effect (SE) value [109] in the Pareto chart (Figure 3.4) generated by Minitab®. The dotted line marks the minimum SE value for statistical significance at the 95% confidence level (SE=2.09). These results indicate that all four independent variables significantly affected the signal, with the strength of those effects decreasing in the order E (SE=11.4) > [C] (SE=8.9) > pH (SE=4.6) > [H_2O_2] (SE=2.1).

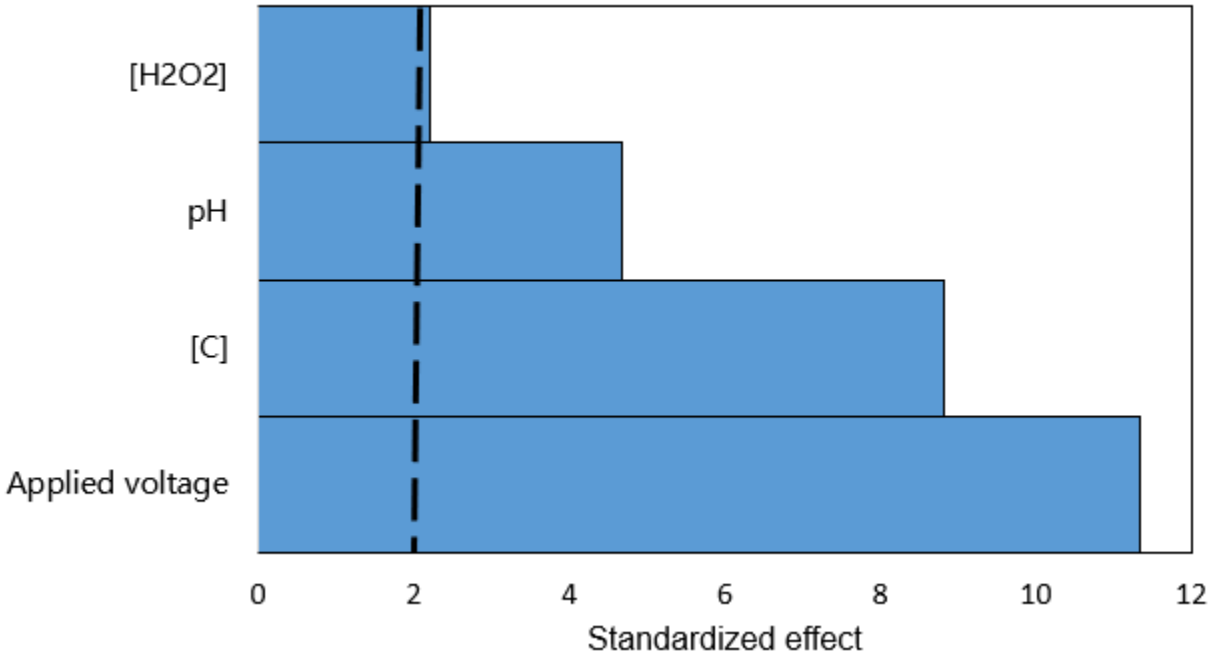

Figure 3.4. Pareto chart showing the standardized effect (SE) of factors E, [C], pH, and 〚[H〛_2 O_2] on the biosensor signal. The terms with an SE value greater than the threshold value marked with the dotted line (SE=2.09) exerted a statistically significant effect on biosensor signal at the 95% confidence level.

The strong increase in the EI's signal with E, and thus the magnitude of (E-E_h), is apparent in both the experimental results and the model's predictions (Figure 3.5). This trend is attributed to the

Butler-Volmer equation's (Eq 2) exponential dependency of the EI's amperometric signal on (E-E_h).

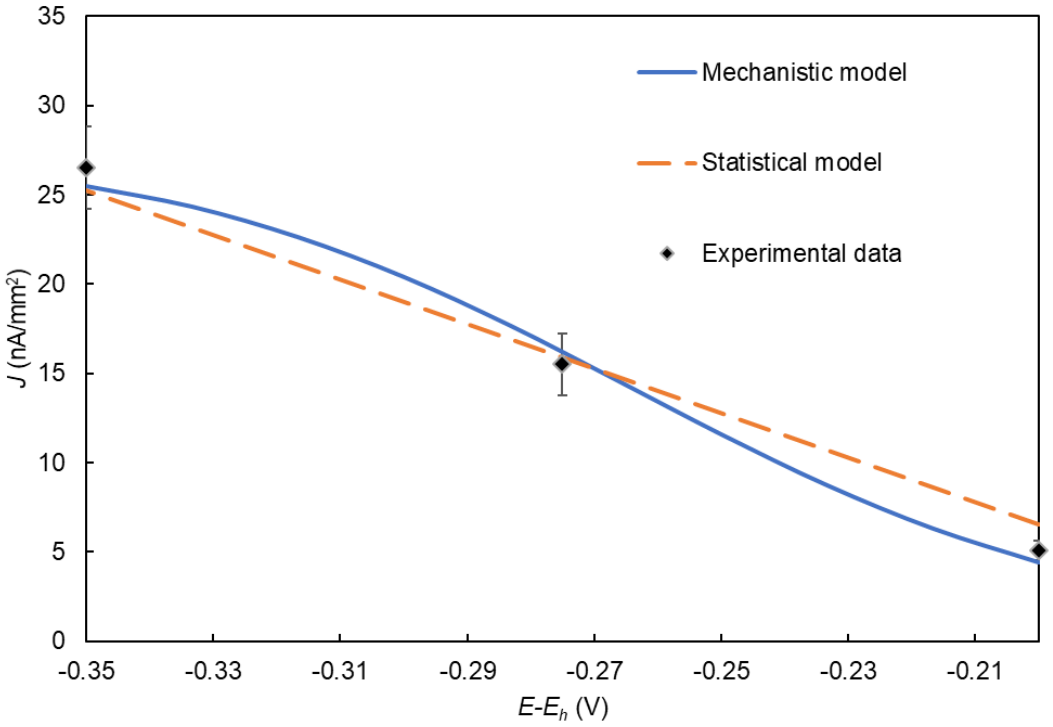

Figure 3.5. Effect of working electrode overpotential (E-Eh) on the steady-state EI's signal. [C]=8mM, [H_2 O_2] =1 mM, pH=6.2, [HRP]=0.5µM.

The effects of the two *HRP* substrate concentrations, $[C]$ and $[H_2O_2]$, predicted by the model, are also similar to those observed experimentally (Figures 3.6 and 3.7, respectively). The increase in signal with an increase in each substrate's concentration is consistent with the ping-pong kinetic model (Eq 1), which predicts that HRP's reaction rate would increase as either $[C]$ or $[H_2O_2]$ increases. However, the SE for $[C]$ is considerably stronger (SE=8.9) than that for $[H_2O_2]$ (SE=2.1), possibly because used the $[H_2O_2]$ used in the experiments was much greater than the $K_m^{H_2O_2}$ value for HRP.

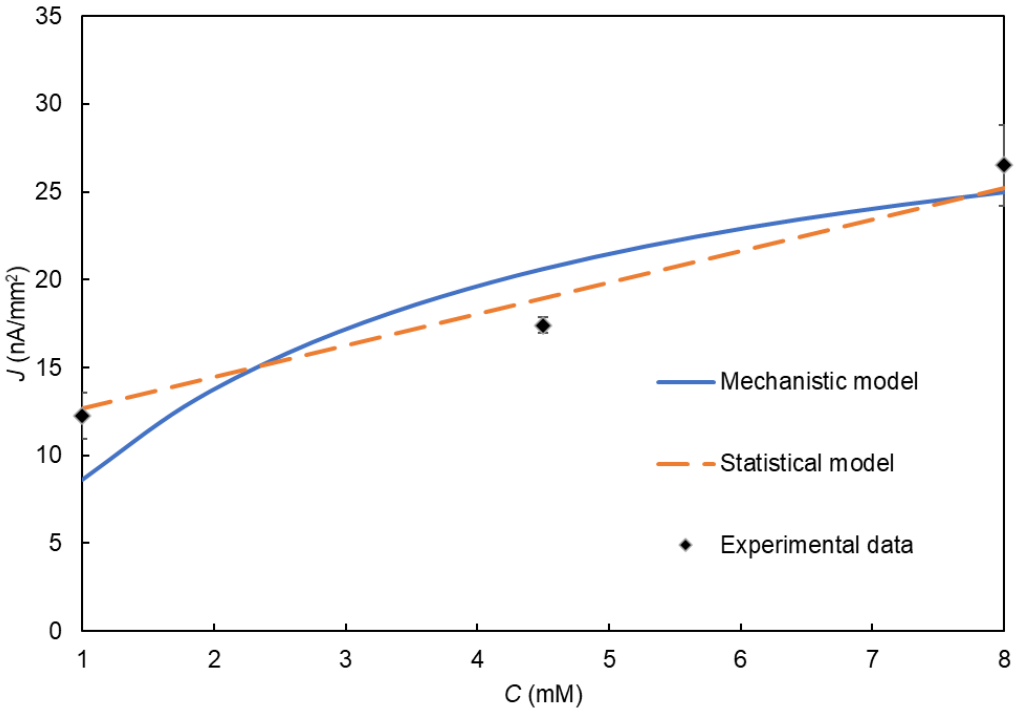

Figure 3.6. Effect of [C] on the steady-state EI's signal: comparison of model prediction and experimental data. [H_2O_2]=1 mM, pH=6.2, [HRP]=0.5µM, E-Eh = -0.35 V.

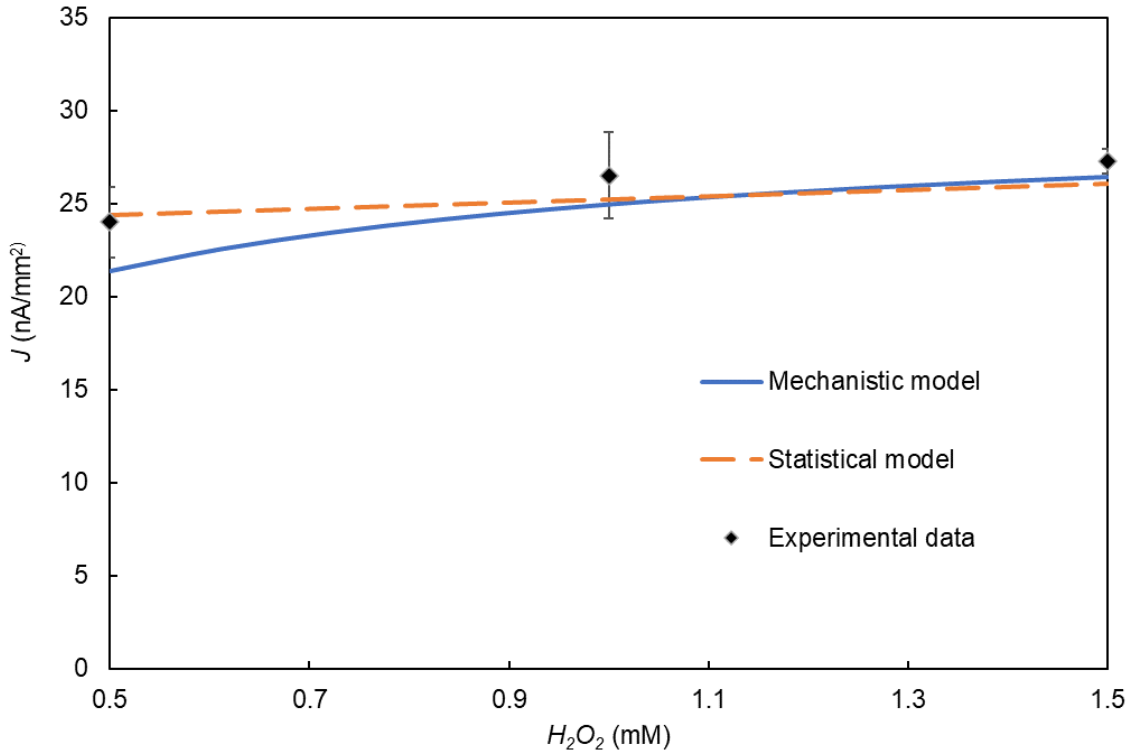

Figure 3.7. Effect of [H_2O_2] on the steady-state EI's signal: comparison of model prediction and experimental data. [C]=8mM, pH=6.2, [HRP]=0.5µM, E-Eh = -0.35V.

Both the experimental results and the mechanistic model (Figure 3.8) indicated a slightly higher EI's signal in a mildly acidic bulk solution (pH = 6.2 or 6.6) than at a neutral one (pH =7). This trend is consistent with published reports that HRP oxidized substrates more rapidly in the slightly acidic buffer than in neutral buffer [124]. One explanation for this effect is that pH (i.e., proton concentration) affects the thermodynamic driving force for the two-electron, two-proton electrochemical reduction of Q to C at the electrode. The E_h value used in the model was measured as the midpoint potential (E_{mid}) of cyclic voltammograms of an aqueous solution containing C and Q. Eq 3 shows that increasing pH would make E_{mid} more negative, which would reduce the magnitude of $(E - E_h)$ and thereby reduce the EI's signal [110, 111].

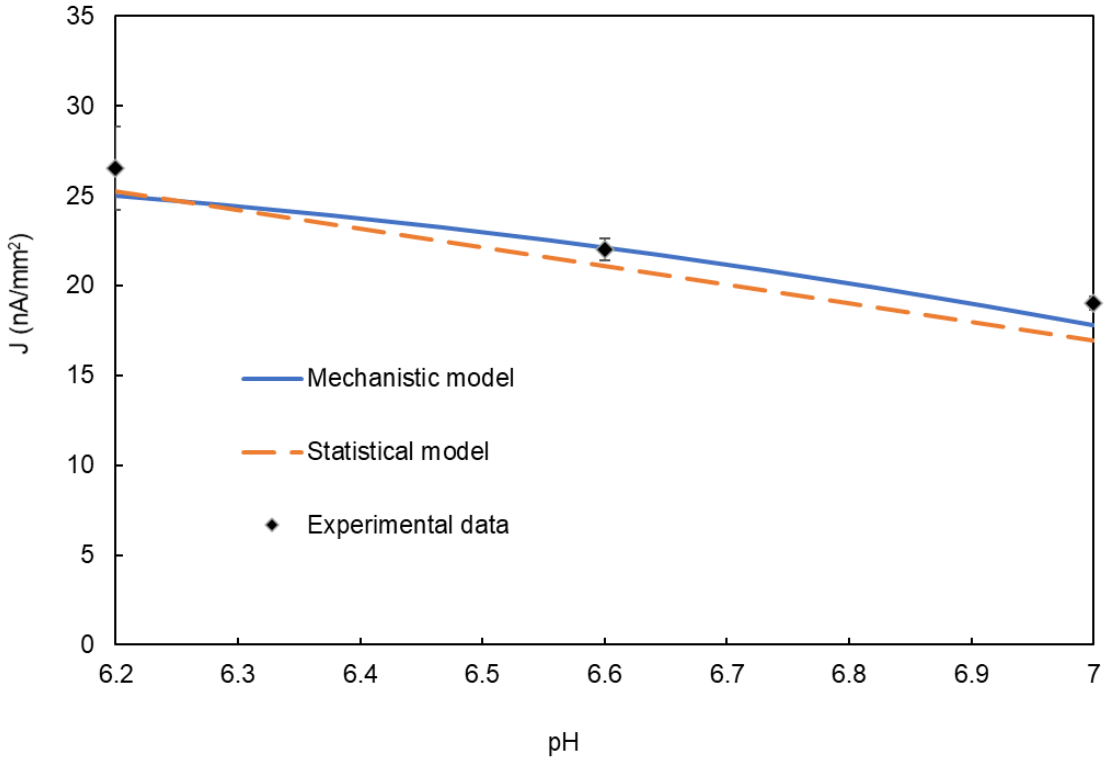

Figure 3.8. Simulation of pH effect on the steady-state EI's signal. [C] = 8mM, [H_2O_2] = 1 mM, [*HRP*] = 0.5µM, E-Eh = -0.35 V.

3.5.3 Integration of Dimensional Analysis and Flux Analysis to Determine Rate-Limiting Step

Previous mathematical models developed to describe the kinetics of HRP on the electrodes [35, 104-107] focused on the enzyme's kinetics or were based on the assumption that the *J* is mass-transfer limited. In contrast, our model explicitly calculates the rates of all key reactions and mass transfer steps, all of which could limit the signal's magnitude to some extent. Additionally, incorporation of Eqs 2 and 3 allows effects of (E-E_h) and pH, respectively, to be predicted, even under conditions in which the commonly used assumption that $[Q]_{x=0} = 0$ is invalid. Figure 3.9A shows that $[Q]_{x=0}$ decreases as the magnitude of (E-E_h) and the reduction rate of [Q] increases.

To demonstrate the improvement in accuracy this extension of the model provides, we calculated the error that would result from assuming $[Q]_{x=0}$ =0 (Figure 3.9) for an (E-E_h) range between -0.2 and -0.35V. The predicted error would have been about 15% for the (E-E_h) value of -0.3 V used by Kohli et al.[115, 125] (Figure 3.9B). The smaller the absolute value of (E-E_h), the greater the improvement in accuracy our extended model would provide.

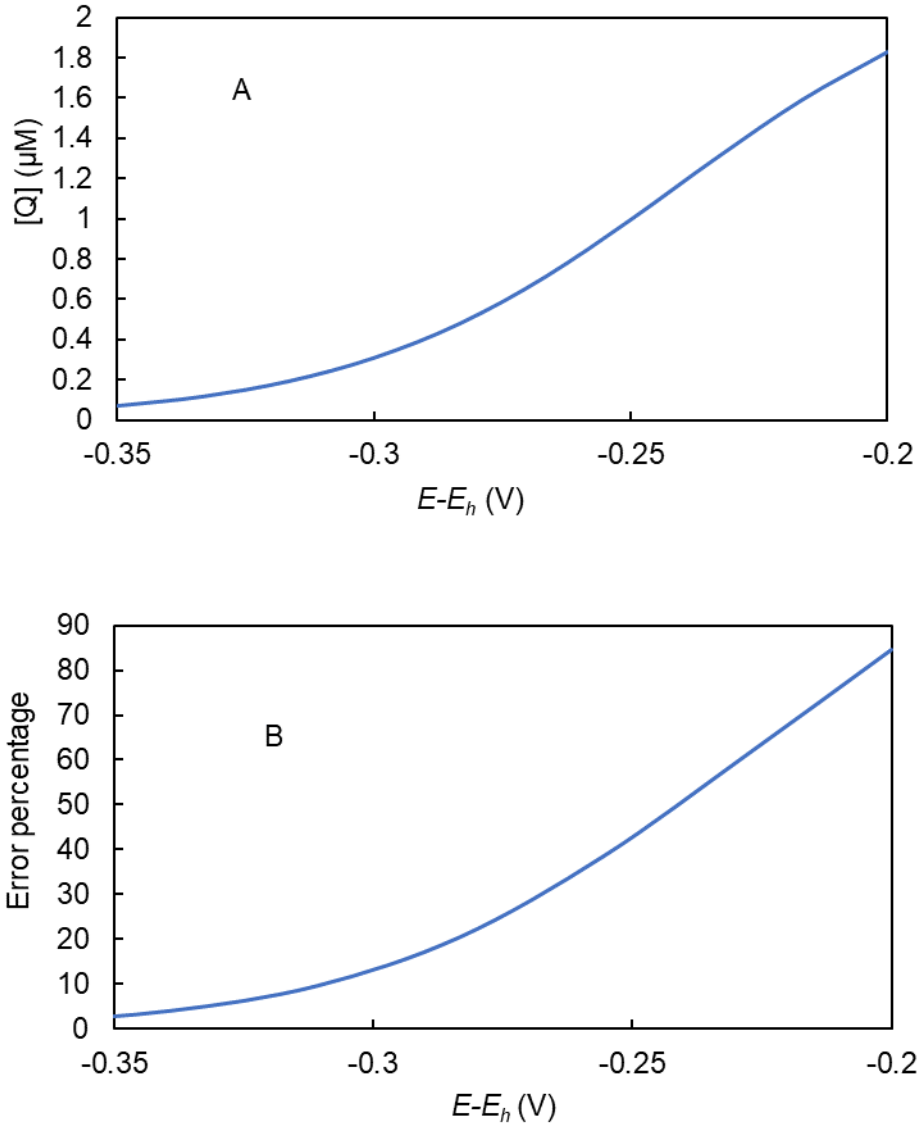

Figure 3.9. A: Simulated $[Q]_{(x=0)}$ over a range of (E-Eh) values B: Error percentage caused by assuming $[Q]_{(x=0)}$ =0 as a function of (E-Eh). Error percentage = [(J assuming $[Q]_{(x=0)}$ =0 - J using calculated value of $[Q]_{(x=0)}$) / J using calculated value of $[Q]_{x=0}$] *100. [C]=8mM, [H_2O_2] =1 mM, pH=6.2, [*HRP*]=0.5μM.

The performance properties of an EI are controlled by the dynamics of the underlying transport and reaction steps that give rise to its *J*. We developed a mathematical framework that leverages dimensional analysis and the mechanistic model's ability to predict the rates of the underlying steps to quantitatively assess the degree to which individual steps control the magnitude of the EI's

signal and its sensitivity (defined as the change in *J* per unit change in analyte concentration). Examples of the approach are described below.

The dimensionless Damkohler number (σ) shown in Eq 17 expresses the ratio of the relative rates of enzymatic reaction ($\frac{V_{max}}{K_M}$) and diffusional mass transfer ($\frac{D_L}{L^2}$) of *HRP*'s substrates within the immunosensing layer [126]. Plugging constants from Table 3.2 into Eq 17 revealed that σ for *C* and H_2O_2 were on the order of 10^{-5}, indicating that the diffusion could provide *C* and H_2O_2 to the HRP orders of magnitude faster than the HRP could consume it [127, 128]. This result indicates that the EI's signal is not significantly limited by the diffusion rate within the immunosensing layer.

$$\sigma^2 = \frac{V_{max}L^2}{D_L K_M} \tag{17}$$

Flux-control analysis has been used to determine the extent to which the rates of individual enzymatic reactions in a biochemical reaction pathway limit the overall mass flux through that pathway [129]. We used a similar approach to determine the relative degrees to which the enzymatic and electrochemical reaction steps limit the magnitude of EI's signal. We defined a current-control coefficient (C_{Vi}^{J}) for each reaction step (V_i) as the ratio of the percent change in the EI's signal to the percent change in V_i while holding all other independent variables constant (Eq 18). We used the mechanistic model to calculate an incremental change in *J* (ΔJ) resulting from an incremental

change (ΔV_i) in either the enzymatic reaction rate (simulated by changing the [HRP] value) or the electrochemical reaction rate (simulated by changing the (E-E_h) value). The incremental changes

(ΔJ and ΔV_i) were then used in place of the differentials (dJ and dV_i) in Eq 18 to calculate the C_{Vi}^{J} values for both the enzymatic reaction and the electrochemical reaction across the range of (E-E_h) values used in this study.

$$\frac{dJ}{J} \Big/ \frac{dV_i}{V_i} = dV_i \tag{18}$$

The C_{Vi}^{J} values calculated by making incremental changes in [HRP] remained virtually 1.0 across the entire range of (E-E_h), for the [HRP] value listed in Table 3.2 (0.5μm), as well as values ranging from 0.005 μM to 50 μM (results not shown). This result indicates that the EI's signal is strongly limited by [HRP] over the entire range simulated. Consequently, the EI's signal has the potential to be linearly correlated with the target analyte's concentration, depending on the shape of the adsorption isotherm of the immobilized primary antibody for its target analyte.

In contrast, the C_{Vi}^{J} values for the electrochemical reaction varied significantly across the range of overpotential used in this study (Figure 3.10) and exhibited a peak at about 3.3 at an (E-E_h) value of about -0.26V. Although the predicted EI's signal curve increased monotonically as the magnitude of (E-E_h) increased, the curve exhibited an inflection point at about the same (E-E_h) value the C_{Vi}^{J} curve peaked. This observation suggests that a transition occurs at this point. For lower (E-E_h) magnitudes, increasing the magnitude strongly increases the EI's signal; however, for higher (E-E_h) magnitudes, further increases in the (E-E_h) magnitude offer diminishing returns, suggesting that the peak in C_{Vi}^{S} may mark an optimal operating overpotential in the absence of other overriding considerations, such as the presence of electrochemical interferents. For significantly higher (E- E_h) magnitudes, the J asymptotically approaches a maximum value and the C_{Vi}^{J} value approaches 0.

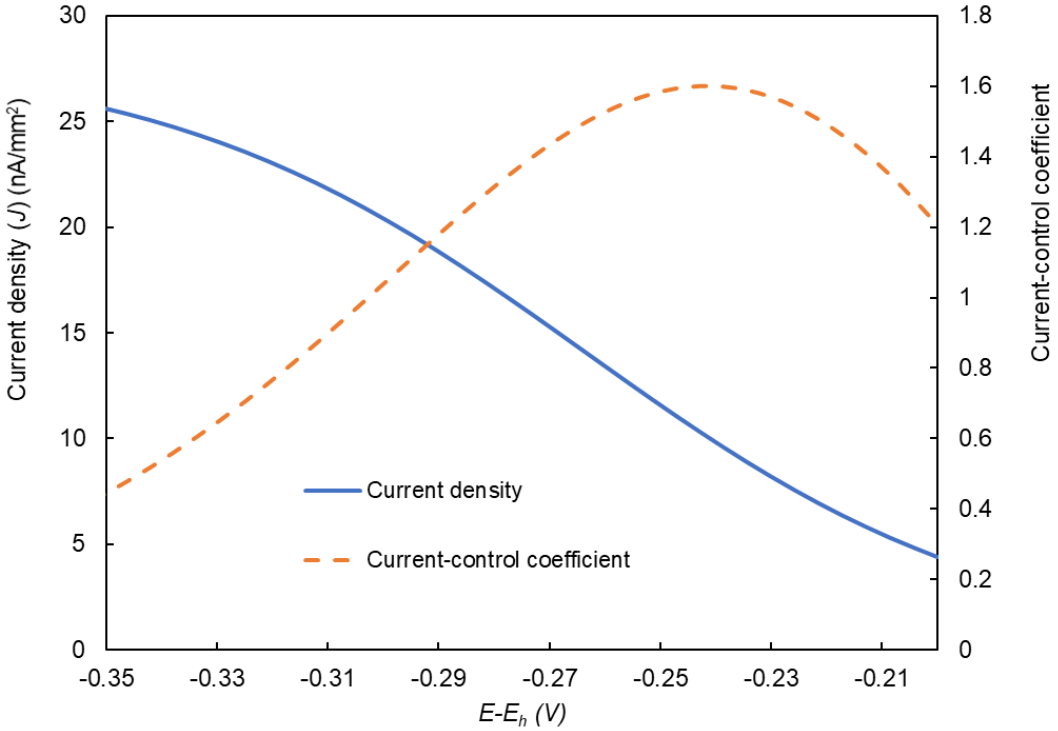

Figure 3.10. Predicted current density (J) and current-control coefficients for the electrochemical reaction at different E values. [C]=8mM, [H_2O_2] =1 mM, pH=6.2, [HRP]=0.5µM.

Because [HRP] would be expected to increase with the analyte concentration, the mechanistic model was also used to calculate the EI's sensitivity (*S*) to [HRP] (defined in Eq 19) as well as sensitivity-control coefficients (C_{Vi}^{S}) (defined in Eq 20).

$$S \simeq \frac{dJ}{d[\mathrm{HRP}]} \tag{19}$$

$$\frac{\frac{dS}{S}}{\frac{dV_i}{V_i}} = C_{Vi}^{S} \tag{20}$$

The *S* and C_{Vi}^{S} values were calculated in a manner similar to that used to calculate C_{Vi}^{J} values. The model was used to calculate incremental ΔJ values resulting from incremental Δ[HRP] values. The incremental change values were substituted for differentials in Eqs 19 and 20. The resulting *S*

values and C_{Vi}^{S} values (Figure 3.11) have shapes similar to the J and C_{Vi}^{J} curves, respectively, shown in Figure 3.10. However, the peak in the C_{Vi}^{S} curve occurs at a slightly different (E-E_h) value (-0.23V) than the peak in the C_{Vi}^{J} curve (-0.26V). If an EI were operated near the peak of the C_{Vi}^{S} curve, the sensitivity could be adjusted simply by making a relatively small change in the (E-E_h) value. Higher sensitivities would be desirable for accurately measuring analyte concentrations over a relatively small concentration range, whereas lower sensitivities would be desirable for measuring analyte concentrations over a wide range.

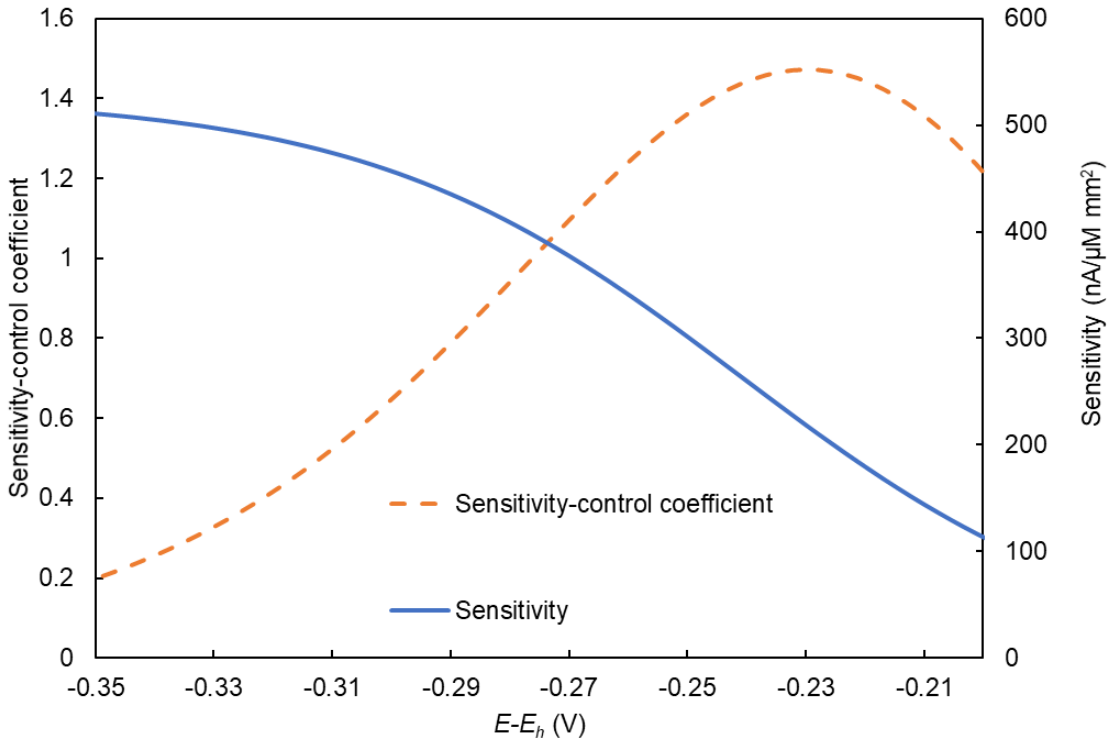

Figure 3.11. Sensitivity-control coefficient and sensitivity vs. E-E_h. [C]=8mM, [H_2O_2] =1.0mM, pH=6.2, [*HRP*]=0.5μM.

3.6 Conclusions

This study demonstrated the use of a novel, integrated experimental and modeling framework to analyze and optimize the performance of EIs. The experimental component included (1) deposition

of an EI interface on the working electrode of miniature SPE arrays; (2) measurement of the performance properties of the resulting EIs for measuring the concentration of a surrogate protein antigen (mouse IgG); (3) use of a response-surface, statistical-design-of-experiments approach to optimize four independent variables: electrode overpotential, pH, and the concentrations of HRP's two substrates ([C] and [H_2O_2]); and (4) development of a statistical model of the experimental data that empirically describes the effect of the four independent variables on the EI's signal.

The modeling component included (1) development of a detailed, mechanistic model of the EI interface that described the rates of the mass-transfer and reaction steps that gave rise to the EI's signal; (2) use of the statistical model of the experimental data to help validate the mechanistic model; and (3) integration of dimensional analysis, principles of flux-control analysis, and the mechanistic model's predictive capabilities to obtain unprecedented insight into which steps control the magnitude of the EI's signal and its sensitivity to the target analyte.

The EI developed in this study had a limit of detection of 1 ng/mL and an inter-assay/intra-assay variation of less than 5%. The mechanistic model reproduced experimentally observed effects of the four independent variables on the EI's signal. Calculation of Damkohler numbers indicated that diffusion of HRP's substrates in the biocatalytic layer did not limit the EI's performance at the overpotential of -0.3 V. Calculation of current-control and sensitivity-control coefficients analyses provided new insight into to which the enzymatic and electrochemical reactions limited both the EI's signal and its sensitivity over the experimentally relevant range of (E-E_h) values.

The novel, integrated experimental and modeling framework presented in this study provides unprecedented capabilities to design, optimize, and validate EIs for diverse applications. Its ability to quickly identify key mass transfer or reaction step(s) that limit(s) could guide strategies to overcome such limitation(s) and thereby reduce the time required to develop new commercial EI

systems. Also, the predictive power of the mechanistic model could, in principle, enable EIs to be designed *a priori* to meet specifications and enable rapid, *in-silic*o hypothesis testing that could accelerate FDA approval of EI systems for healthcare applications.

APPENDIX

MATLAB Codes

```
%%%% This function returns the effect of overpotential on EI's signal%%%%
function overpotential
H=1e-6; %H2O2 bulk concentration in mol/cm3
C=8e-6; %Catechol bulk concentration in mol/cm3
KHm=2e-7; %Km value of HRP for H2O2 in mol/cm3
KCm=3e-6; %Km value of HRP for catechol in mol/cm3
Kcat=22000; %turnover number of HRP for catechol and H2O2 in 1/sec
E=5e-10; %concentration of HRP in mol/cm3
L= 2.2e-6; %thickness of enzyme layer in cm
Df= 2.28e-6; %cm2/s %diffusion coefficient in enzyme layer
De= 2.2e-5; %cm2/s %diffusion coefficient in boundary layer
Kp= 1; %partition coefficient
del = 3e-3; %thickness of boundary layer in cm
Ka=0.1e-6; %apparent electron transfer rate in cm/s
R=8.314; %universal gas constant (8.314 J K-1 mol-1
T=298; %temperature in K
area= 0.118; %area of the working electrode in cm2
electron= 2; %number of electron transferred in reduction of quinone
F= 96485 %Faraday constant 96,485 C mol-1
x = linspace(0,L,100);
function dydx = ode3(x,y) %this function returns all of the odes, concentrations have been normalized by catechol
bulk concentration
dy1dx = [ y(2); (Kcat*E*y(1)*y(3)/(Df*(((KHm*KCm)/C)+KCm*y(3)+KHm*y(1)+(y(1)*y(3)*C))))];
dy2dx = [ y(4); (Kcat*E*y(1)*y(3)/(Df*(((KHm*KCm)/C)+KCm*y(3)+KHm*y(1)+(y(1)*y(3)*C))))];
dy3dx = [ y(6); -(Kcat*E*y(1)*y(3)/(Df*(((KHm*KCm)/C)+KCm*y(3)+KHm*y(1)+(y(1)*y(3)*C))))];
dydx=[dy1dx;dy2dx;dy3dx];
end

function res = ode3bc(ya,yb) %this function returns the BCs
res1 = [ya(4); Df*yb(2)-((De/(Kp*del))*(Kp-yb(1)))];%
res2 = [ya(2)+ya(6); Df*yb(4)-((De/(Kp*del))*(Kp*H/C-yb(3)))];%
res3 = [ya(6)-((((ya(5)*Ka*Exp)-(ya(3)*Ka*EXP))/(area*Df))); Df*yb(6)+((De/(Kp*del))*yb(5))];
res=[res1;res2;res3];
```

```
end
S=linspace(-0.05,-0.25,10);%E(applied voltage range)
i=1;
for i=1:length(S)
  V=S(i);
  Exp=exp((-F*0.8*((V-0.15)))/(R*T));%corresponds to butler-volmer
  EXP=exp((F*1.2*((V-0.15)))/(R*T));%corresponds to butler-volmer
  eexp(i)=Exp;
initialsolution = bvpinit(x,[1,0.001,1,-0.5,0.01,-0.06]);%initial guess
solution = bvp4c(@ode3,@ode3bc,initialsolution);
y = deval(solution,x);
D(i)= y(6,1);
J(i)=2*96485*Df*D(i)*C*(10000000); %current density in nA/mm2
end
figure (1)
hold on
plot(S,J);
xlabel('Potential(V)');
ylabel('Current density(nA/mm2)');
end
%%%%%%%%%%%%%%%%%%%%%%%%%%%%%%%%%%%%%%%%
```

```
%%%% This function returns the effect of pH on EI's signal%%%%
function hydrogenperoxide
H=1e-6; %H2O2 bulk concentration in mol/cm3
C=8e-6; %Catechol bulk concentration in mol/cm3
KHm=2e-7; %Km value of HRP for H2O2 in mol/cm3
KCm=3e-6; %Km value of HRP for catechol in mol/cm3
Kcat=22000; %turnover number of HRP for catechol and H2O2 in 1/sec
E=5e-10; %concentration of HRP in mol/cm3
L= 2.2e-6; %thickness of enzyme layer in cm
Df= 2.28e-6; %cm2/s %diffusion coefficient in enzyme layer
De= 2.2e-5; %cm2/s %diffusion coefficient in boundary layer
Kp= 1; %partition coefficient
del = 3e-3; %thickness of boundary layer in cm
Ka=0.1e-6; %apparent electron transfer rate in cm/s
R=8.314; %universal gas constant (8.314 J K-1 mol-1
T=298; %temperature in K
area= 0.118; %area of the working electrode in cm2
electron= 2; %number of electron transferred in reduction of quinone
F= 96485 %Faraday constant 96,485 C mol-1
V=-0.2; %applied voltage
   Exp=exp((-F*0.8*((V-0.15)))/(R*T));%corresponds to butler-volmer
   EXP=exp((F*1.2*((V-0.15)))/(R*T));%corresponds to butler-volmer
x = linspace(0,L,100);
function dydx = ode3(x,y) %this function returns all of the odes, concentrations have been normalized by catechol
bulk concentration
dy1dx = [ y(2); (Kcat*E*y(1)*y(3)/(Df*(((KHm*KCm)/C)+KCm*y(3)+KHm*y(1)+(y(1)*y(3)*C))))];
dy2dx = [ y(4); (Kcat*E*y(1)*y(3)/(Df*(((KHm*KCm)/C)+KCm*y(3)+KHm*y(1)+(y(1)*y(3)*C))))];
dy3dx = [ y(6); -(Kcat*E*y(1)*y(3)/(Df*(((KHm*KCm)/C)+KCm*y(3)+KHm*y(1)+(y(1)*y(3)*C))))];
dydx=[dy1dx;dy2dx;dy3dx];
end

function res = ode3bc(ya,yb) %this function returns BCs
res1 = [ya(4); Df*yb(2)-((De/(Kp*del))*(Kp-yb(1)))];%
res2 = [ya(2)+ya(6); Df*yb(4)-((De/(Kp*del))*(Kp*H/C-yb(3)))];%
res3 = [ya(6)-((((ya(5)*Ka*Exp)-(ya(3)*Ka*EXP))/(area*Df))); Df*yb(6)+((De/(Kp*del))*yb(5))];
```

```
res=[res1;res2;res3];
end
S=linspace(0.5e-6,1.5e-6,10); %H2O2 range
i=1;
for i=1:length(S)
H=S(i);
initialsolution = bvpinit(x,[1,0.001,1,0.05,0.001,0.06]);
solution = bvp4c(@ode3,@ode3bc,initialsolution);
y = deval(solution,x);
D(i)= y(6,1);
J(i)=2*96485*Df*D(i)*C*(10000000); %current density
end
figure (1)
hold on
plot(S,J);
xlabel('H2O2(mM)');
ylabel('Currentdensity(nA/mm2)');
end
%%%%%%%%%%%%%%%%%%%%%%%%%%%%%%%%%%%%%%%%%%%%%
```

```
%%%% This function returns the effect of catechol concentration on the EI's signal%%%%
function catechol
H=1e-6; %H2O2 bulk concentration in mol/cm3
C=8e-6; %Catechol bulk concentration in mol/cm3
KHm=2e-7; %Km value of HRP for H2O2 in mol/cm3
KCm=3e-6; %Km value of HRP for catechol in mol/cm3
Kcat=22000; %turnover number of HRP for catechol and H2O2 in 1/sec
E=5e-10; %concentration of HRP in mol/cm3
L= 2.2e-6; %thickness of enzyme layer in cm
Df= 2.28e-6; %cm2/s %diffusion coefficient in enzyme layer
De= 2.2e-5; %cm2/s %diffusion coefficient in boundary layer
Kp= 1; %partition coefficient
del = 3e-3; %thickness of boundary layer in cm
Ka=0.1e-6; % apparent electron transfer rate in cm/s
R=8.314; %universal gas constant (8.314 J K-1 mol-1
T=298; %temperature in K
area= 0.118; %area of the working electrode in cm2
electron= 2; %number of electron transferred in reduction of quinone
F= 96485 %Faraday constant 96,485 C mol-1
V=-0.2; %applied voltage
   Exp=exp((-F*0.8*((V-0.15)))/(R*T));%corresponds to butler-volmer
   EXP=exp((F*1.2*((V-0.15)))/(R*T));%corresponds to butler-volmer
x = linspace(0,L,100);
function dydx = ode3(x,y) %this function returns all of the odes, concentrations have been normalized by catechol
bulk concentration
dy1dx = [ y(2); (Kcat*E*y(1)*y(3)/(Df*(((KHm*KCm)/C)+KCm*y(3)+KHm*y(1)+(y(1)*y(3)*C))))];
dy2dx = [ y(4); (Kcat*E*y(1)*y(3)/(Df*(((KHm*KCm)/C)+KCm*y(3)+KHm*y(1)+(y(1)*y(3)*C))))];
dy3dx = [ y(6); -(Kcat*E*y(1)*y(3)/(Df*(((KHm*KCm)/C)+KCm*y(3)+KHm*y(1)+(y(1)*y(3)*C))))];
dydx=[dy1dx;dy2dx;dy3dx];
end

function res = ode3bc(ya,yb)%this function returns all of the BCs
res1 = [ya(4); Df*yb(2)-((De/(Kp*del))*(Kp-yb(1)))];%
res2 = [ya(2)+ya(6); Df*yb(4)-((De/(Kp*del))*(Kp*H/C-yb(3)))];%
res3 = [ya(6)-((((ya(5)*Ka*Exp)-(ya(3)*Ka*EXP))/(area*Df))); Df*yb(6)+((De/(Kp*del))*yb(5))];
```

```
res=[res1;res2;res3];
end
S=linspace(1e-6,8e-6,10); %range of catechol
i=1;
for i=1:length(S)
C=S(i);
initialsolution = bvpinit(x,[1,0.001,1,0.05,0.001,0.06]);
solution = bvp4c(@ode3,@ode3bc,initialsolution);
y = deval(solution,x);
D(i)= y(6,1);
J(i)=2*96485*Df*D(i)*C*(10000000); %Current density in nA/mm2
end
hold on
plot(S*1e6,J);
xlabel('Catechol(mM)');
ylabel('Current density(nA/mm2)');
end
%%%%%%%%%%%%%%%%%%%%%%%%%%%%%%%%%%%%%%%%%
```

```
%%%% This function returns the effect of pH on EI's signal%%%%
function hydrogenperoxide
H=1e-6; %H2O2 bulk concentration in mol/cm3
C=8e-6; %Catechol bulk concentration in mol/cm3
KHm=2e-7; %Km value of HRP for H2O2 in mol/cm3
KCm=3e-6; %Km value of HRP for catechol in mol/cm3
Kcat=22000; %turnover number of HRP for catechol and H2O2 in 1/sec
E=5e-10; %concentration of HRP in mol/cm3
L= 2.2e-6; %thickness of enzyme layer in cm
Df= 2.28e-6; %cm2/s %diffusion coefficient in enzyme layer
De= 2.2e-5; %cm2/s %diffusion coefficient in boundary layer
Kp= 1; %partition coefficient
del = 3e-3; %thickness of boundary layer in cm
Ka=0.1e-6; %apperant electron transfer rate in cm/s
R=8.314; %universal gas constant (8.314 J K-1 mol-1
T=298; %temperature in K
area= 0.118; %area of the working electrode in cm2
electron= 2; %number of electron transferred in reduction of quinone
F= 96485 %Faraday constant 96,485 C mol-1
V=-0.2; %applied voltage
   Exp=exp((-F*0.8*((V-0.15)))/(R*T));%corresponds to butler-volmer
   EXP=exp((F*1.2*((V-0.15)))/(R*T));%corresponds to butler-volmer
x = linspace(0,L,100);
function dydx = ode3(x,y) %this function returns all of the odes, concentrations have been normalized by catechol
bulk concentration
dy1dx = [ y(2); (Kcat*E*y(1)*y(3)/(Df*(((KHm*KCm)/C)+KCm*y(3)+KHm*y(1)+(y(1)*y(3)*C))))];
dy2dx = [ y(4); (Kcat*E*y(1)*y(3)/(Df*(((KHm*KCm)/C)+KCm*y(3)+KHm*y(1)+(y(1)*y(3)*C))))];
dy3dx = [ y(6); -(Kcat*E*y(1)*y(3)/(Df*(((KHm*KCm)/C)+KCm*y(3)+KHm*y(1)+(y(1)*y(3)*C))))];
dydx=[dy1dx;dy2dx;dy3dx];
end

function res = ode3bc(ya,yb) %this function returns BCs
res1 = [ya(4); Df*yb(2)-((De/(Kp*del))*(Kp-yb(1)))];%
res2 = [ya(2)+ya(6); Df*yb(4)-((De/(Kp*del))*(Kp*H/C-yb(3)))];%
res3 = [ya(6)-((((ya(5)*Ka*Exp)-(ya(3)*Ka*EXP))/(area*Df))); Df*yb(6)+((De/(Kp*del))*yb(5))];
```

```
res=[res1;res2;res3];
end
S=linspace(0.5e-6,1.5e-6,10); %H2O2 range
i=1;
for i=1:length(S)
H=S(i);
initialsolution = bvpinit(x,[1,0.001,1,0.05,0.001,0.06]);
solution = bvp4c(@ode3,@ode3bc,initialsolution);
y = deval(solution,x);
D(i)= y(6,1);
J(i)=2*96485*Df*D(i)*C*(10000000); %current density
end
figure (1)
hold on
plot(S*1e6,J);
xlabel('H2O2(mM)');
ylabel('Current density(nA/mm2)');
end
%%%%%%%%%%%%%%%%%%%%%%%%%%%%%%%%%%%%%%%%%%%%%%%
```

4 Theoretical and Experimental Studies of an Inhibition-based Bi-enzyme Electrochemical Biosensor (IBE) for Detection of Organophosphorus Compounds

4.1 Introduction

Amperometric biosensors detect chemicals at a constant electrochemical potential by measuring oxidation or reduction current produced by electroactive products of a biochemical reaction [130]. Low cost, high sensitivity, relatively fast response time, simplicity of design, being compact, and having the potential for being miniaturized make an amperometric biosensor a great choice for detecting a wide range of chemicals [118, 131].

Amperometric biosensors based on the principle of enzyme inhibition have been extensively developed for environmental applications [132]. These biosensors can be developed for analytes that can act as inhibitors for a specific enzyme. Such analytes can interact with an enzyme or enzyme-substrate complex and inhibit the biocatalytic properties. Therefore, they can be detected and measured indirectly by measuring the change that they cause in the biocatalytic activity of an immobilized enzyme. The susceptibility of most enzymes to a very low concentration of inhibitors makes these types of biosensors very sensitive [133].

Inhibition-based amperometric biosensors have been frequently developed for the detection of Organophosphorus compounds (OPs) [56, 134, 135]. OPs are synthetic compounds that are widely used in pesticides and chemical warfare [136]. OPs work based on inhibition of acetylcholinesterase (AChE) in the central nervous system of insects and humans. OPs can reside in the environment for several years and pose serious health issue for the non-target species such

as human and animals. Inhibition of AChE by OPs in non-target species can cause severe health issues and even death [137].

The gold standard method for detecting OPs is gas/liquid chromatography combined with mass spectroscopy [138]. Chromatographic methods are very sensitive, specific, and reliable, but they suffer from some major drawbacks. Some of these disadvantages are high cost, complicated and time-consuming process for sample preparation, requiring highly trained technicians, and not being applicable for on-site or in-field applications [138]. In contrast, amperometric biosensors based on the principle of enzyme inhibition provide a fast and sensitive detection without sample preparation. Besides, they have the potential for being developed as miniaturized and portable analytical devices for on-site applications [139]. AChE is the most commonly used enzyme in the fabrication of biosensors based on principles of enzyme inhibition for OPs [140, 141].

Despite a large amount of interest in the area of inhibition based amperometric biosensors for detection of OPs, there is a lack of a comprehensive theoretical study in this field. Zhang et al. developed a theoretical model for immobilized enzyme inhibition biosensors under the assumption that the inhibition process is diffusion limited. This model was valid for the concentrations of the OPs, which were very low compared to the amount of enzyme available [142]. Choi et al. developed a mathematical model for a fiber-optic biosensor for the detection of OPs. In their study, a mathematical model of enzyme kinetics for the inhibition of AChE and transport phenomena was developed to analyze the effect of operating parameters. Using the mathematical model, they optimized AChE concentration and substrate concentration [143].Their model was able to simulate the optical signal under different experimental conditions.

Herein, we present a comprehensive mathematical model to simulate and study the time-dependent electric current in an inhibition-based bi-enzyme electrochemical biosensor (IBE). The IBE is a

modified version of our previously developed biosensor. Previously, a novel bi-enzyme electrochemical biosensor was developed in Dr. Worden's research group to measure the activity of an esterase enzyme, neuropathy target esterase (NTE) [61]. The biosensor included an esterase enzyme (NTE) and an oxidase enzyme (tyrosinase) to generate a substrate recycling system that could amplify the biosensor's signal. The biosensor was fabricated in a conventional electrochemical cell format. A mathematical model was also developed to study the steady-state electric signal in the biosensor [61, 115, 144].

The IBE includes two enzymes, AChE (neurological esterase) and tyrosinase (oxidase). Phenyl methylsulfonyl fluoride (PMSF) was used as a model inhibitor of AChE. AChE hydrolyzes a reactant to yield a substrate that is repeatedly oxidized by the tyrosinase (Tyr) and then reduced by the electrode. This substrate recycling not only generates a current that reports the AChE's activity but also amplifies the electric current to increase the biosensor's sensitivity dramatically. The IBE detects PMSF by quantitative measurement of AChE's activity, and the amount of loss in AChE's activity is related to PMSF concentrations. Therefore, to achieve the maximum sensitivity, it is necessary to adjust the ratio of the two enzymes' activity in a way that AChE's activity is controlling the electric current. Besides, AChE's activity cannot exceed a specific range. It should remain low enough to allow low PMSF concentrations to have a significant effect on its activity and high enough to generate a measurable electric current. Several factors, including substrate concentration, AChE's activity, Tyr's activity, applied voltage, and diffusion rate, can influence the sensitivity of the IBE for detection of the PMSF. Therefore, we have developed an unsteady-state model to simulate the irreversible inhibition of AChE with PMSF and to study to what extend each parameter affects the biosensor's sensitivity. The model includes unsteady-state mass balance equations, including diffusion-based mass-transfer steps, enzymatic reactions, and kinetics of

irreversible enzyme inhibition. We report parameters such as current-control coefficients, sensitivity, and Damkohler numbers to quantify the effect of each factor on limiting the electric current and the biosensor's sensitivity. The model provides a platform to study the effect of each factor on controlling the electric current and the biosensor's sensitivity; therefore, allow one to optimize the governing factors affecting the biosensor's performance.

4.2 Experimental Methods

4.2.1 Materials and Instrumentation

Sodium phosphate (monobasic and dibasic), Acetylcholinesterase (C2888, from *Electrophorus electricus*), Tyrosinase (T3824, from mushroom), Bovine serum albumin (BSA), Glutaric dialdehyde (50 wt. % solution in water, Phenylmethylsulfonyl fluoride (PMSF), and Phenyl acetate were obtained from Sigma Aldrich. Ultrapure water (18.2 MΩ) was produced by a Nanopure-UV four-stage purifier (Barnstead International, Dubuque, IA); the purifier was equipped with a UV source and a final 0.2 µm filter. Ultrapure water was used to prepare all aqueous solutions. Screen-printed electrodes were obtained from Conductive Technologies Inc. and Metrohm DropSens (models DRP-250AT).

4.2.2 Enzyme Electrode Preparation

SPEs were cleaned by sonication in pure ethanol for 2 minutes, followed by rinsing with ultrapure water. To prepare the enzyme solution, 40 µl of 50 mM phosphate buffer pH 7, 20 µl of 20 mg/mL Tyr in phosphate buffer, 20 µl of 1 mg/mL AChE in phosphate buffer, 10 µl of 2.7 mg/mL BSA in phosphate buffer and 10 µl of 4 wt. % glutaraldehyde in water were mixed together just before starting the preparation procedure. Three microliters of enzyme solution (in the case of DropSens SPEs) or one microliter of enzyme solution (in the case of CTI SPEs) were deposited on the working electrode, and SPEs were left at 4 ℃ to dry overnight. Next day, prepared bi-enzyme

modified SPEs were rinsed with ultrapure water, and then they were stored at phosphate buffer at 4 ℃ for future use.

4.2.3 PMSF Detection and Electrochemical Measurements

To perform electrochemical experiments for the detection of PMSF, 30 µL of 50 mM phosphate buffer (pH 7) was added on the working electrode of SPEs. A potential of -200 mV relative to an Ag/AgCl reference electrode was maintained on the working electrode using a potentiometer (CHI 660, C.H. Instruments, USA). An aliquot of phenyl acetate solution was added, and after reaching a stable electrochemical signal, a known amount of PMSF was added, and an electrochemical current was recorded after 30 seconds.

4.3 Mathematical Model

The biosensor includes a working electrode onto which a thin layer containing AChE and Tyr is bound, a diffusion layer, and the bulk liquid. To design the mathematical model, it was assumed that the geometry of the electrode is symmetrical and mass transfer of all species takes place in one dimension (x). The model developed to describe the unsteady-state amperometric response of the IBE consisting of a set of differential mass balances for all reacting components (phenylacetate (S_1), phenol (S_2), catechol (S_3), O-quinone (S_4), and PMSF (I) over the spatial regions depicted in Figure 4.1, the enzyme-containing layer, the diffusion layer, and the bulk solution. PMSF concentration is zero throughout the biosensor interface before addition to the system ($t < T_0$).

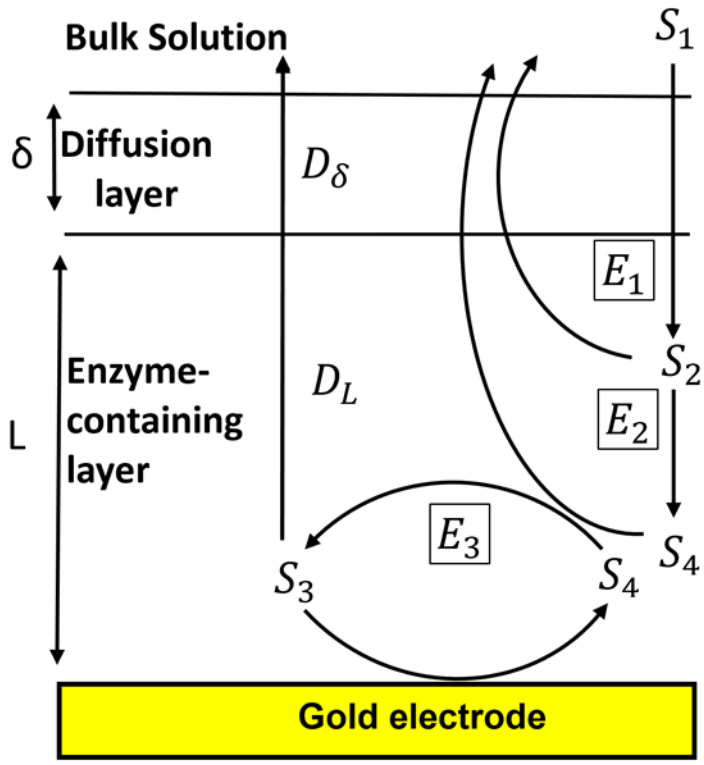

Figure 4.1. Schematic representation of reactions happening on the surface of gold working electrode. S1, S_2, S_3, and S_4 denote phenyl acetate, phenol, catechol, o-quinone respectively. E_1, E_2, and E_3 denote acetylcholinesterase, tyrosinase's phenolase activity, and tyrosinase's catecholase activity.

The mass balance equations describe diffusion of phenylacetate (S_1), phenol (S_2), catechol (S_3), *O*-quinone (S_4), and PMSF (I) in one dimension (x) through two layers (Figure 4.1) that lie between the electrode's surface at x=0 and the bulk solution: an enzyme-containing layer between x=0 and $x=L$ containing the AChE (E_1) and Tyr (E_2, E_3), and a stagnant aqueous layer between $x=L$ and $x=L+\delta$. The enzymes concentration and their maximum reactions rates were assumed to be uniform across the enzyme-containing layer, and the electrochemical reduction of O-quinone (S_4) to catechol (S_3) is assumed to occur on the electrode's surface.

The bulk solution was assumed to be well-mixed, with the concentrations of all chemical species remaining constant at their initial values [102, 115]. (Note: PMSF (*I*) bulk concentration is zero before the addition time (t=T_0)).

4.3.1 AChE Inactivation and Enzyme Kinetics

AChE is a hydrolase enzyme found in the synapse between nerve cells and muscle cells. AChE stops the signal pathway between nerve cells and muscle cells by hydrolyzing a neurotransmitter called acetylcholine[145]. In this work, phenylacetate (S_1) was used as the substrate for AChE. The AChE (E_1) hydrolyzes phenylacetate (S_1) to produce phenol (S_2) and acetate (Figure 4.2).

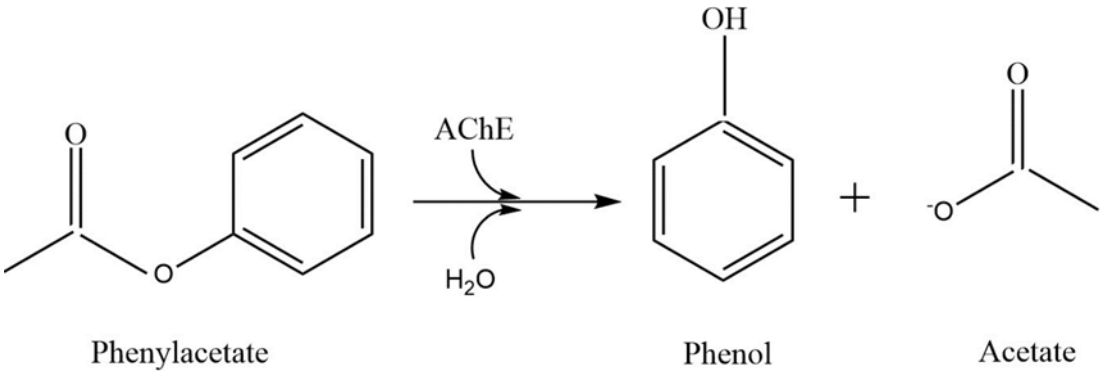

Figure 4.2. Hydrolysis of phenylacetate with AChE.

PMSF (*I*) is an irreversible inhibitor of AChE that covalently binds to the active site of the enzyme and modifies AChE's activity (E_1) [146]. The sulfonyl group of PMSF (Figure 4.3) mimics the carbonyl group of phenylacetate transition state. The hydroxyl group of serine residue of the active site of AChE nucleophilically attacks the sulfonyl group of PMSF, resulting in irreversible sulfonylation of AChE [147]. In this model, we assumed that the rate of PMSF (*I*) consumption equals the rate of AChE inactivation.

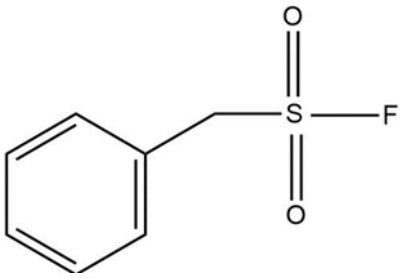

Figure 4.3. Molecular structure of PMSF.

The general scheme for the inactivation of AChE with PMSF (*I*) in the presence of the substrate (S_I) is shown in Figure 4.4.

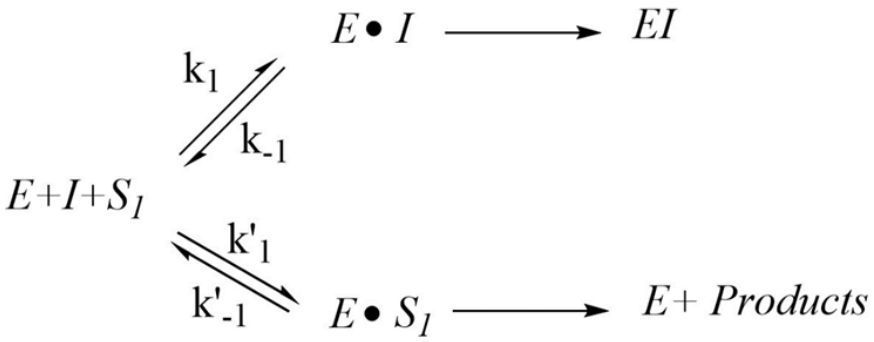

Figure 4.4. Inhibition mechanism of AChE (E) with PMSF (I) in the presence of substrate (S1).

Studies have shown that AChE inhibition with PMSF follows a pseudo-first order kinetics [147] (Eq 1):

$$ln\ \frac{V'_{max,1}}{V_{max,1}} = -k't' \tag{1}$$

Where $V_{max,1}$ and $V'_{max,1}$ are maximum velocities of the enzymatic reaction for AChE in the absence of the inhibitor and when incubated with inhibitor for a time of t'. The k' is the pseudo-first-order rate constant for the inactivation of AChE with PMSF (Eq 2):

$$k' = \frac{k_2[I]}{\frac{1}{(1-\beta)}k_I + [I]} \tag{2}$$

The affinity of PMSF for AChE is given by the Michaelis-Menten type constant, k_I. (Note: k_I has also been denoted as K_d and K_a in other studies) [110, 147].

$$k_I = \frac{k_{-1} + k_2}{k_{+1}} \tag{3}$$

k_{+1} and k_{-1} are the forward and backward rate constants for the formation of the Michaelis-Menten type complex and k_2 is the sulfonylation rate constant (Figure 4.4). The β is given by Eq 4 Where $K_{m,1}$ is the Michaelis-Menten constant for phenylacetate.

$$\beta = \frac{[S_1]}{[S_1] + K_{m,1}} \tag{4}$$

PMSF (*I*) competes with phenyl acetate (S_I) for the active site of AChE (E_I), therefore changing the Michaelis-Menten constant ($K_{m,1}$) to the apparent $K'_{m,1}$ (Eq 5) [143].

$$K'_{m,1} = K_{m,1}(1 + \frac{[I]}{k_I}) \tag{5}$$

Eqs 6-8 explain the enzymatic kinetics of AChE in the presence of the irreversible inhibition with PMSF. $k_{cat,1}$ is the turnover number of AChE for phenylacetate. By assuming that the rate of PMSF (*I*) consumption equals the rate of enzyme inactivation, Eq 9 was derived to explain the rate of PMSF (*I*) consumption.

$$v_1 = \frac{V'_{max,1}[S_1]}{K'_{m,1} + [S_1]} \tag{6}$$

$$V'_{max,1} = V_{max,1}\, Exp(-k't) \tag{7}$$

$$V_{max,1} = k_{cat,1}\, E_I \tag{8}$$

$$\frac{dI}{dt} = -E_1 k' Exp(-k't) \tag{9}$$

Tyr contains two enzyme activities: monophenolase activity, which catalyzes the hydroxylation of monophenols to produce o-diphenols (catechols), and catecholase activity, which catalyzes

oxidation of catechols to O-quinones. Figure 4.5 shows the scheme for the two-step oxidation of phenol with Tyr.

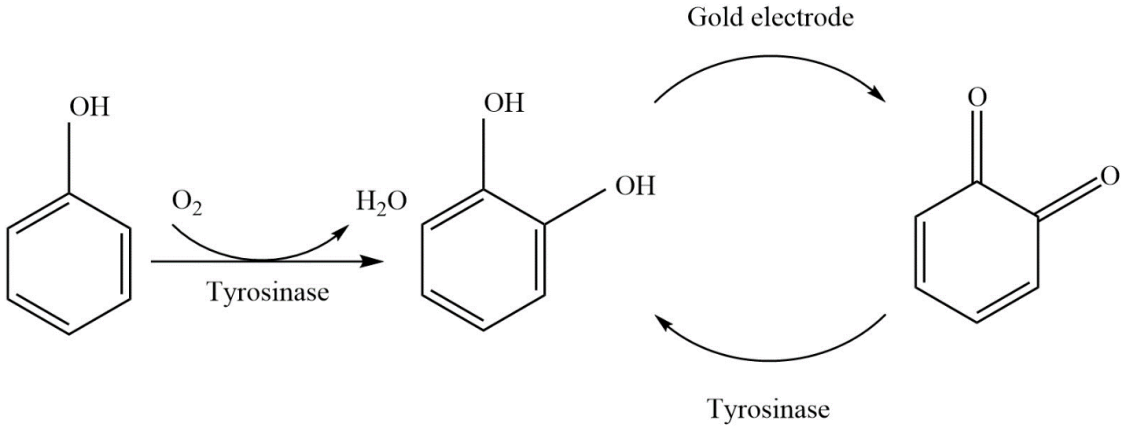

Figure 4.5. Scheme of phenol oxidation with tyrosinase to produce O-quinone.

Studies have shown that the hydroxylation step (monophenolase activity) takes place much slower than the oxidation step (catecholase activity) and therefore limits the rate of O-quinone production [148]. Therefore, we assumed that rate (v_2) of O-quinone (S_4) production from phenol (S_2) can be obtained from Eqs 11-12 where E_2 is corresponded to phenolase activity of Tyr [114]. The rate (v_3) of conversion of catechol (S_3) to O-quinone (S_4) can be given by Eqs 12-13. E_3 denotes catecholase activity of Tyr [115].

$$v_2 = \frac{V_{max,2}[S_2]}{K_{m,2} + [S_2]} \tag{10}$$

$$V_{max,2} = k_{cat,2}\, E_2 \tag{11}$$

$$v_3 = \frac{V_{max,3}[S_3]}{K_{m,3} + [S_3]} \tag{12}$$

$$V_{max,3} = k_{cat,3}\, E_3 \tag{13}$$

Molecules of O-quinone (S_4) produced by Tyr can be reduced back to catechol (S_3) at the surface of the working electrode at a rate described by the Butler-Volmer equation (Eq 14):

$$J = nFD_L \left[\frac{\partial Q}{\partial x}\right]_{x=0} = nFK_0[Q]_{x=0}\, e^{\left(-\frac{\alpha nF(E-E_h)}{RT}\right)} - nFK_0[C]_{x=0}\, e^{\left(\frac{(1-\alpha)nF(E-E_h)}{RT}\right)} \quad (14)$$

where J is the electric current density, n is the number of transferred electrons (e.g., n=2 for the electrochemical reduction of O-quinone (S_4), α is the charge transfer coefficient (assumed 0.35), F is the Faraday constant (96485 C mol^{-1}), K_0 is the apparent electron transfer rate constant for O-quinone (S_4), R is the universal gas constant (8.314 J K^{-1} mol^{-1}), T is the absolute temperature (assumed 298 K), and E_h is the redox potential for electrochemical reduction of O-quinone (S_4) to catechol (S_3) under the experimental conditions (0.15 V). Values of E_h for a given set of experimental conditions were determined as the midpoint between the cathodic peak and anodic peak of cyclic voltammogram obtained under the same conditions.

4.3.2 Mass Balance Equations

Assuming one-dimensional diffusion in the *x*-direction, the mass balance equations including diffusion and enzymatic reaction for phenyl acetate (S_1), phenol (S_2), catechol (S_3), O-quinone (S_4), and PMSF (I) across the enzyme-containing layer (0<x<L) can be derived (Eqs 15-19).

$$\frac{\partial S_1}{\partial t} = D_L \frac{\partial^2 S_1}{\partial x^2} - \frac{V'_{max,1}[S_1]}{K'_{m,1} + [S_1]} \quad (15)$$

$$\frac{\partial S_2}{\partial t} = D_L \frac{\partial^2 S_2}{\partial x^2} - \frac{V_{max,2}E_2[S_2]}{K_{m,2} + [S_2]} + \frac{V'_{max}[S_1]}{K'_{m,1} + [S_1]} \quad (16)$$

$$\frac{\partial S_3}{\partial t} = D_L \frac{\partial^2 S_3}{\partial x^2} - \frac{V_{max,3}E_3[S_3]}{K_{m,3} + [S_3]} \quad (17)$$

$$\frac{\partial S_4}{\partial t} = D_L \frac{\partial^2 S_4}{\partial x^2} + \frac{V_{max,3}[S_3]}{K_{m,3} + [S_3]} + \frac{V_{max,2}[S_2]}{K_{m,2} + [S_2]} \quad (18)$$

$$\frac{\partial I}{\partial t} = D_L \frac{\partial^2 I}{\partial x^2} - E_1 \times (-k') \times Exp(-k't) \quad (19)$$

4.3.3 Boundary Conditions

Because O-quinone (S_4) reduction at the electrode generates catechol (S_3) in equimolar amounts, their flux at x=0 were assumed to be equal in magnitude but opposite in sign (Eq 20).

$$D_L[\frac{\partial S_4}{\partial x}]_{x=0} = -D_L[\frac{\partial S_3}{\partial x}]_{x=0} \quad (20)$$

At x=0, phenylacetate (S_1), phenol (S_2), catechol (S_3), and PMSF (I) are assumed not electro-inactive chemicals (Eq 21):

$$[\frac{\partial S_1}{\partial x}]_{x=0} = 0,\ [\frac{\partial S_2}{\partial x}]_{x=0} = 0,\ [\frac{\partial S_3}{\partial x}]_{x=0} = 0,\ [\frac{\partial I}{\partial x}]_{x=0} = 0 \quad (21)$$

Partitioning kinetics of all reactants from the diffusion layer to the enzyme-containing layer was assumed to be rapid enough that the interfacial concentrations at the boundaries of the diffusion layer and enzyme-containing layer remained at equilibrium. Identical partition coefficients ($k_p = 1$) were assumed for all reactants (Eqs 22-26).

$$[S_1]_{L+} = k_p[S_1]_{L+} \quad (22)$$

$$[S_2]_{L+} = k_p[S_2]_{L+} \quad (23)$$

$$[S_3]_{L+} = k_p[S_3]_{L+} \quad (24)$$

$$[S_4]_{L+} = k_p[S_4]_{L+} \quad (25)$$

$$[I]_{L+} = k_p[S_4]_{L+} \quad (26)$$

The bulk solution (where x=∞) contained S_1 at a concentration of $S_1(\infty)$ but no S_2, S_3, and S_4. The corresponding boundary conditions are given in Eq 27 A, B, C, D, and E.

$$[S_1]_{x=\infty} = C(\infty) \tag{27A}$$

$$[S_2]_{x=\infty} = 0 \tag{27B}$$

$$[S_3]_{x=\infty} = 0 \tag{27C}$$

$$[S_4]_{x=\infty} = 0 \tag{27D}$$

$$[I]_{x=\infty,t<T0} = 0,\ [I]_{x=\infty,T0<t} = I(\infty) \tag{27E}$$

Due to the reaction in the enzyme-containing layer, S_1 diffuse from the bulk solution through the stagnant film and into the enzyme-containing layer, while S_2, S_3, and S_4 diffuse in the opposite direction. Because no reaction is assumed to occur in the diffusion layer, the flux of species entering this layer is assumed to equal that exiting it. The corresponding boundary conditions are (Eqs 28-32).

$$D_L[\frac{\partial S_1}{\partial x}]_{x=L-} = \frac{D_\delta}{k_p\,\delta}\{k_p\,S_1(\infty) - [S_1]_{x=L-}\} \tag{28}$$

$$D_L[\frac{\partial S_2}{\partial x}]_{x=L-} = -\frac{D_\delta}{\delta}\{[S_2]_{x=L+} - 0\} \ = -\frac{D_\delta}{k_p\,\delta}[S_2]_{x=L-}\} \tag{29}$$

$$D_L[\frac{\partial S_3}{\partial x}]_{x=L-} = -\frac{D_\delta}{\delta}\{[S_3]_{x=L+} - 0\} = -\frac{D_\delta}{k_p\,\delta}[S_3]_{x=L-}\} \tag{30}$$

$$D_L[\frac{\partial S_4}{\partial x}]_{x=L-} = -\frac{D_\delta}{\delta}\{[S_4]_{x=L+} - 0\} = -\frac{D_\delta}{k_p\,\delta}[S_4]_{x=L-}\} \tag{31}$$

$$D_L[\frac{\partial I}{\partial x}]_{x=L-} = \frac{D_\delta}{k_p\,\delta}\{k_p\,I(\infty) - [I]_{x=L-}\} \tag{32}$$

4.3.4 Initial Conditions

Initial conditions at injection time of phenylacetate (t=0) are (Eq 33):

$$[S_i]_{\,i=2:4,t=0,0\leqslant x\leqslant L} = 0, [S_1]_{\,t=0,0\leqslant x<L} = 0, [S_1]_{x=L} = S_1(\infty) \quad (33)$$

Inhibitor concentration (I) is zero before its injection time (T_0) and is assumed to be a constant value throughout the enzyme-containing layer and solution after injection time (Eq 34):

$$[I]_{0<t<T_0,} = 0, [I]_{T_0<t} = I(\infty) \quad (34)$$

By applying a splitting finite difference method in MATLAB, Eqs 15-19 were solved numerically using parameters and variables given in Table 4.1.

4.4 Results and Discussion

4.4.1 Biosensor's Response to PMSF

Figure 6 shows an amperometry experiment to detect PMSF. This experiment was repeated for different concentrations of PMSF to obtain a calibration curve (Figure 4.6). In all amperometry experiments, the IBE's response to PMSF was relatively fast (less than 20 seconds). It was observed that after the addition of PMSF, there was a sharp drop in current density followed by a small increase in the current density. This means that part of the drop in the current density is temporary and is not caused by PMSF inhibition. We hypothesized that this behavior could be caused by mixing while adding PMSF to the reaction solution. We tested and validated our hypothesis experimentally (Figure 4.7) and theoretically (4.9). A calibration curve for the response of the bi-enzyme biosensor to PMSF was obtained (Figure 4.8).

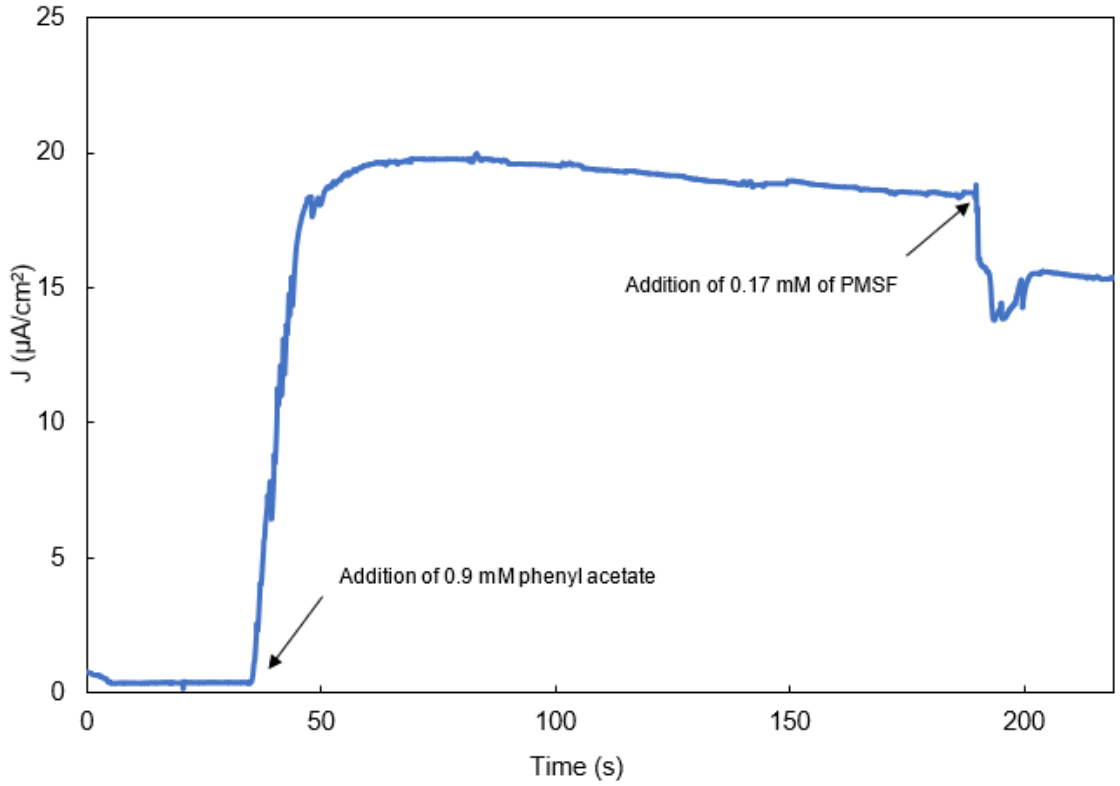

Figure 4.6. Current vs. time response of the bi-enzyme biosensor to the addition of phenylacetate (S_1) to obtain final phenylacetate (S_1) concentration of 0.9 mM followed by the addition of inhibitor PMSF to obtain a final PMSF concentration of 0.17 mM.

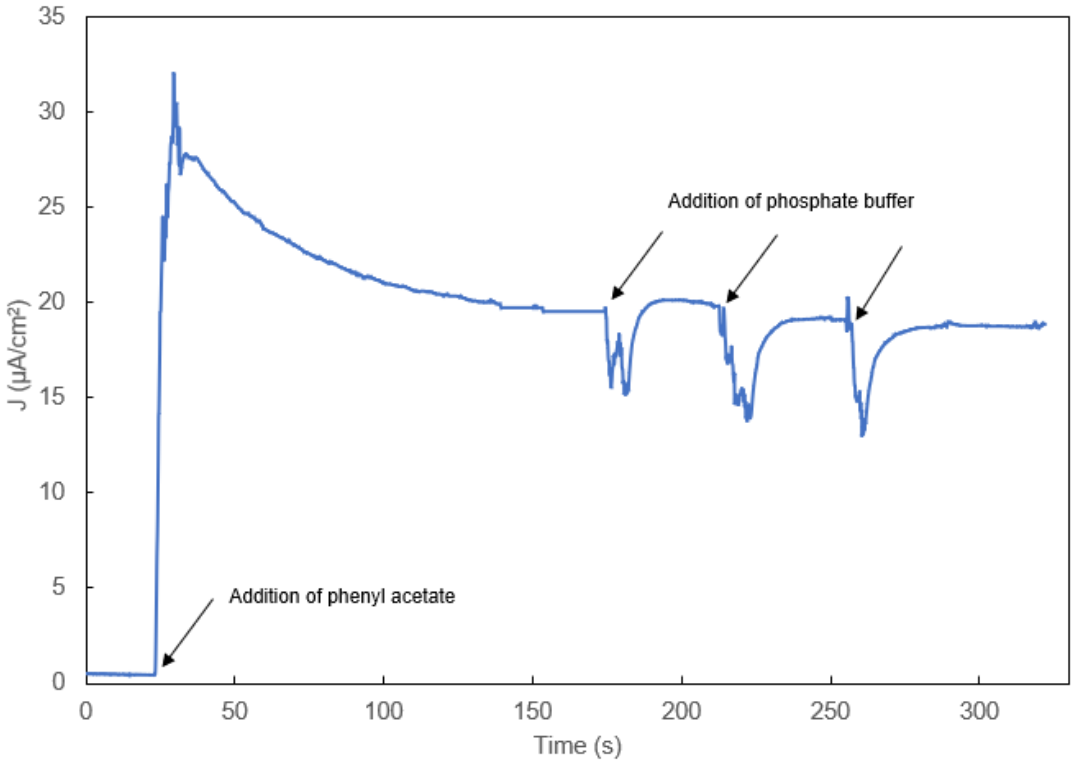

Figure 4.7. Control experiment to study the effect of phosphate buffer addition on the bi-enzyme biosensor's signal.

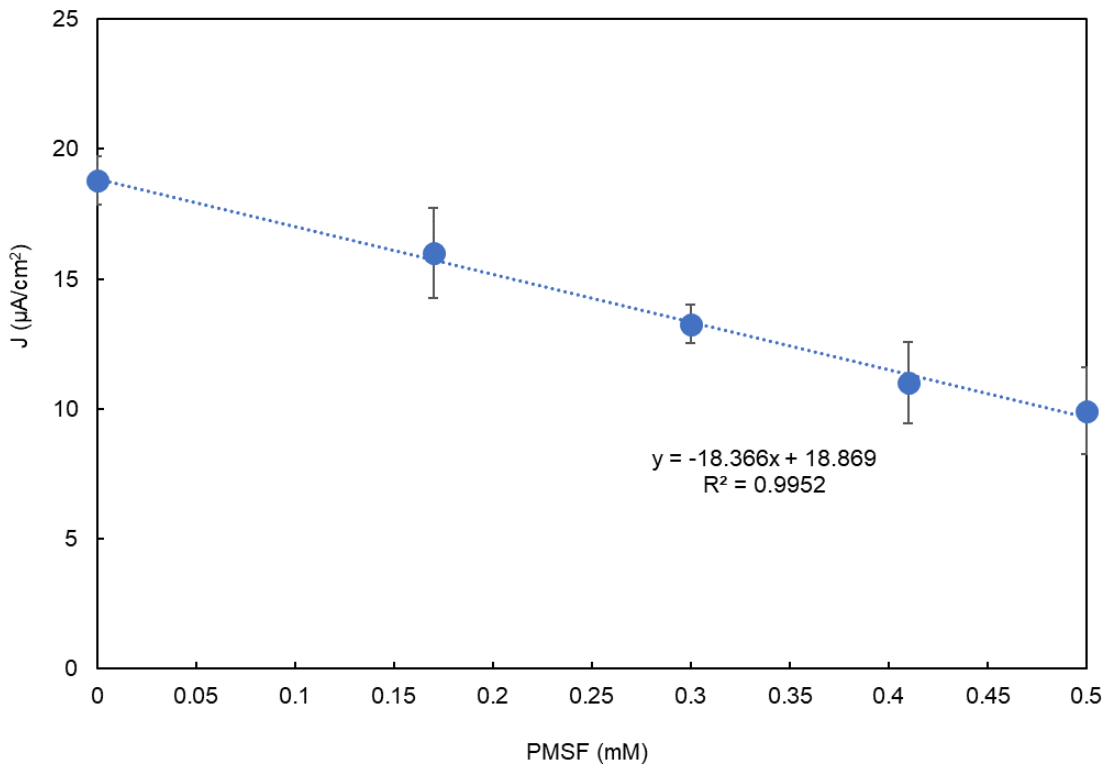

Figure 4.8. Current vs PMSF concentration. Error bars indicate mean ± standard deviation of 3 replicates. Phenylacetate: 0.9 mM.

4.4.2 Validation of the Mathematical Model and Simulation of the Biosensor's Response

Eqs 15-19 were solved numerically by applying a splitting finite difference technique in MATLAB and using the parameters/variables listed in Table 4.1. The numerical model successfully simulated the biosensor's behavior shown in Figures 4.7-4.8. To justify the shape of the current density after injection time (t=T_0) of PMSF (Figure 4.7), we hypothesized that part of this sharp drop in electric current density is caused by the mixing of the reaction solution while injecting PMSF. A control experiment (Figure 4.8) validated this hypothesis. We decided to simulate this observation using our mathematical model. Mixing would speed up the diffusion of the reactants (S_2, S_3, S_4) from the enzyme-containing layer to the diffusion layer. Having a lower concentration of these reactants would lower S_4 production and thereby lowering the current density. Over time, enzymatic

reactions replenish the lost reactants in the enzyme-containing layer and build up S_4, which results in the recovery of the current density (Figure 4.7). To formulize this phenomenon caused by mixing of the reaction solution, we added the below equations to our numerical simulation at the time that PMSF is added (Eqs 35-37):

$$[S_2]_{0<x<L,t=T_0^+} = 0.8 \times [S_2]_{0<x<L,t=T_0^-} \quad (35)$$

$$[S_3]_{0<x<L,t=T_0^+} = 0.8 \times [S_3]_{0<x<L,t=T_0^-} \quad (36)$$

$$[S_4]_{0<x<L,t=T_0^+} = 0.8 \times [S_4]_{0<x<L,t=T_0^-} \quad (37)$$

Table 4.1. Parameters and variables used in the numerical simulation.

Parameter/variable	Dimensional parameter	Variation range	Value used to fit experimental data
Time	t, s	0-300	--
Distance from electrode surface	x, cm	3.0×10^{-4}-3.0×10^{-2}	3.0×10^{-3}
Phenyl acetate concentration	$[S_1]$, mM	0-1.5	0.9
PMSF concentration	$[I]$, mM	0-0.5	--
Acetylcholinesterase concentration	$[E_1]$, μM	0-1000	10
Tyrosinase Concentration (phenolase activity)	$[E_2]$, μM	0-500	187
Tyrosinase Concentration (catecholase activity)	$[E_3]$, μM	0-500	187
Michaelis-Menten constant of phenyl acetate	$K_{m,1}$, mM	0-10	7.3
Michaelis-Menten constant of phenol	$K_{m,2}$, mM	0-10	2.5
Michaelis-Menten constant of catechol	$K_{m,3}$, mM	0-10	2.2
Acetylcholinesterase turnover number for phenyl acetate	$k_{cat,1}$, s^{-1}	2.0×10^{2}-2.0×10^{5}	2.3×10^{4}
Tyrosinase turnover number for phenol	$k_{cat,2}$, s^{-1}	2.0-2.0×10^{3}	20
Tyrosinase turnover number for catechol	$k_{cat,3}$, s^{-1}	2.0-2.0×10^{3}	760
Dissociation constant of PMSF	k_I, mM	0.02-2.0	0.003
Reaction constant of deactivation of acetylcholinesterase with PMSF	k_2, s^{-1}	0.001-1	0.1
Enzyme-containing layer thickness	L, nm	10-100	25
Diffusion layer thickness	$\boldsymbol{\delta}$, μm	10-200	30
Diffusion coefficient in diffusion layer	D_δ, $cm^2\ s^{-1}$	1×10^{-6}-9×10^{-5}	2.20×10^{-5}
Diffusion coefficient in enzyme-containing layer	D_L, $cm^2\ s^{-1}$	1×10^{-8}-9×10^{-6}	2.28×10^{-8}
Standard redox electrochemical potential of O-quinone	E^0, V	0.15	0.15
Heterogeneous electron transfer rate constant	K_0, $cm\ s^{-1}$	1×10^{-7}-1×10^{-4}	4×10^{-6}

What these equations explain is that values of $[S_2]$, $[S_3]$, and $[S_4]$ at the time just after the addition of PMSF (t= T_0^+) would be a fraction of their values at the time just before the addition of PMSF

(t=T_0^-). We assigned an arbitrary value of 0.8 to this fraction to get the best fit for our experimental data. The final values of parameters used in the numerical simulation to achieve the best fit for experimental data are listed in table 1. Figure 4.9Figure 4.10 show simulated the IBE's signal to PMSF.

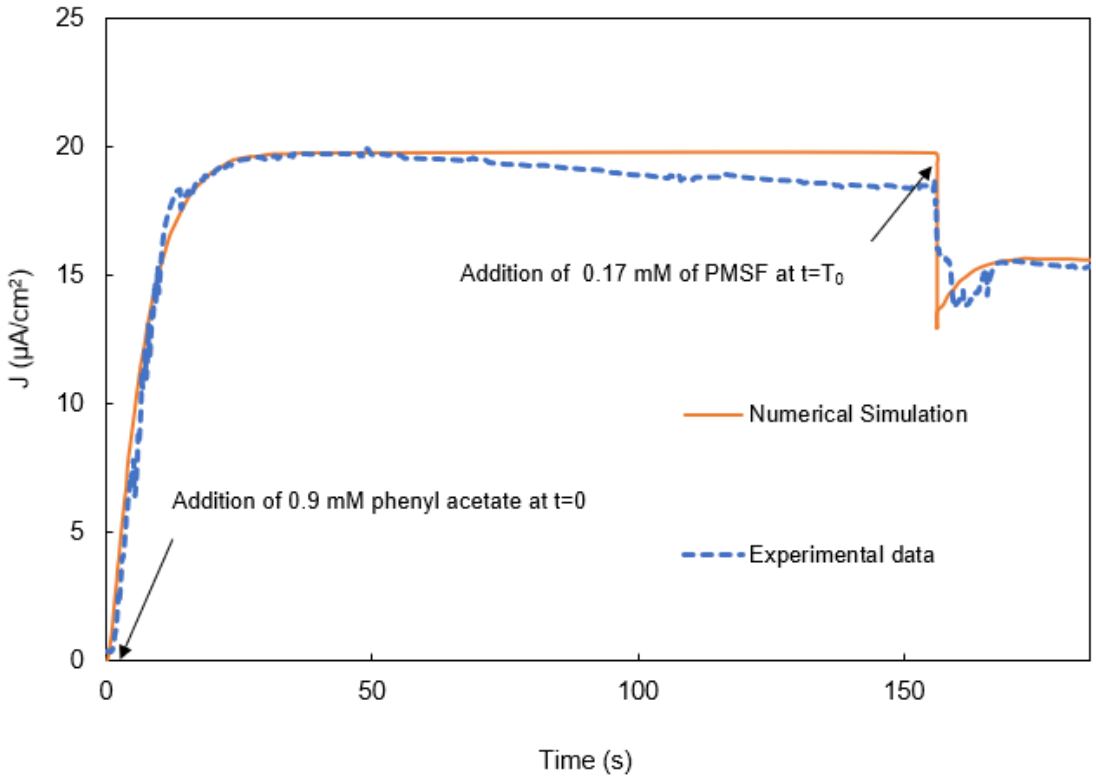

Figure 4.9. Simulated the bi-enzyme biosensor's signal vs. time.

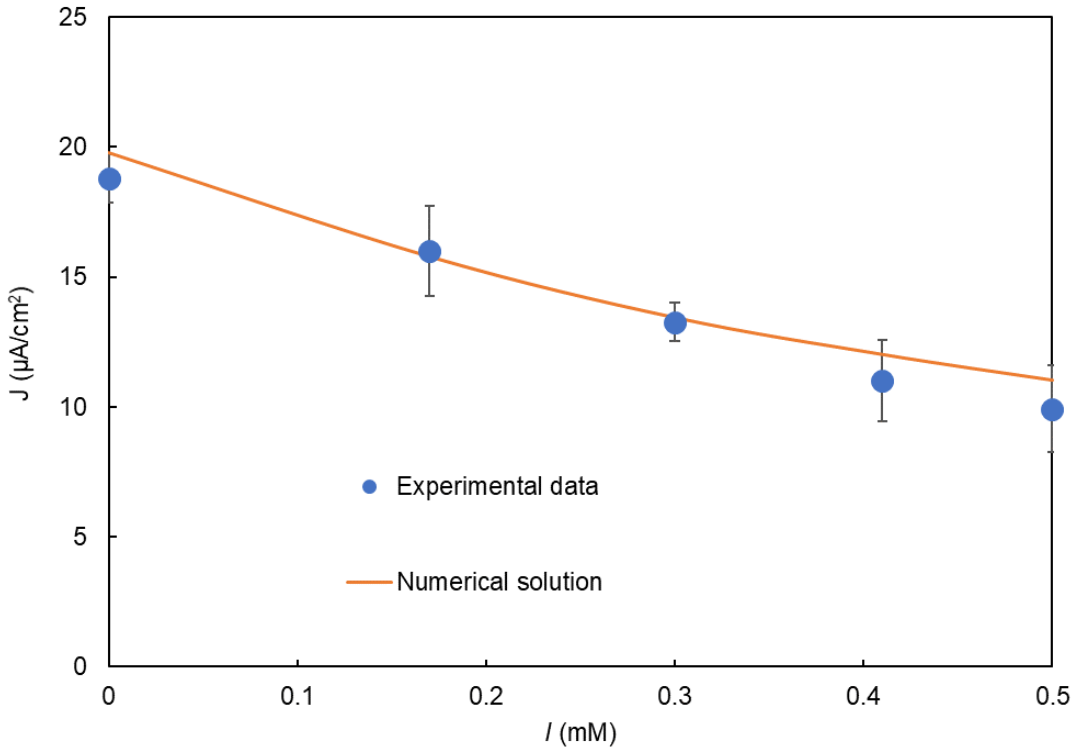

Figure 4.10. Simulated current density vs. PMSF concentration (I).

4.4.3 Signal Amplification

One of the features of the IBE is the built-in amplification system that amplifies the electric current by including an esterase (AChE) and an oxidase (Tyr). In the biosensor's interface, each produced phenol (S_2) molecule produced from the hydrolysis of phenol acetate by AChE can react with Tyr to produces O-quinone (S_4). O-quinone (S_4) reduction on the electrode surface results in an electric signal and catechol (S_3) production. Because Catechol (S_3) can be oxidized back to O-quinone by the Tyr's catecholase activity, it can lead to a substrate recycling system which amplifies the electric current. This amplification system is mainly caused by Tyr's catecholase activity. Therefore, amplification factor (AF) can be defined as the ratio of the electric current density (J) in the presence of catecholase activity and the absence of the catecholase activity (Eq 38) [115]:

$$AF=\frac{[J]_{E_3\neq 0}}{[J]_{E_3=0}} \quad (38)$$

We used the numerical model to simulate to what extend the amplification system has improved the biosensor's sensitivity. Figure 4.11 shows the simulated electric current in the presence and the absence of the amplification system. This result shows that the amplification system improves the bi-enzyme biosensor's performance for PMSF detection significantly. To set the amplification system zero, catecholase activity of Tyr (E3) was set to zero in the numerical model.

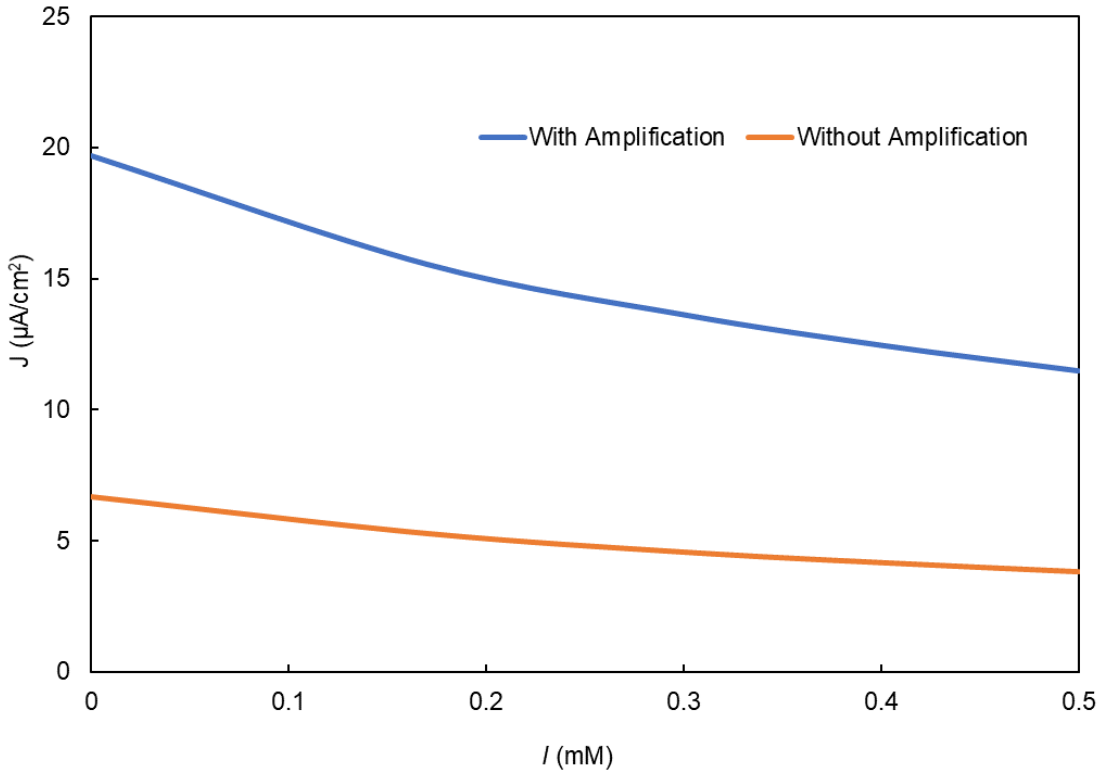

Figure 4.11. The simulated current density with and without (E3=0) amplification system in the bi-enzyme biosensor.

Figure 4.12 shows the effect of the catecholase activity (E3) on the amplification factor. This result shows increasing Tyr concentration would benefit the bi-enzyme biosensor's performance by enhancing the amplification system.

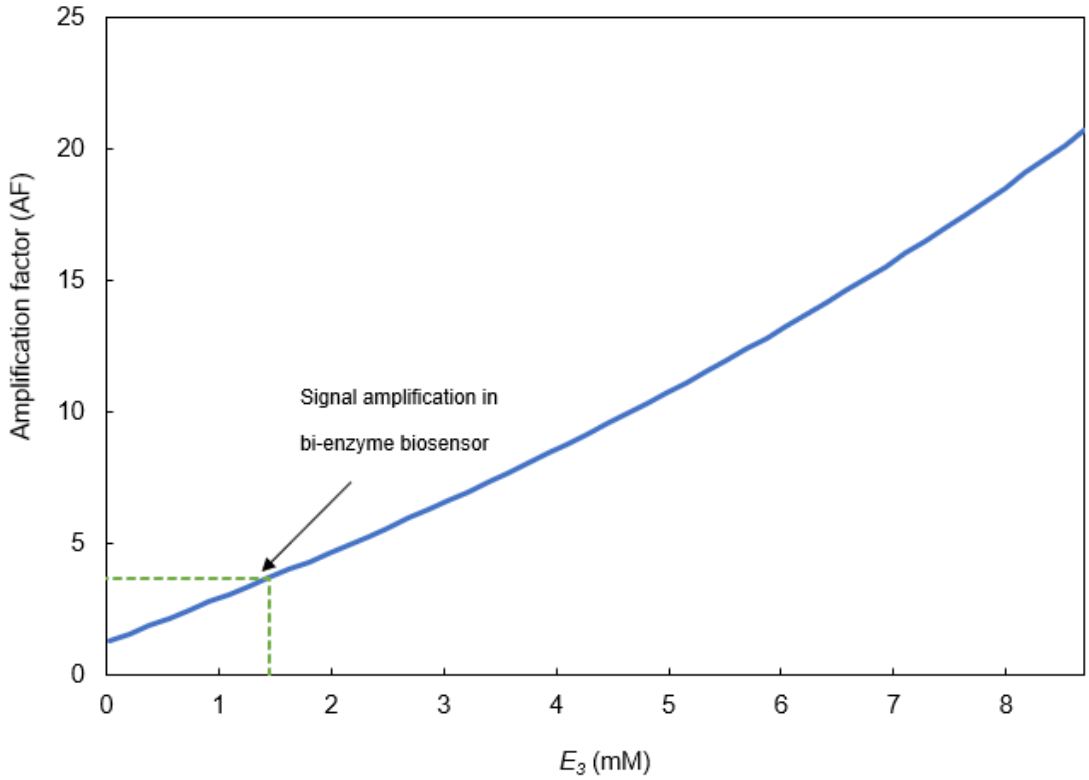

Figure 4.12. Signal amplification in bi-enzyme biosensor due to S3 recycling caused by catecholase activity (E3).

4.4.4 Biosensor's Sensitivity

One of the goals for the development of the numerical model was to optimize the governing factors, which can affect the IBE's performance. We defined a term called sensitivity (S) as a performance parameter to optimize the governing factors. The biosensor's sensitivity (S) with respect to PMSF (I) can be defined as Eq 39:

$$S = \frac{dJ}{dI} \tag{39}$$

To derive the sensitivity (S) for a set of the experimental condition using Eq 39, we changed [I] incrementally around a constant concentration of PMSF in the model and measured the corresponding dJ to calculate S.

Figure 4.13 shows sensitivity curve vs. phenylacetate concentration (S_1) increases until it reaches a maximum and passes that concentration, sensitivity starts to decrease. This result can be explained by the fact that PMSF competes with Phenyl acetate for the active site of AChE. Therefore, increasing phenylacetate concentration too much will lower the chance of PMSF reaching the active site of AChE and results in lowering the sensitivity for the detection of PMSF. Based on Figure 4.13, there is a concentration of phenylacetate under a set of experimental condition which would provide maximum sensitivity for detection of PMSF, and this concentration can be estimated using the model.

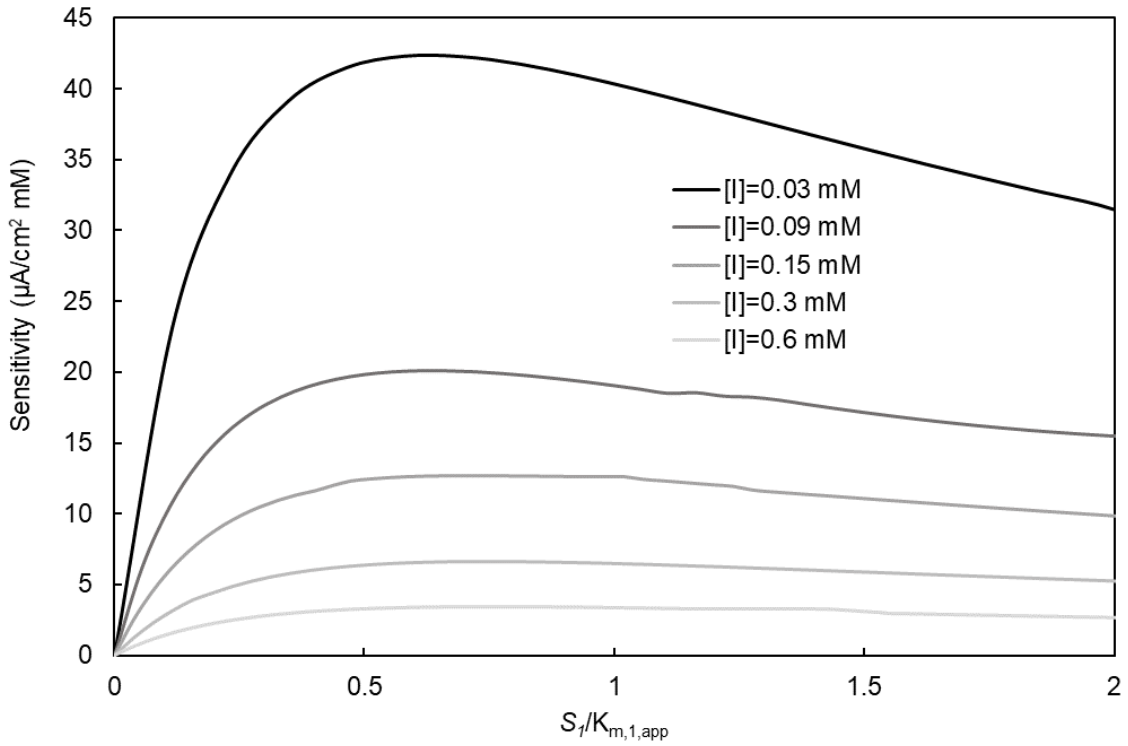

Figure 4.13. Sensitivity vs. phenylacetate concentration (S_1). S_1 was normalized with $K_{m,1,app}$.

Figure 4.14 shows that once the sensitivity curve vs. AChE (E_1) reached a maximum and passed that concentration; sensitivity gradually starts to decline. Having too much AChE present on the electrode lowers the sensitivity as it lowers the percentage change that a fixed amount of PMSF

can cause in the AChE activity. Besides, this graph shows that increasing Tyr would benefit sensitivity. This is mainly because increasing Tyr concentration enhances the amplification system.

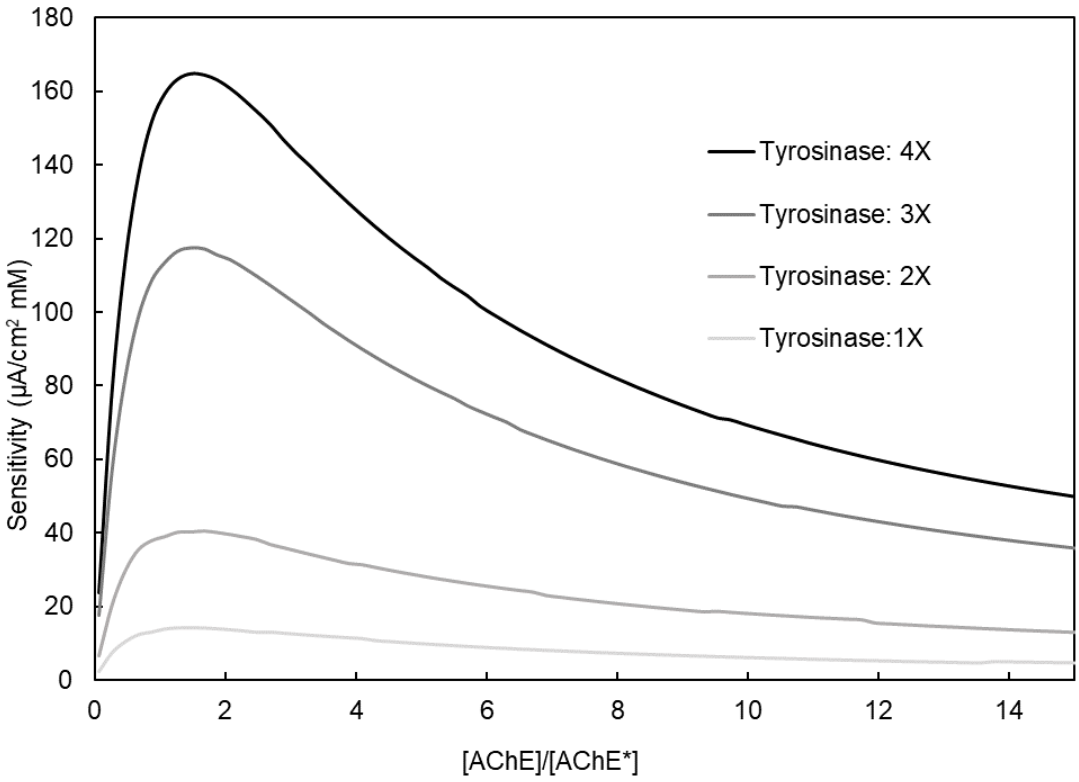

Figure 4.14. Sensitivity vs [AChE] at different tyrosinase concentrations. [AChE] was normalized with [AChE*] =3 μM. [I] = 0.3 mM.

4.4.5 Rate Limiting Step

The biosensor's signal is controlled by the rate of mass transfer and reaction steps, which all participate in the production of an electric current. The model allowed us to predict the rate of each step and analyze their effects on controlling the biosensor's signal.

$$\sigma^2 = \frac{V_{max}L^2}{D_L K_M} \tag{40}$$

We used Eq 40 and parameter values from Table 1 to calculate the Damkohler number (σ), defined as the squared root of the dimensionless ratio of the relative rates of enzymatic reaction ($\frac{V_{max}}{K_M}$) and diffusional mass transfer ($\frac{D_L}{L^2}$) within the enzyme-containing layer [126].

The σ values for AChE and Tyr were on the order of 10^{-5} indicating that the diffusion processes are many orders of magnitude faster than the reaction processes [127, 128].

Flux-control analysis has been used to determine the extent to which the rates of individual enzymatic reactions limit the overall mass flux through a metabolic pathway [129]. We adapted this approach to assess to what extent the enzymatic and electrochemical reaction steps limited current production by the biosensor.

A current-control coefficient (C_{Vi}^{J}) for a given reaction step (V_i) is defined as the ratio of the percent change in the overall pathway flux (J) to the percent change in V_i while holding all other independent variables constant (Eq 41). By analogy, we calculated current-control coefficients C_{Vi}^{J} by using the model to predict the percent change in the current generated per unit change in either the AChE reaction rate, Tyr reaction rate, or the electrochemical reaction rate. Based on the definition of V_{max}, we could vary the enzyme reaction rate by varying the assumed enzyme concentration value. Similarly, based on Eq 14, we could vary the electrochemical reaction rate by varying E and thus (E-E_h). Using this approach, C_{Vi}^{J} values were calculated for the enzymatic reactions and the electrochemical reaction.

Using the model, the effect of each governing factor on the current-control coefficient was simulated (Figures 4.15-4.17). These results help predict the step limiting the IBE's signal most under a certain experimental condition, then changing the experimental condition to the one that

gives the desirable results. For example, for the case of the IBE here, having the reaction step catalyzed by AChE (E_1) as the most rate limiting step would maximize the biosensor's sensitivity for the detection of PMSF. Figure 4.15 shows the current-control coefficient for the reaction step catalyzed by AChE (E_1). This result shows that increasing the amount of AChE decrease the role of AChE in controlling the current density. We found that changing applied voltage or Tyr concentration did not have a significant effect on this result. For the predicted value of 3 μM for AChE, a current-control coefficient of 0.52 is predicted.

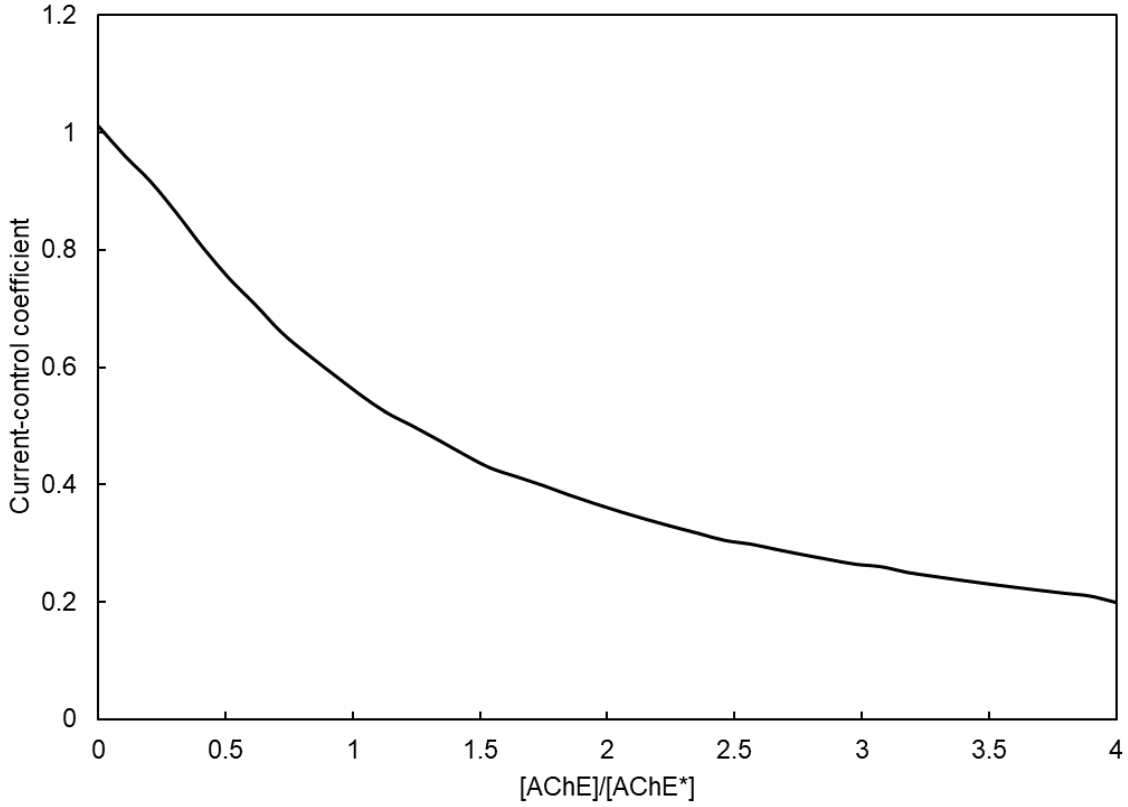

Figure 4.15. Current-control coefficient vs [AChE]/[AChE*].

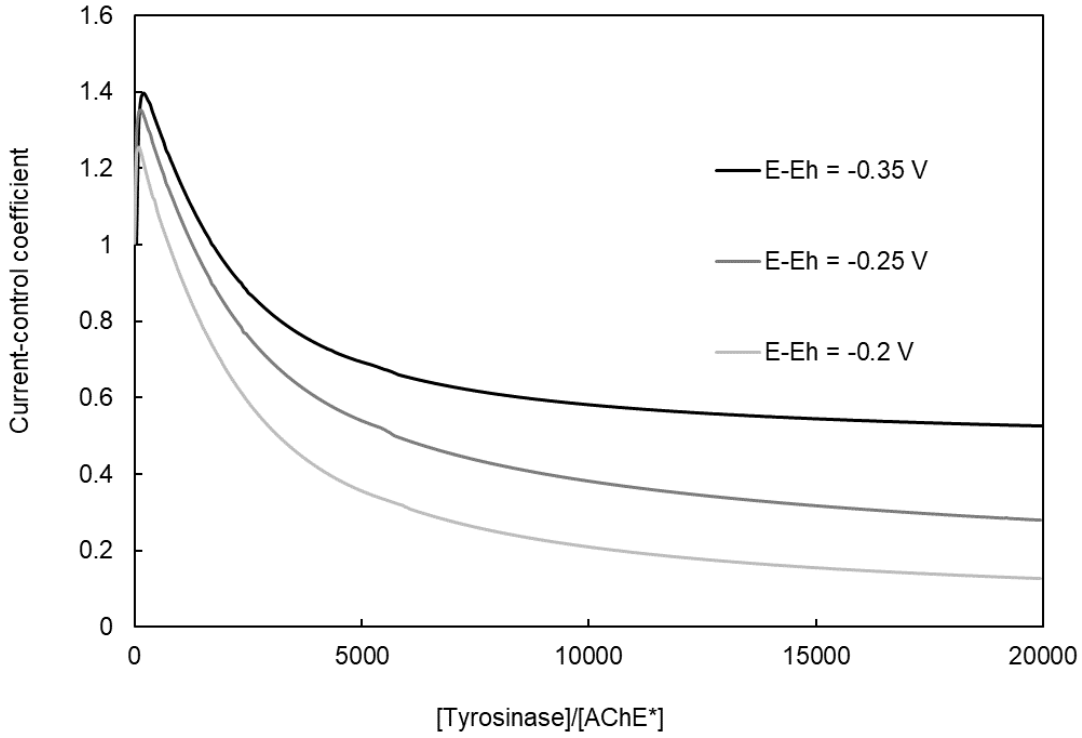

Figure 4.16. Current-control coefficient for tyrosinase. Tyrosinase concentration was normalized with [AChE*]=3μM.

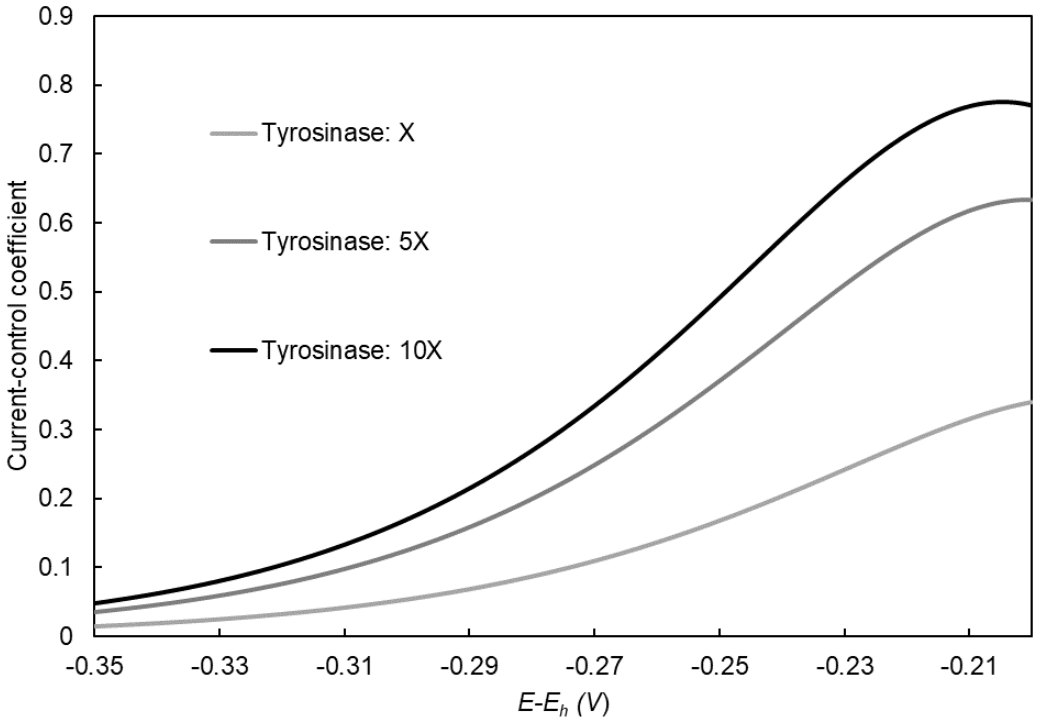

Figure 4.17. Current-control coefficient vs. applied voltage.

Figure 4.16 shows the current-control coefficient versus Tyr concentration. Tyr concentration includes both phenolase activity and catecholase activity. Figure 4.16 shows that the current-control coefficient has a greater value at the predicted value of Tyr concentration. This means that Tyr activity controls the current density more than the AChE activity. We obtained the current-control coefficient for Tyr under different values of applied voltages and AChE concentrations. We found that AChE concentration did not significantly affect the shape of current-control coefficient for Tyr whereas applied voltage showed a significant effect (Figure 4.16).

Figure 4.17 shows the current-control coefficient for the electrochemical reaction step as a function of the overpotential (E-E_0). At the applied overpotential of -0.35 V, the current-control-coefficient is close to zero, meaning that electrochemical reaction is happening much faster compared to the other steps. Because results from Figures 4.15-4.17 showed that Tyr activity has a bigger role in controlling the current density, the current-control coefficient for the applied voltage was also obtained at different Tyr concentrations (Figure 4.17). According to figure 4.17, increasing Tyr concentration increases the role of the electrochemical potential in controlling the current density. This means that at a higher Tyr concentration a more negative applied voltage is needed to get a current-control coefficient of close to zero. According to Figures 4.15-4.17, under the experimental conditions predicted by the model, the reaction step catalyzed by the Tyr has the maximum current-control-coefficient. This means that this step has a maximum effect on controlling the current density. The trends in Figures 4.15-4.17 shows that increasing an enzyme activity would lower the current-control-coefficient. Because having the AChE-catalyzed reaction as the most rate limiting step would be desirable, this model suggests that increasing the Tyr activity would benefit the biosensor's performance. At the same time, increasing Tyr concentration requires a more negative

applied voltage to secure that the AChE activity has maximum effect on controlling the current density.

4.5 Conclusions

In this work, an inhibition-based bi-enzyme electrochemical biosensor (IBE) was presented for the detection of organophosphorus compounds. The presented bi-enzyme biosensor was fabricated on screen-printed electrodes for a model inhibitor (PMSF) containing a hydrolase enzyme (AChE) and an oxidase enzyme (Tyr). The inclusion of the two enzymes provided an amplification system, which improved the biosensor's sensitivity significantly. An unsteady-state mathematical model was also developed to simulate the biosensor's signal. Concepts such as sensitivity and current-control-coefficient were defined to study the effect of each governing factor on the biosensor's performance. The model predicted effect of each governing factor on sensitivity and their role in limiting current density. With the aid of the model, a condition was predicted, which would maximize the sensitivity for detection of the inhibitor.

APPENDIX

MATLAB Codes

```
%%%%%%%%%%%%%%%%%%%%%%%%%%%%%%%%%%%%%%%%%%%%%%%
% Copyright: Neda Rafat, Mohsen Zeyernouri
% Time-Dependent BioSensor PDE modeling
% Feb. 10 to Dec. 4, 2019
%%%%%%%%%%%%%%%%%%%%%%%%%%%%%%%%%%%%%%%%%%%%%%%

clear All
format Long
%%
%%constants for the model
Si= 0.0009; %mol/cm3 Si:concentration of phenylacetate(S1) in the bulk
solution %Concentrations were normalized with Si
L= 2.5e-6; %thickness of the enzyme  layer
Df= 2.28e-8; %cm2/s %diffusion coefficient in the enzyme layer
De= 2.2e-5; %cm2/s %diffusion coefficient in the diffusion layer
Kp= 1; %partition coefficient, assumed to be one for all reactants
del = 3e-3; %thickness of the diffusion layer
k1= 1.2e+4;%1/s %turnover number of AChE for phenylacetate
k2= 20; %1/s %turnover number of Tyr for phenol
k3= 760;%1/s %turnover number of Tyr for catechol
K1= 73e-7; %mol/cm3 Km value for phenylacetate
K2= 2.5e-7;  %mol/cm3 Km value for phenol
K3= 2.2e-7;  %mol/cm3 Km value for catechol
E1= 1e-8; %AChE concentration
E2= 178e-8; %Tyr-phenolase concentration
E3= 178e-8; %Tyr-catecholase concentration
V=-0.2; %applied voltage in volt
Ka=4e-6; %electron transfer rate constant
F=96485; %Faraday constant
R=8.314;  %universal gas constant
T=293; %temperature in kelvin
area= 0.118; %cm2 %area of the working electode
Exp=exp((-F*0.8*((V-0.15)))/(R*T));%butler-volmer cathodic current
EXP=exp((F*1.2*((V-0.15)))/(R*T)); %butler-volmer anodic current
Vmax1=k1*E1;
Vmax2=k2*E2;
Vmax3=k3*E3;
KI=0.003; %mM %dissociation constant of PMSF
K12=0.1; %K2 %reaction rate constant of sulfonylation of AChE with PMSF


%constnats used in the PDEs:
constant1 = -1 ;
constant2 = 1;
constant3 =  -1 ;
constant4 =  1 ;
constant5 = -1;
kappa = Df; %
KAPPA = De/(del*Df);

%%
DeltaT= 0.001; % time-step
N=70000;
```

```
%total time= N*DeltaT
M= 100;   % The total numbr of spatial point in our computational domain
Dx = L/(M-1); % spacing
IterMax=15;
%%
% Allocation of memory for the field variables (vectors!)

C1_old = zeros(M,1); %C1 stands for phenyl acetate
C1_new = zeros(M,1);

C1_kp1 = zeros(M,1);
C1_k = zeros(M,1);

C2_old = zeros(M,1); %C2 stands for Phenol
C2_new = zeros(M,1);

C2_kp1 = zeros(M,1);
C2_k = zeros(M,1);

C3_old = zeros(M,1); %C3 stands for Catechol
C3_new = zeros(M,1);

C3_kp1 = zeros(M,1);
C3_k = zeros(M,1);

C4_old = zeros(M,1); %C4 stands for Quinone
C4_new = zeros(M,1);

C4_kp1 = zeros(M,1);
C4_k = zeros(M,1);

I_old = zeros(M,1);
I_new = zeros(M,1);

I_kp1 = zeros(M,1);
I_k = zeros(M,1);

x = zeros(M,1);
%%
% Setting the initial conditions
% Note: all concentration are normalized with bulk phenylacetate
concentration

for j=1:M
    x(j,1) = (j-1)*Dx;
    C1_old(j,1) = 0;
    C2_old(j,1) = 0;
    C3_old(j,1) = 0;
    C4_old(j,1) = 0;
    I_old(j,1) = 0;
end

for ll=1:N
    Time(ll,1)=(ll-1)*DeltaT;
```

```
end

  C1_old(M,1) = 1; %at time zero, phenylacetate concentration in the
diffusion layer equals bulk concentration
%%
    KP = ((I_old*K12)./(I_old+KI*ones(M,1)));
     INH=ones(M,1);
     Vmax1=k1*E1*INH;
     kminh=ones(M,1)+(1/KI)*I_old;

%InitialGuess

for TimeStep=1:N
    C1_k = C1_old;
    C2_k = C2_old;
    C3_k = C3_old;
    C4_k = C4_old;
     I_k = I_old;

    if TimeStep < 40000 % at time= 40000*DeltaT, PMSF was added

     I_old(M,1)=0;

    elseif (TimeStep >= 40000) && (TimeStep <= 40001) %this elseif coomand is
to simulate the sharp drop in currentcaused by mixing when adding PMSF

            C2_k = C2_old*0.8;
            C3_k = C3_old*0.8;
            C4_k = C4_old*0.8;

        I_old(M,1)=0.17; %inhibitor concentration
        KP = ((I_old*K12)./(I_old+KI*ones(M,1)));
        INH=exp(-KP*(TimeStep-40000)*(DeltaT/60));
        Vmax1=k1*E1*INH;
        kminh=ones(M,1)+(1/KI)*I_old;

    else

         I_old(M,1)=0.17;
         KP = ((I_old*K12)./(I_old+KI*ones(M,1)));
         INH=exp(-KP*(TimeStep-40000)*(DeltaT/60));
         Vmax1=k1*E1*INH;
         kminh=ones(M,1)+(1/KI)*I_old;

    end




for Iter=1:IterMax

    for j=2:M-1
        % to solve the problem iteratively, starting from an initial guess,
        % then iteratively converge to the new solution
```

```
        C1_kp1(j,1) = (1/(1 + 2*kappa*DeltaT/Dx^2))*(   C1_old(j,1)  +
kappa*DeltaT*(  C1_k(j+1,1) + C1_k(j-1,1) )/Dx^2 +    constant1*DeltaT*(
(Vmax1(j,1)*C1_old(j,1)/(K1*kminh(j,1) + Si*C1_old(j,1)) )   ));
        C2_kp1(j,1) = (1/(1 + 2*kappa*DeltaT/Dx^2))*(   C2_old(j,1)  +
kappa*DeltaT*(  C2_k(j+1,1) + C2_k(j-1,1) )/Dx^2 +    constant2*DeltaT*(
((Vmax1(j,1)*C1_old(j,1)/(K1*kminh(j,1) + Si*C1_old(j,1)))-
(Vmax2*C2_old(j,1)/(K2 + Si*C2_old(j,1)))) )   );
        C3_kp1(j,1) = (1/(1 + 2*kappa*DeltaT/Dx^2))*(   C3_old(j,1)  +
kappa*DeltaT*(  C3_k(j+1,1) + C3_k(j-1,1) )/Dx^2 +    constant3*DeltaT*(
(Vmax3*C3_old(j,1)/(K3 + Si*C3_old(j,1)) ) ) );
        C4_kp1(j,1) = (1/(1 + 2*kappa*DeltaT/Dx^2))*(   C4_old(j,1)  +
kappa*DeltaT*(  C4_k(j+1,1) + C4_k(j-1,1) )/Dx^2 +    constant4*DeltaT*(
(Vmax2*C2_old(j,1)/(K2 + Si*C2_old(j,1)))+(Vmax3*C3_old(j,1)/(K3 +
Si*C3_old(j,1)) ) ) );
         I_kp1(j,1) = (1/(1 + 2*kappa*DeltaT/Dx^2))*(   I_old(j,1)  +
kappa*DeltaT*(  I_k(j+1,1) + I_k(j-1,1) )/Dx^2 +    constant5*DeltaT*(-
KP(j,1)*E1*INH(j,1)));
    end


     % Applying the BCs at each time-step
    j=1;
%     C4_kp1(j,1) = 0;
     I_kp1(j,1) = I_kp1(j+1,1);
    C1_kp1(j,1) = C1_kp1(j+1,1);
    C2_kp1(j,1) = C2_kp1(j+1,1);
    C3_kp1(j,1) = C3_kp1(j+1,1) + C4_kp1(j+1,1) ;
    C4_kp1(j,1) = (C4_kp1(j+1,1) +
(Dx/(area*Df))*Ka*C3_kp1(j,1)*EXP)/(1+(Dx/(area*Df))*Ka*Exp);



    j=M;

    C4_kp1(j,1) = ( 1/(1+Dx*KAPPA) )*C4_kp1(j-1,1);
    C3_kp1(j,1) = ( 1/(1+Dx*KAPPA) )*C3_kp1(j-1,1);
    C2_kp1(j,1) = ( 1/(1+Dx*KAPPA) )*C2_kp1(j-1,1);
    C1_kp1(j,1) = (C1_kp1(j-1,1) + KAPPA*Dx )/(1+ Dx*KAPPA);
    I_kp1(j,1) = (I_kp1(j-1,1) + I_old(M,1)*KAPPA*Dx )/(1+ Dx*KAPPA);



     I_k = I_kp1;
    C1_k = C1_kp1;
    C2_k = C2_kp1;
    C3_k = C3_kp1;
    C4_k = C4_kp1;

end

   for j=2:M-1

         I_new(j,1)=I_kp1(j,1);
        C1_new(j,1)=C1_kp1(j,1);
```

```
        C2_new(j,1)=C2_kp1(j,1);
        C3_new(j,1)=C3_kp1(j,1);
        C4_new(j,1)=C4_kp1(j,1);

    end



     % Applying the BCs at each time-step
    j=1;

%     C4_new(j,1) = 0;
     I_new(j,1) = I_new(j+1,1);
    C1_new(j,1) = C1_new(j+1,1);
    C2_new(j,1) = C2_new(j+1,1);
    C3_new(j,1) = C3_new(j+1,1) + C4_kp1(j+1,1) ;
    C4_new(j,1) = (C4_new(j+1,1) +
(Dx/(area*Df))*Ka*C3_new(j,1)*EXP)/(1+(Dx/(area*Df))*Ka*Exp);

    j=M;


    C4_new(j,1) = ( 1/(1+Dx*KAPPA) )*C4_new(j-1,1);
    C3_new(j,1) = ( 1/(1+Dx*KAPPA) )*C3_new(j-1,1);
    C2_new(j,1) = ( 1/(1+Dx*KAPPA) )*C2_new(j-1,1);
    C1_new(j,1) = (C1_new(j-1,1) + KAPPA*Dx )/(1+ Dx*KAPPA);
    I_new(j,1) = (I_new(j-1,1) + I_old(M,1)*KAPPA*Dx )/(1+ Dx*KAPPA);

    % updating the old field

    QM(TimeStep,1)=C4_new(1,1);
    QMM(TimeStep,1)=C4_new(2,1);
    IMM(TimeStep,1)=I_new(1,1);
     I_old=I_new;
    C1_old=C1_new;
    C2_old=C2_new;
    C3_old=C3_new;
    C4_old=C4_new;


%%%%%%%%%%%%%%%%%%%%%%%%%%%%%%%%%%%%%%%%%%%%%%%%%%%%%%%%%%%%%%%%%%%%%%%%%%%%%
%%%%%%%%%%
end
Initial2(:,1)=C1_new;
Initial2(:,2)=C2_new;
Initial2(:,2)=C3_new;
Initial2(:,4)=C4_new;
% xlswrite('initial.xls', Initial2, 'Sheet 1', 'A1');
AAA=QM;
aaa=QMM;
J=2*96485*Df*Si*(1000000)*(QMM-QM)/Dx;
% xlswrite('current.xls', J);
hold
plot(Time,J) %normalized current density
plot(Time, IMM)
```

```
xlabel('Time(s)')
ylabel('Current Density (microamp/cm^2)')
hold

% all concentrations are normalizzed to bulk concentration of phenylacetate
(Si)
% figure;
% plot(x/L,C1_new) %normalized phenyl acetate
%
% figure;
%
% plot(x/L,C2_new) %normalized phenol
%
% figure;
% plot(x/L,C3_new) %normalized catechol
%
%
% figure;
% plot(x/L,C4_new) %normalized Quinone
```

5 Use of Electrochemical Detection Techniques for *Listeria Monocytogenes* Ongoing Research

5.1 Introduction

This chapter will discuss how our previous research in the field of electrochemical immunosensors and chemotaxis can be applied for *Listeria monocytogenes* (*LM*) research. This research was conducted in collaboration with Dr. Jonathan Hardy's lab, which has expertise in the foodborne pathogenic bacterium *LM*. *LM* is a facultative anaerobic, gram-positive, pathogenic bacterium that causes the infection listeriosis [149]. Listeriosis, a serious infection that has a global mortality rate of 24 %, is most likely to infect high-risk population groups, including pregnant women, their fetuses, adults over 65 years old, and immunocompromised people [63]. According to the Centers for Disease Control and prevention (CDC), 1600 cases of listeria are diagnosed within the United States annually, resulting in 260 deaths. *LM* can grow and survive under a wide range of environmental conditions, including high salt concentrations, aerobic and anaerobic environments, refrigeration temperatures, and acidic conditions. Besides, *LM* can produce biofilms on food production equipment, thereby sheltering LM cells from sterilization methods. For these reasons, *LM* has proven to be a ubiquitous and persistent foodborne pathogen [63, 64].

To help avoid health risks associated with *LM*, it is important to detect this pathogen in food-processing environments and food samples [65] and as well as to learn more about the mechanisms this bacterium uses to survive under adverse conditions. Some of the common detection methods of *LM* are culturing, biosensors, enzyme linked immunosorbent assay (ELISA), and polymerase chain reaction (PCR) [65].

Recently, *LM* was shown to secrete biologically active extracellular vesicles (EVs) despite the cells' having a thick cell wall and no outer membrane [66-68]. These EVs, with a diameter ranging from 20 to 200 nm, can be used as toxin cargo to transport concentrated virulence factors to host cells [66]. We hypothesized thatan EEIB could be developed for detection of EVs secreted by *LM.* To our knowledge, this woulf be the first time that an electrochemical biosensor would have been developed for that purpose.

Moreover, a recent study has shown that *LM* can respire under anaerobic conditions using an extracellular electron transfer mechanism (EET). In EET, cells discard electrons generated during respiration by using molecular electron carriers to transporting the electrons from the cytosol to the exterior of the cell [150], rather than by reacting them with O_2 to form H_2O. This study also showed that FmnB, a flavin containing membrane protein, plays an important role in the LM's EET mechanism [151].

Previously, a collaboration between the laboratories of Dr. Worden and Dr. James Tiedje demonstrated for the first time a new mechanism by which the motile, facultative anaerobe *Shewanella oneidensis*, locates extracellular electron acceptors needed to carry out EET. In this new mechanism, denoted mediated energy taxis, *S. oneidensis* secretes a reduces electron carrying molecule (e.g., the flavin derivative riboflavin), which served as both an electron shuttle and a chemoattractant to direct cell movement toward local insoluble electron acceptors (IEA). The reduced riboflavin diffuses away from the cells in all directions. Molecules that encounter an IEA (e.g. an iron oxide particle) are oxidized. The resulting oxidized riboflavin diffuses away from the IEA particle, creating a spatial gradient of the oxidized riboflavin, which serves as a chemoattractant for *S. oneidensis* cells that draws the cells to the IEA particle [152-155].

Based on these recent discoveries, we hypothesized that *LM* also uses an oxidized flavin derivative as a chemoattractant to direct bacteria movement toward IEA particles. We also hypothesized that secreted EVs by *LM* may contain a reduced flavin or FmnB, and the cells can migrate toward secreted EVs that contained oxidized flavin or FmnB.

To test this hypothesis, we developed develop swarm plate assays (motility assays) to study *LM* chemotaxis. In Dr. Worden's previous research swarm plate assays have provided graphical measurement of chemotaxis rates and been used to validate mathematical models of chemotaxis for E. coli and S. oneidensis[70, 152]. . This chapter will discuss the motility assays of *LM* in complex media and a defined media.

Initial motility assays were performed in a semi-solid complex media, brain-heart infusion (BHI) to confirm motility of *LM* and optimize temperature and agar concentration for the motility assay. Then, a chemically defined medium was formulated for *LM* to study chemotaxis of *LM*. Having a chemically defined medium allows us to study the chemotactic behavior of *LM* under a controlled growth environment, and it allows to adjust the concentration of each chemical. The defined medium will be useful to investigate LM's chemotactic properties, and possibly energy taxis, to riboflavin and external electron acceptors such as iron oxide.

As described below, promising results were obtained for the motility assays of *LM* in a complex media and a chemically defined media. However, this project was paused due to the COVID-19 pandemic. Suggestions for the continuation of this project and future work will be discussed in the next chapter.

5.2 Materials and Instrumentation

Brain heart infusion broth (BHI), RPMI 1640 amino acid solution (50X), RPMI-1640 vitamin solution mix (100X), thioctic acid, UltraPure™ Agarose, M9 Minimal Salts, 5X, magnesium sulfate, L-glutamine, glucose, and ferric citrate were purchased from Sigma Aldrich. *Listeria monocytogenes* WT strain 10403S and luminescent 10403S (C1) were used for the motility assays.

5.3 Experimental Methods

5.3.1 Cultivating *LM*

A day before performing motility assays, *LM* was streaked out on a 4% BHI agar plate and incubated at 30 ℃ for 24 hours. A sterile platinum wire was used to transfer cultivated cells for inoculation of plates.

5.3.2 Preparation of Chemically Defined Media for *LM*

Table 5.1 includes the final concentrations for a previously developed defined media [156] for *LM* and two different formula that were developed in our work to optimize the motility assays. M9 minimal media was prepared following the instruction provided by Sigma Aldrich. The optimized defined media was prepared by mixing the following solutions: 20 mL of 5X M9 media, 20 mL of 5X amino acid solution, 2 mL of 30 g/L L-glutamine, 10 mL of 100 g/L glucose, 1 mL of 0.2 g/L of ferric citrate, 1 mL of 40 g/L of magnesium sulfate, and 0. 5 mg/L thioctic acid in ethanol. The total volume was brought to 95 mL with DI water (5 mL was saved for the addition of agarose solution).

5.4 Motility Assay

Agar plates (BHI or chemically defined media) were prepared with different agar concentrations: 0.4 %, 0.3 %, 0.2 %, 0.15 %, 0.1 %. A 6 % stock agar solution was prepared in DI water. To prepare an agar plate, an appropriate amount of the melted stock agar solution was added to the

media. 10 mL of the media containing agar solution was added to a 6 mm petri dish. The petri dish was stored at 4 ℃ for four hours, and afterward it was ready for inoculation. Next, each plate was inoculated with *LM* using the tip of an inoculation wire that contacted the cultivated *LM*. Then, plates were incubated at 30 ℃ or 24 ℃ (Note: The inoculation wire was sterilized with flame before carrying the *LM*. To inoculate properly, it is important to prevent contacting of the wire from the bottom of the plate. The inoculation wire was inserted in the agar plate for around 2 mm).

5.5 Results and Discussion

5.5.1 Optimization of agar concentration and temperature

Temperature and agar concentration are two significant factors affecting motility of *LM*. We performed motility assays for wild type (WT) strain in BHI with different agar concentrations (0.4 %, 0.3 %, 0.2 %, 0.15 %, 0.1 %) and at two different incubation temperatures (24 ℃ and 30℃). We found a 0.15 % agar concentration, and a temperature of 24 ℃ gave the best result for the motility of *LM,* and this condition was selected for the next assays.

5.5.2 Motility Assay in Complex Media (BHI)

Motility (swarm plate) assay provides qualitative observation of chemotaxis. Besides motility assays of wild type *LM* , we were also interested to study motility assays of a luminescent strain of *LM* because bioluminescence imagining of the plates would provide a quantitative measure of bacteria growth. In Dr. Hardy's lab**,** WT strain 10403S was made luminescent by chromosol integration of *lux-kan* transposon cassette. Using this technique, a motile luminescent strain (1C) was created [157]. Figure 5.1 shows the motility assay for luminescent strain (1C) in 0.15 % agar plate at 25 ℃.

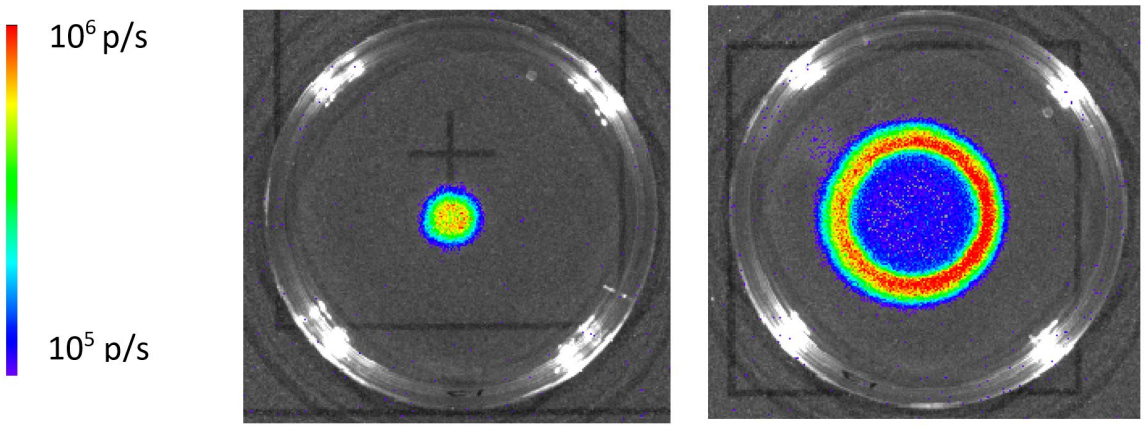

Figure 5.1. Motility assays of luminescent LM (1C) in 0.15% agar in BHI.

5.5.3 Motility Assay of *LM* in a Chemically Defined Media

After confirming the motility of wild type and luminescent strains of *LM* in a complex media, we sought to develop a chemically defined media that would allows chemotaxis of *LM* to be studied under a known and controlled growth environment. Table 5.1 shows the chemical concentrations in each defined media. Using the first developed media, we did not observe a successful growth for *LM* (Figure 5.2.A). In the next defined media, we increases amino acid concentrations, and we added magnesium sulfate and thioctic acid to the media. This media successfully supported *LM* growth in the motility assay (Figure 5.2.B).

Table 5.1. Chemical formula for chemically defined media of LM.

Chemical	MWB media	This work (unoptimized)	This work (optimized)
$KH2PO_4$	6.56 g/L	15 g/L	15 g/L
$NaHPO_4.7H_2O$	30.96g/L	33.9 g/L	33.9 g/L
$MgSO_4.7H_2O$	0.41g/L	0	0.4 g/L
Ferric citrate	0.088 g/L	0.02 g/L	0.02 g/L
Glucose	10 g/L	50 mM glycerol	10 g/L
L-Leucine	0.1 g/L	0.05 g/L	0.5 g/L
L-Isoleucine	0.1 g/L	0.05 g/L	0.5 g/L
L-Valine	0.1 g/L	0.025 g/L	0.25 g/L
L-Methionine	0.1 g/L	0.015 g/L	0.15 g/L
L-Arginine	0.1 g/L	0.2 g/L	2 g/L
L-Cysteine	0.1 g/L	0.05 g/L	0.5 g/L
L-Histidine	0	0.015 g/L	0.15 g/L
L-Tryptophan	0	0.005 mg/L	0.05 g/L
L-Glutamine	0.6 g/L	0.6 g/L	0.146 g/L
Riboflavin	0.5 mg/L	0.2 mg/L	0.4 mg/L
Thiamine	1.0 mg/mL	1 mg/L	2 mg/L
Biotin	0.5 mg/L	0.2 mg/L	0.4 mg/L
Thioctic acid	0.005 mg/L	0	0.005 mg/L

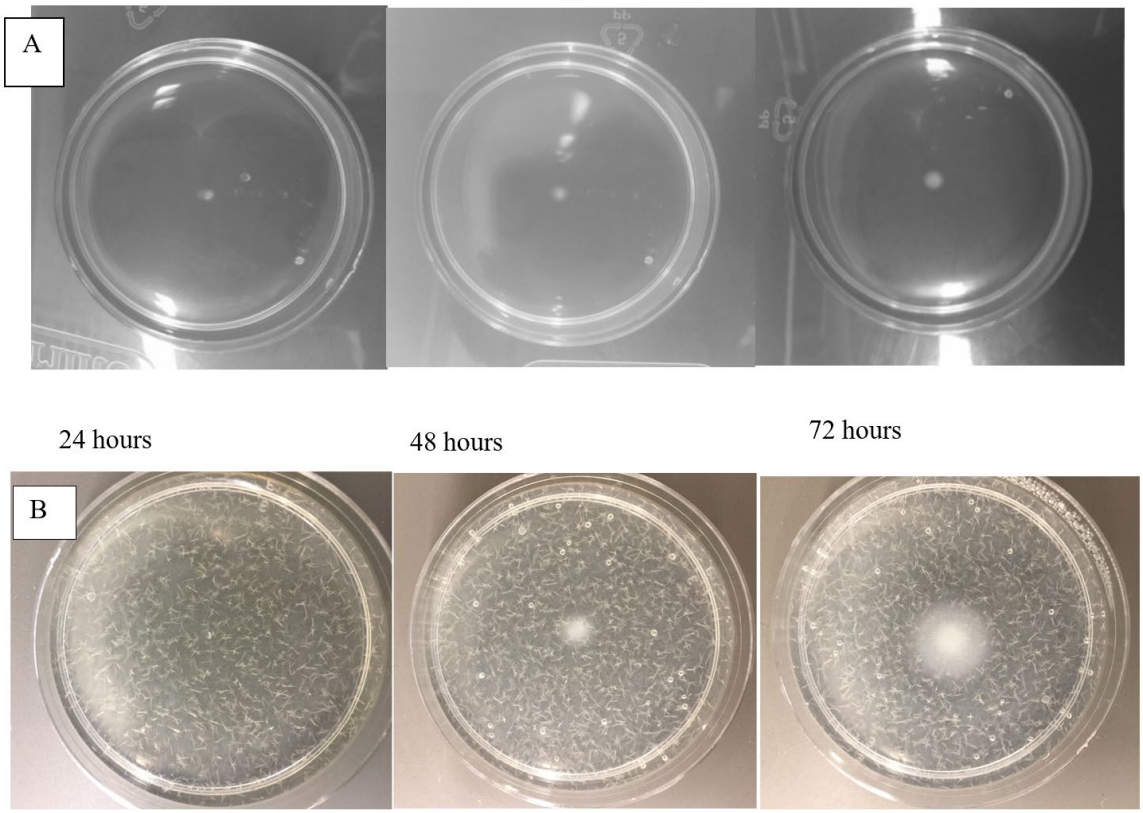

Figure 5.2. A: Motility assay of wild type LM in the unoptimized defined media. B: Motility assay of wild type LM in the optimized defined media. Some crystals were formed after the addition of magnesium sulfate in the optimized media.

5.6 Conclusion

In this chapter, we developed motility assays of WT, and luminescent strains of *LM* in a complex media; the agar concentration and temperature were optimized for these motility assays. Because we were interested in studying chemotaxis of *LM*, a chemically defined media was developed to study *LM* chemotaxis under a controlled growth condition. We developed a formulation for a chemically defined media which successfully supported WT *LM* growth and facilitated a motility assay for *LM* under known growth conditions.

6 Summary and Recommendations for Future Work

6.1 Summary

This dissertation describes , experimental and theoretical studies of two types of electrochemical biosensors. The first type, an electrochemical immunosensor (EI), was fabricated on screen-printed electrodes (SPEs) for the detection of a model analyte (mouse IgG). The EI concept inintegrates the principles of an enzyme-labeled immunosorbent assay (ELISA) and an electrochemical transducer using horseradish peroxidase (HRP) as the labeling enzyme. High throughput optical ELISAs were used to validate the functionality of antibodies against an analyte to aid in developing the EI. The experimental conditions, such as substrates concentrations, pH, and applied voltage, were optimized using a fractional factorial design. A mechanistic mathematical model was developed to simulate the steady-state signal in the EI by solving a system of coupled, non-linear ordinary differential mass-balance equations that described the rates of chemical reaction and diffusion-based mass transfer rates for all the reactants. A new dimensionless group, the current-control coefficient, was defined and used to characterize the extent that each reaction and/or mass-transfer step limits the current density. The mathematical model and associated new dimensionless groups provide powerful new tools fop to predict the rate-limiting step and optimize experimental conditions for improving the sensitivity of detection for EIs, and the current-control-coefficient concept could also be extended to other types of amperometric biosensors.

The second type of electrochemical biosensor, a bi-enzyme electrochemical biosensor containing AChE was also fabricated on SPE. It's ability to detect a model AChE inhibitor, phenylmethylsulfonyl fluoride (PMSF), was then characterized. The bi-enzyme biosensor had AChE and tyrosinase coimmobilized on the gold working electrode. The use of a substrate (phenylacetate) that was cleaved by AChE to produce phenol, together with the phenolase and

catecholase activities of tyrosinase, provided a redox-recycle signal amplification system that significantly improved the biosensor's sensitivity. A mechanistic, unsteady-state mathematical model was developed to simulate the time-dependent electrochemical signal in the IBE. The model consisted of a system of coupled, non-linear, partial differential mass-balance equations that described the rates of chemical reaction and diffusion-based mass transfer for all the reactants, including PMSF. The model was able to reproduce dynamics of the bi-enzyme amperometric biosensor's response a step change in the phenylacetate and PMSF. Using the model and the current-control coefficient and sensitivity parameters, the effects of the governing factors, (e.g., the relative concentrations of the AChE and tyrosinase enzymes on the working electrode) on the biosensor's sensitivity were characterized. The model and associated dimensionless groups provide new insights that can facilitate efforts to design and optimize be-enzyme biosensors in general, and biosensors to AChE inhibitors specifically.

Finally, we established the groundwork for developing an EI biosensor to detect EVs produced by *Listeria monocytogenes* (*LM*). Such a biosensor would be valuable for two purposes. First, it could be used to detect the presence of *LM* in a sample (e.g. a food product). Second, it could be use to measure the role of *LM* EVs in extracellular electron transfer (EET), which enables facultative anaerobic bacteria like *LM* respire in the absence of oxygen by shuttling the electrons from the inside the cell to electron acceptors in the extracellular enviroment. We hypothesized that *LM* might use EVs to transport electrons produced in anaerobic respiration away from the cell and to help identify the location of nearby extracellular electron acceptors. To help test this hypothesis, we developed motility assays for *LM*in both complex media and a chemically defined medium.

6.2 Enzyme Linked Immunosorbent Assay (ELISA)

In this chapter, optical ELISAs for detection of two different analytes, mouse IgG and extracellular vesicles from breast cancer cells, were presented. Because ELISAs provide a high throughput platform to develop standard immunoassays, they were used to find suitable bioreceptors to detect the analyte of interest before developing an electrochemical immunosensor. It is suggested that similar optical ELISA studies be conducted to detect EVs from *LM.* To our knowledge, no such ELISA assay has been developed. . Based on the literature review of proteomics of EVs from *LM*, we suggest that ActA protein (a membrane protein found in *LM*'s EVs) be evaluated as a surface biomarker for detecting EVs secreted by *LM*. Antibodies against *LM*'s ActA protein are commercially available.. Once a successful ELISA is developed, the same antibody would be integrated with an electrochemical transducer to develop an electrochemical immunosensor for the detection of EVs from *LM*.

6.3 Integrated Experimental and Teoretical Studies on an Electrochemical Immunosensor (EI)

In this chapter, theoretical and experimental studies of an EI for a model antigen, mouse IgG, were presented. The model is suitable to optimize the steady-state current in the EI. We recommend that the model be extended to include equations describing equilibrium partitioning of the antigen binding to the immobilized captured antibody and enzyme-labeled detection antibody. This extension would allow investigators to optimize antibody concentrations and estimate HRP concentration as a function of analyte concentration. This capability would be useful for optimization of antibody-antigen kinetics and designing EIs that meet specific performance criteria.

6.4 Theoretical and Experimental Studies of an Inhibition-based Bi-enzyme Electrochemical Biosensor (IBE) for Detection of Organophosphorus Compounds

In this chapter, theoretical and experimental studies of a bi-enzyme biosensor for a model inhibitor of AChE, PMSF, were presented. We recommend that the commercial prospects of an SPE to detect toxic OPs that are widely used in agriculture, such as methamidophos, be evaluated. Such a biosensor would enable food and environmental samples to be checked for the presence of OPs that pose serious health issues for non-targeted species such as human and animals. The mathematical model could be applied to an OP of interest by adding its inhibition kinetic constants to the model. Using the model, governing factors such as AChE concentration, Tyr concentration, applied voltage and substrate concentration could be optimized for achieving optimum sensitivity for the inhibitor.

6.5 Use of Electrochemical Detection Techniques for *Listeria Monocytogenes* Ongoing Research

In this chapter we proposed that *LM* EVs are might be used to discard electrons produced during anaerobic respiration and that they might be involved in an energy-taxis mechanism to increase *LM* cells' chances of survival under anaerobic conditions. To test this hypotheses, we recommend that an EI be developed to detect EVs generated by *LM* . We also recommend that the chemically defined media we formulated for *LM* motility assays be used to assess *LM* chemotaxis in the presence of oxidized flavins (e.g., riboflavin) and its own EVs after they have been oxidized. These experiments could provide important insight into *LM*'s persistence in food-processing plants and its pathogenicity.

REFERENCES

REFERENCES

1. Cammann, K., *Bio-sensors based on ion-selective electrodes.* Fresenius' Zeitschrift für Analytische Chemie, 1977. **287**(1): p. 1-9.

2. Karunakaran, C., R. Rajkumar, and K. Bhargava, *Introduction to biosensors*, in *Biosensors and bioelectronics*2015, Elsevier. p. 1-68.

3. Yoon, J.-Y., *Introduction to biosensors: from electric circuits to immunosensors*2016: Springer.

4. Mehrotra, P., *Biosensors and their applications–A review.* Journal of oral biology and craniofacial research, 2016. **6**(2): p. 153-159.

5. Eggins, B.R., *Biosensors: an introduction*2013: Springer-Verlag.

6. Cass, T., *Biosensors*2004: Oxford University Press.

7. Gorton, L., *Biosensors and modern biospecific analytical techniques*2005: Elsevier.

8. Scheller, F. and F. Schubert, *Biosensors*1991: Elsevier.

9. Knopf, G.K. and A.S. Bassi, *Smart biosensor technology* 2018: CRC press.

10. Ronkainen, N.J., H.B. Halsall, and W.R. Heineman, *Electrochemical biosensors.* Chemical Society Reviews, 2010. **39**(5): p. 1747-1763.

11. Eggins, B.R., *Chemical sensors and biosensors*. Vol. 28. 2008: John Wiley & Sons.

12. Grieshaber, D., et al., *Electrochemical biosensors-sensor principles and architectures.* Sensors, 2008. **8**(3): p. 1400-1458.

13. Ducheyne, P., *Comprehensive biomaterials II*2017: Elsevier.

14. Pisoschi, A.M., *Potentiometric biosensors: concept and analytical applications-an editorial.* Biochem Anal Biochem, 2016. **5**(3): p. 19-20.

15. Pereira, A., M. Sales, and L. Rodrigues, *Biosensors for Rapid Detection of Breast Cancer Biomarkers*, in *Advanced Biosensors for Health Care Applications*2019, Elsevier. p. 71-103.

16. Bahadır, E.B. and M.K. Sezgintürk, *A review on impedimetric biosensors.* Artificial cells, nanomedicine, and biotechnology, 2016. **44**(1): p. 248-262.

17. Wang, J., *Amperometric biosensors for clinical and therapeutic drug monitoring: a review.* Journal of pharmaceutical and biomedical analysis, 1999. **19**(1-2): p. 47-53.

18. Lequin, R.M., *Enzyme immunoassay (EIA)/enzyme-linked immunosorbent assay (ELISA).* Clinical chemistry, 2005. **51**(12): p. 2415-2418.

19. Borrebaeck, C.A., *Antibodies in diagnostics–from immunoassays to protein chips.* Immunology today, 2000. **21**(8): p. 379-382.

20. Aydin, S., *A short history, principles, and types of ELISA, and our laboratory experience with peptide/protein analyses using ELISA.* Peptides, 2015. **72**: p. 4-15.

21. Crowther, J.R., *ELISA: theory and practice*. Vol. 42. 1995: Springer Science & Business Media.

22. Engvall, E., *[28] Enzyme immunoassay ELISA and EMIT*, in *Methods in enzymology*1980, Elsevier. p. 419-439.

23. Andaloussi, S.E., et al., *Extracellular vesicles: biology and emerging therapeutic opportunities.* Nature reviews Drug discovery, 2013. **12**(5): p. 347-357.

24. Rontogianni, S., et al., *Proteomic profiling of extracellular vesicles allows for human breast cancer subtyping.* Communications biology, 2019. **2**(1): p. 1-13.

25. Ricci, F., G. Adornetto, and G. Palleschi, *A review of experimental aspects of electrochemical immunosensors.* Electrochimica Acta, 2012. **84**: p. 74-83.

26. Wan, Y., et al., *Development of electrochemical immunosensors towards point of care diagnostics.* Biosensors and Bioelectronics, 2013. **47**: p. 1-11.

27. Bahadır, E.B. and M.K. Sezgintürk, *Applications of electrochemical immunosensors for early clinical diagnostics.* Talanta, 2015. **132**: p. 162-174.

28. Ghindilis, A.L., et al., *Immunosensors: electrochemical sensing and other engineering approaches.* Biosensors and Bioelectronics, 1998. **13**(1): p. 113-131.

29. Skládal, P., *Advances in electrochemical immunosensors.* Electroanalysis, 1997. **9**(10): p. 737-745.

30. Wu, J., et al., *Biomedical and clinical applications of immunoassays and immunosensors for tumor markers.* TrAC Trends in Analytical Chemistry, 2007. **26**(7): p. 679-688.

31. Wen, W., et al., *Recent advances in electrochemical immunosensors.* Analytical chemistry, 2016. **89**(1): p. 138-156.

32. Abuknesha, R.A., et al., *Efficient labelling of antibodies with horseradish peroxidase using cyanuric chloride.* Journal of immunological methods, 2005. **306**(1-2): p. 211-217.

33. Kulys, J. and R. Baronas, *Modelling of amperometric biosensors in the case of substrate inhibition.* Sensors, 2006. **6**(11): p. 1513-1522.

34. Nicell, J.A. and H. Wright, *A model of peroxidase activity with inhibition by hydrogen peroxide.* Enzyme and Microbial Technology, 1997. **21**(4): p. 302-310.

35. Ruzgas, T., et al., *Kinetic models of horseradish peroxidase action on a graphite electrode.* Journal of Electroanalytical Chemistry, 1995. **391**(1-2): p. 41-49.

36. Vojinović, V., et al., *Kinetics of soluble and immobilized horseradish peroxidase-mediated oxidation of phenolic compounds.* Biochemical engineering journal, 2007. **35**(2): p. 126-135.

37. Buchanan, I.D. and J.A. Nicell, *A simplified model of peroxidase-catalyzed phenol removal from aqueous solution.* Journal of Chemical Technology & Biotechnology: International Research in Process, Environmental & Clean Technology, 1999. **74**(7): p. 669-674.

38. Raghav, R. and S. Srivastava, *Immobilization strategy for enhancing sensitivity of immunosensors: L-Asparagine–AuNPs as a promising alternative of EDC–NHS activated citrate–AuNPs for antibody immobilization.* Biosensors and Bioelectronics, 2016. **78**: p. 396-403.

39. Duan, C. and M.E. Meyerhoff, *Immobilization of proteins on gold coated porous membranes via an activated self-assembled monolayer of thioctic acid.* Microchimica Acta, 1995. **117**(3-4): p. 195-206.

40. Pei, Z., et al., *Optimizing immobilization on two-dimensional carboxyl surface: pH dependence of antibody orientation and antigen binding capacity.* Analytical biochemistry, 2010. **398**(2): p. 161-168.

41. Scientific, T. *Carbodiimide Crosslinker Chemistry*. Available from: https://www.thermofisher.com/us/en/home/life-science/protein-biology/protein-biology-learning-center/protein-biology-resource-library/pierce-protein-methods/carbodiimide-crosslinker-chemistry.html.

42. Lomillo, M.A., J. Kauffmann, and M.A. Martinez, *HRP-based biosensor for monitoring rifampicin.* Biosensors and Bioelectronics, 2003. **18**(9): p. 1165-1171.

43. Hanrahan, G. and K. Lu, *Application of factorial and response surface methodology in modern experimental design and optimization.* Critical Reviews in Analytical Chemistry, 2006. **36**(3-4): p. 141-151.

44. Choi, Y.-J., H.J. Chae, and E.Y. Kim, *Steady-state oxidation model by horseradish peroxidase for the estimation of the non-inactivation zone in the enzymatic removal of pentachlorophenol.* Journal of bioscience and bioengineering, 1999. **88**(4): p. 368-373.

45. Wu, Y., et al., *Kinetic model for removal of phenol by horseradish peroxidase with PEG.* Journal of Environmental Engineering, 1999. **125**(5): p. 451-458.

46. Mansouri Majoumerd, M. and H.R. Kariminia, *Bisubstrate kinetic model for enzymatic decolorization of reactive black 5 by Coprinus cinereus Peroxidase.* Iranian Journal of Chemistry and Chemical Engineering (IJCCE), 2013. **32**(2): p. 125-134.

47. SATOH, T., *Global epidemiology of organophosphate and carbamate poisonings*, in *Toxicology of Organophosphate & Carbamate Compounds*2006, Elsevier. p. 89-100.

48. Soltaninejad, K. and S. Shadnia, *History of the use and epidemiology of organophosphorus poisoning*, in *Basic and Clinical Toxicology of Organophosphorus Compounds*2014, Springer. p. 25-43.

49. Sultatos, L.G., *Mammalian toxicology of organophosphorus pesticides.* Journal of Toxicology and Environmental Health, Part A Current Issues, 1994. **43**(3): p. 271-289.

50. Davis, C.S. and R.J. Richardson, *Organophosphorus compounds.* Experimental and clinical neurotoxicology, 1980: p. 527-544.

51. Jokanović, M., et al., *Pyridinium oximes in the treatment of poisoning with organophosphorus compounds*, in *Handbook of Toxicology of Chemical Warfare Agents*2020, Elsevier. p. 1145-1159.

52. Singh, B.K. and A. Walker, *Microbial degradation of organophosphorus compounds.* FEMS microbiology reviews, 2006. **30**(3): p. 428-471.

53. Barceló, D., et al., *Determination of organophosphorus compounds in Mediterranean coastal waters and biota samples using gas chromatography with nitrogen-phosphorus and chemical ionization mass spectrometric detection.* International journal of environmental analytical chemistry, 1990. **38**(2): p. 199-209.

54. Hauser, B., M. Schellin, and P. Popp, *Membrane-assisted solvent extraction of triazines, organochlorine, and organophosphorus compounds in complex samples combined with large-volume injection-gas chromatography/mass spectrometric detection.* Analytical chemistry, 2004. **76**(20): p. 6029-6038.

55. Jaffrezic-Renault, N., *New trends in biosensors for organophosphorus pesticides.* Sensors, 2001. **1**(2): p. 60-74.

56. Dhull, V., et al., *Acetylcholinesterase biosensors for electrochemical detection of organophosphorus compounds: a review.* Biochemistry research international, 2013. **2013**.

57. Boublik, Y., et al., *Acetylcholinesterase engineering for detection of insecticide residues.* Protein Engineering, 2002. **15**(1): p. 43-50.

58. Turdean, G.L., et al., *Sensitive detection of organophosphorus pesticides using a needle type amperometric acetylcholinesterase-based bioelectrode. Thiocholine electrochemistry and immobilised enzyme inhibition.* Journal of enzyme inhibition and medicinal chemistry, 2002. **17**(2): p. 107-115.

59. Palchetti, I., et al., *Determination of anticholinesterase pesticides in real samples using a disposable biosensor.* Analytica Chimica Acta, 1997. **337**(3): p. 315-321.

60. Skládal, P., et al., *Detection of carbamate pesticides in vegetable samples using cholinesterase-based biosensors.* Electroanalysis, 1997. **9**(14): p. 1083-1087.

61. Kohli, N., et al., *Nanostructured biosensor for measuring neuropathy target esterase activity.* Analytical chemistry, 2007. **79**(14): p. 5196-5203.

62. Pizarro-Cerda, J. and P. Cossart, *Listeria monocytogenes: cell biology of invasion and intracellular growth.* Microbiology spectrum, 2018. **6**(6).

63. Farber, J. and P. Peterkin, *Listeria monocytogenes, a food-borne pathogen.* Microbiology and Molecular Biology Reviews, 1991. **55**(3): p. 476-511.

64. Swaminathan, B. and P. Gerner-Smidt, *The epidemiology of human listeriosis.* Microbes and infection, 2007. **9**(10): p. 1236-1243.

65. Priyanka, B., R.K. Patil, and S. Dwarakanath, *A review on detection methods used for foodborne pathogens.* The Indian journal of medical research, 2016. **144**(3): p. 327.

66. Coelho, C., et al., *Listeria monocytogenes virulence factors, including listeriolysin O, are secreted in biologically active extracellular vesicles.* Journal of Biological Chemistry, 2019. **294**(4): p. 1202-1217.

67. Lee, J.H., et al., *Transcription factor σB plays an important role in the production of extracellular membrane-derived vesicles in Listeria monocytogenes.* PloS one, 2013. **8**(8): p. e73196.

68. Vdovikova, S., et al., *A novel role of Listeria monocytogenes membrane vesicles in inhibition of autophagy and cell death.* Frontiers in cellular and infection microbiology, 2017. **7**: p. 154.

69. Light, S.H., et al., *A flavin-based extracellular electron transfer mechanism in diverse Gram-positive bacteria.* Nature, 2018.

70. Li, R., et al., *Soluble Electron Shuttles Can Mediate Energy Taxis toward Insoluble Electron Acceptors.* Environmental Science & Technology, 2012. **46**(5): p. 2813-2820.

71. Kellogg, M.D., *Measurement of Biological Materials*, in *Clinical and Translational Science*2017, Elsevier. p. 137-155.

72. Matabaro, E., et al., *Current immunoassay methods for the rapid detection of aflatoxin in milk and dairy products.* Comprehensive reviews in food science and food safety, 2017. **16**(5): p. 808-820.

73. Gan, S.D. and K.R. Patel, *Enzyme immunoassay and enzyme-linked immunosorbent assay.* J Invest Dermatol, 2013. **133**(9): p. e12.

74. Darwish, I.A., *Immunoassay methods and their applications in pharmaceutical analysis: basic methodology and recent advances.* International journal of biomedical science: IJBS, 2006. **2**(3): p. 217.

75. medgadget. Available from: https://www.medgadget.com/2019/11/enzyme-linked-immunosorbent-assay-elisa-market-2017-predicted-to-reach-2-3-billion-by-industry-size-till-2025-at-a-cagr-of-5-1-size-trends-revenue-analysis-by-products-techniques-therapeut.html.

76. MARKET STUDY REPORT.

77. Beyzavi, K., et al., *Comparison of horseradish peroxidase and alkaline phosphatase-labelled antibodies in enzyme immunoassays.* Annals of clinical biochemistry, 1987. **24**(2): p. 145-152.

78. Veitch, N.C., *Horseradish peroxidase: a modern view of a classic enzyme.* Phytochemistry, 2004. **65**(3): p. 249-259.

79. Raposo, G. and W. Stoorvogel, *Extracellular vesicles: exosomes, microvesicles, and friends.* Journal of Cell Biology, 2013. **200**(4): p. 373-383.

80. Van Doormaal, F., et al., *Cell-derived microvesicles and cancer.* Neth J Med, 2009. **67**(7): p. 266-73.

81. Buzas, E.I., et al., *Emerging role of extracellular vesicles in inflammatory diseases.* Nature Reviews Rheumatology, 2014. **10**(6): p. 356-364.

82. D'Souza-Schorey, C. and J.W. Clancy, *Tumor-derived microvesicles: shedding light on novel microenvironment modulators and prospective cancer biomarkers.* Genes & development, 2012. **26**(12): p. 1287-1299.

83. Xie, H., et al., *Extracellular vesicles based electrochemical biosensors for detection of cancer cells: A review.* Chinese Chemical Letters, 2020.

84. Kumar, D., et al., *Biomolecular characterization of exosomes released from cancer stem cells: possible implications for biomarker and treatment of cancer.* Oncotarget, 2015. **6**(5): p. 3280.

85. Rubinstein, E., et al., *CD9, CD63, CD81, and CD82 are components of a surface tetraspan network connected to HLA-DR and VLA integrins.* European journal of immunology, 1996. **26**(11): p. 2657-2665.

86. Rybak, K. and S. Robatzek, *Functions of extracellular vesicles in immunity and virulence.* Plant physiology, 2019. **179**(4): p. 1236-1247.

87. Parsons, M.E., et al., *A protocol for improved precision and increased confidence in nanoparticle tracking analysis concentration measurements between 50 and 120 nm in biological fluids.* Frontiers in cardiovascular medicine, 2017. **4**: p. 68.

88. Muhammad, N., et al., *Engineering of the E. coli outer membrane protein FhuA to overcome the hydrophobic mismatch in thick polymeric membranes.* Journal of nanobiotechnology, 2011. **9**(1): p. 1-9.

89. Nolan, L.C. and K.E. O'Connor, *A spectrophotometric method for the quantification of an enzyme activity producing 4-substituted phenols: Determination of toluene-4-monooxygenase activity.* Analytical biochemistry, 2005. **344**(2): p. 224-231.

90. Wang, J., *Electrochemical glucose biosensors.* Chemical Reviews, 2008. **108**(2): p. 814-825.

91. Heinemann, L. and D.C. Klonoff, *Blood glucose meter market: this world is undergoing drastic changes.* Journal of diabetes science and technology, 2013. **7**(3): p. 584-6.

92. Kang, M.-H., et al., *Evaluation of four portable blood glucose meters in diabetic and non-diabetic dogs and cats.* Veterinary Quarterly, 2016. **36**(1): p. 2-9.

93. Chen, A.L. and S.M. Yang, *Replacing antibodies with aptamers in lateral flow immunoassay.* Biosensors & Bioelectronics, 2015. **71**: p. 230-242.

94. Jiang, N., et al., *Lateral and Vertical Flow Assays for Point-of-Care Diagnostics.* Advanced Healthcare Materials, 2019. **8**(14).

95. Lisi, F., J.R. Peterson, and J.J. Gooding, *The application of personal glucose meters as universal point-of-care diagnostic tools.* Biosensors & Bioelectronics, 2020. **148**.

96. Bahri, M., et al., *Capacitance electrochemical biosensor based on silicon nitride transducer for TNF-α cytokine detection in artificial human saliva: Heart failure (HF).* Talanta, 2019: p. 120501.

97. Tallapragada, S.D., et al., *Development of screen-printed electrode based immunosensor for the detection of HER2 antigen in human serum samples.* Bioelectrochemistry, 2017. **118**: p. 25-30.

98. Dempsey, E. and D. Rathod, *Disposable printed lateral flow electrochemical immunosensors for human cardiac troponin T.* IEEE Sensors Journal, 2018. **18**(5): p. 1828-1834.

99. Katz, L.B., et al., *Meeting the New FDA Standard for Accuracy of Self-Monitoring Blood Glucose Test Systems Intended for Home Use by Lay Users.* Journal of diabetes science and technology, 2020: p. 1932296820906184-1932296820906184.

100. Belluzo, M.S., M.É. Ribone, and C.M. Lagier, *Assembling amperometric biosensors for clinical diagnostics.* Sensors, 2008. **8**(3): p. 1366-1399.

101. Branch, G. and M. Joslyn, *The kinetics of the auto-oxidation of catechol in the presence of several foreign substances.* Journal of the American Chemical Society, 1935. **57**(12): p. 2388-2394.

102. Baronas, D., F. Ivanauskas, and R. Baronas, *Mechanisms controlling the sensitivity of amperometric biosensors in flow injection analysis systems.* Journal of mathematical chemistry, 2011. **49**(8): p. 1521-1534.

103. Loghambal, S. and L. Rajendran, *Mathematical modeling in amperometric oxidase enzyme–membrane electrodes.* Journal of Membrane Science, 2011. **373**(1-2): p. 20-28.

104. Huang, J., W. Huang, and T. Wang, *Catalytic and Inhibitory Kinetic Behavior of Horseradish Peroxidase on the Electrode Surface.* Sensors, 2012. **12**(11): p. 14556-14569.

105. Ivanec-Goranina, R. and J. Kulys, *Kinetic study of peroxidase-catalyzed oxidation of 1-hydroxypyrene. Development of a nanomolar hydrogen peroxide detection system.* Central European Journal of Biology, 2008. **3**(3): p. 224.

106. Galende, P.P., et al., *Kinetics of Spanish broom peroxidase obeys a Ping-Pong Bi–Bi mechanism with competitive inhibition by substrates.* International journal of biological macromolecules, 2015. **81**: p. 1005-1011.

107. Deyhimi, F. and F. Nami, *Peroxidase-catalyzed electrochemical assay of hydrogen peroxide: A ping–pong mechanism.* International Journal of Chemical Kinetics, 2012. **44**(10): p. 699-704.

108. Šimelevicius, D. and K. Petrauskas, *Application of the Butler-Volmer Equation in Mathematical Modelling of Amperometric Biosensor.*

109. Compton, R.G. and C.E. Banks, *Understanding voltammetry*2011: World Scientific.

110. Richardson, R.J., et al., *Neuropathy target esterase as a biomarker and biosensor of delayed neuropathic agents*, in *Handbook of Toxicology of Chemical Warfare Agents*2015, Elsevier. p. 935-952.

111. Compton, R.G. and J. Wadhawan, *Electrochemistry: Nanoelectrochemistry*. Vol. 12. 2013: Royal Society of Chemistry.

112. Coche-Guerente, L., et al., *Amplification of amperometric biosensor responses by electrochemical substrate recycling: Part I. Theoretical treatment of the catechol–polyphenol oxidase system.* Journal of Electroanalytical Chemistry, 1999. **470**(1): p. 53-60.

113. Coche-Guerente, L., et al., *Amplification of amperometric biosensor responses by electrochemical substrate recycling: Part II. Experimental study of the catechol–polyphenol oxidase system immobilized in a laponite clay matrix.* Journal of Electroanalytical Chemistry, 1999. **470**(1): p. 61-69.

114. Coche-Guerente, L., P. Labbe, and V. Mengeaud, *Amplification of Amperometric Biosensor Responses by Electrochemical Substrate Recycling. 3. Theoretical and Experimental Study of the Phenol− Polyphenol Oxidase System Immobilized in Laponite Hydrogels and Layer-by-Layer Self-Assembled Structures.* Analytical chemistry, 2001. **73**(14): p. 3206-3218.

115. Kohli, N., et al., *Theoretical and experimental study of bi-enzyme electrodes with substrate recycling.* Journal of electroanalytical chemistry, 2010. **641**(1-2): p. 104-110.

116. Indira, K. and L. Rajendran, *Analytical Expressions Pertaining to the Concentration of Substrates and Product in Phenol-Polyphenol Oxidase System Immobilized in Laponite Hydrogels: A Reciprocal Competitive Inhibition Process.* Advances in Physical Chemistry, 2012. **2012**.

117. Achi, F., et al., *Mathematical model and numerical simulation of inhibition based biosensor for the detection of Hg (II).* Sensors and Actuators B: Chemical, 2015. **207**: p. 413-423.

118. Meena, A. and L. Rajendran, *Mathematical modeling of amperometric and potentiometric biosensors and system of non-linear equations–Homotopy perturbation approach.* Journal of Electroanalytical Chemistry, 2010. **644**(1): p. 50-59.

119. Ašeris, V., et al., *Modelling glucose dehydrogenase-based amperometric biosensor utilizing synergistic substrates conversion.* Electrochimica Acta, 2014. **146**: p. 752-758.

120. BRENDA. *The Comprehensive Enzyme Information System*. Available from: https://www.brenda-enzymes.org/.

121. Amatore, C., et al., *The real meaning of Nernst's steady diffusion layer concept under non-forced hydrodynamic conditions. A simple model based on Levich's seminal view of convection.* Journal of Electroanalytical Chemistry, 2001. **500**(1-2): p. 62-70.

122. Fransaer, J. and M. Ammam, *Mathematical modeling of the amperometric response to glucose of glucose oxidase films deposited by AC-electrophoresis.* Journal of Sensor Technology, 2011. **1**(02): p. 17.

123. Grunwald, P., *Determination of effective diffusion coefficients—an important parameters for the efficiency of immobilized biocatalysts.* Biochemical education, 1989. **17**(2): p. 99-102.

124. Ximenes, V.F., et al., *The effect of pH on horseradish peroxidase-catalyzed oxidation of melatonin: production of N1-acetyl-N2-formyl-5-methoxykynuramine versus radical-mediated degradation.* Journal of pineal research, 2007. **42**(3): p. 291-296.

125. Kohli, N., et al., *Nanostructured biosensor for measuring neuropathy target esterase activity.* Analytical Chemistry, 2007. **79**(14): p. 5196-5203.

126. Parthasarathy, P. and S. Vivekanandan, *A numerical modelling of an amperometric-enzymatic based uric acid biosensor for GOUT arthritis diseases.* Informatics in Medicine Unlocked, 2018. **12**: p. 143-147.

127. Ismail, I., G. Oluleye, and I. Oluwafemi, *Mathematical modelling of an enzyme-based biosensor.* Int J Biosen Bioelectron, 2017. **3**(2): p. 265-268.

128. Baronas, R., et al., *Effect of diffusion limitations on multianalyte determination from biased biosensor response.* Sensors, 2014. **14**(3): p. 4634-4656.

129. Kacser, H., J.A. Burns, and D.A. Fell, *The control of flux*, 1995, Portland Press Limited.

130. Gerard, M., A. Chaubey, and B. Malhotra, *Application of conducting polymers to biosensors.* Biosensors and bioelectronics, 2002. **17**(5): p. 345-359.

131. Worsfold, P., et al., *Encyclopedia of analytical science*2019: Elsevier.

132. Honeychurch, K.C. and M. Piano, *Electrochemical (bio) sensors for environmental and food analyses*, 2018, Multidisciplinary Digital Publishing Institute.

133. Bachan Upadhyay, L.S. and N. Verma, *Enzyme inhibition based biosensors: A review.* Analytical Letters, 2013. **46**(2): p. 225-241.

134. Gahlaut, A., *Electrochemical biosensors for determination of organophosphorus compounds.* Open Journal of Applied Biosensor, 2012. **1**(01): p. 1.

135. Pundir, C. and A. Malik, *Bio-sensing of organophosphorus pesticides: A review.* Biosensors and Bioelectronics, 2019. **140**: p. 111348.

136. Zheng, Y., et al., *A review on the detoxification of organophosphorus compounds by microorganisms.* African Journal of Microbiology Research, 2013. **7**(20): p. 2127-2134.

137. Pundir, C.S. and N. Chauhan, *Acetylcholinesterase inhibition-based biosensors for pesticide determination: A review.* Analytical Biochemistry, 2012. **429**(1): p. 19-31.

138. Xu, M.-L., et al., *Detection of pesticide residues in food using surface-enhanced Raman spectroscopy: a review.* Journal of agricultural and food chemistry, 2017. **65**(32): p. 6719-6726.

139. Palchetti, I., S. Laschi, and M. Mascini, *Electrochemical biosensor technology: application to pesticide detection*, in *Biosensors and Biodetection*2009, Springer. p. 115-126.

140. Kumaran, S. and M. Morita, *Application of a cholinesterase biosensor to screen for organophosphorus pesticides extracted from soil.* Talanta, 1995. **42**(4): p. 649-655.

141. Trojanowicz, M. and M.L. Hitchman, *Determination of pesticides using electrochemical biosensors.* TrAC Trends in Analytical Chemistry, 1996. **15**(1): p. 38-45.

142. Zhang, S., H. Zhao, and R. John, *Development of a quantitative relationship between inhibition percentage and both incubation time and inhibitor concentration for inhibition biosensors—theoretical and practical considerations.* Biosensors and Bioelectronics, 2001. **16**(9-12): p. 1119-1126.

143. Choi, J.-W., J. Min, and W.-H. Lee, *Signal analysis of fiber-optic biosensor for the detection of organophosphorus compounds in the contaminated water.* Korean Journal of Chemical Engineering, 1997. **14**(2): p. 101-108.

144. Richardson, R.J., et al., *Neuropathy target esterase as a biomarker and biosensor of delayed neuropathic agents*, in *Handbook of Toxicology of Chemical Warfare Agents*2020, Elsevier. p. 1005-1025.

145. Pohanka, M., *Acetylcholinesterase inhibitors: a patent review (2008–present).* Expert opinion on therapeutic patents, 2012. **22**(8): p. 871-886.

146. Irie, T., K. Fukushi, and M. Iyo, *Evaluation of phenylmethanesulfonyl fluoride (PMSF) as a tracer candidate mapping acetylcholinesterase in vivo.* Nuclear medicine and biology, 1993. **20**(8): p. 991-992.

147. Kraut, D., et al., *Inactivation studies of acetylcholinesterase with phenylmethylsulfonyl fluoride.* Molecular Pharmacology, 2000. **57**(6): p. 1243-1248.

148. Coche-Guerente, L., P. Labbé, and V. Mengeaud, *Amplification of Amperometric Biosensor Responses by Electrochemical Substrate Recycling. 3. Theoretical and Experimental Study of the Phenol− Polyphenol Oxidase System Immobilized in Laponite Hydrogels and Layer-by-Layer Self-Assembled Structures.* Analytical chemistry, 2001. **73**(14): p. 3206-3218.

149. Ramaswamy, V., et al., *Listeria-review of epidemiology and pathogenesis.* Journal of Microbiology Immunology and Infection, 2007. **40**(1): p. 4.

150. Shi, L., et al., *Extracellular electron transfer mechanisms between microorganisms and minerals.* Nature Reviews Microbiology, 2016. **14**(10): p. 651-662.

151. Light, S.H., et al., *A flavin-based extracellular electron transfer mechanism in diverse Gram-positive bacteria.* Nature, 2018. **562**(7725): p. 140-144.

152. Li, R., et al., *Shewanella oneidensis MR-1 Chemotaxis in a Diffusion Gradient Chamber.* Environmental Science & Technology, 2011. **45**(3): p. 1014-1020.

153. Li, R., et al., *Soluble electron shuttles can mediate energy taxis toward insoluble electron acceptors.* Environmental science & technology, 2012. **46**(5): p. 2813-2820.

154. Kotloski, N.J. and J.A. Gralnick, *Flavin electron shuttles dominate extracellular electron transfer by Shewanella oneidensis.* MBio, 2013. **4**(1).

155. Oram, J. and L.J. Jeuken, *Tactic response of Shewanella oneidensis MR-1 toward insoluble electron acceptors.* MBio, 2019. **10**(1).

156. Premaratne, R.J., W.-J. Lin, and E.A. Johnson, *Development of an improved chemically defined minimal medium for Listeria monocytogenes.* Applied and Environmental Microbiology, 1991. **57**(10): p. 3046-3048.

157. Hardy, J., et al., *Extracellular replication of Listeria monocytogenes in the murine gall bladder.* Science, 2004. **303**(5659): p. 851-853.